THE IMPACTS OF LAND COVER CHANGE ON CLIMATE OVER CHINA

A Dissertation

by

LIANG CHEN

Submitted to the Office of Graduate and Professional Studies of
Texas A&M University
in partial fulfillment of the requirements for the degree of

DOCTOR OF PHILOSOPHY

Chair of Committee,	Oliver W. Frauenfeld
Committee Members,	Steven M. Quiring
	David M. Cairns
	Gerald R. North
Head of Department,	David M. Cairns

August 2015

Major Subject: Geography

ABSTRACT

China has experienced substantial land cover changes for hundreds of years, such as deforestation, agricultural expansion, and urbanization. These land cover changes can modify the physical and thermodynamic characteristics of the land surface, thereby influencing climate at regional or broader scales. In this dissertation, I first examine the performance of state-of-the-art general circulation models to assess their ability to skillfully simulate climate in China. Then, the CESM and WRF models are used to investigate specific biogeophysical effects of land cover changes—including vegetation changes and urbanization.

Multimodel ensembles of CMIP5 models are found to well capture the spatial patterns of seasonal and annual temperature and precipitation. However, they contain substantial cold biases over the Tibetan Plateau especially in the cold season, and overestimate precipitation in most regions of China, especially along the eastern edge of the Tibetan Plateau. Four CMIP5 models are identified due to their better simulation of historical surface air temperature variability over China: MPI-ESM-LR, CanESM2, MIROC-ESM, and CCSM4. Focusing on CCSM4, a subset of CESM, sensitivity analyses indicate that, for historical vegetation changes, summer temperatures are regulated by evapotranspiration, which can decrease the diurnal temperature range. Decreases in winter temperature over northern China are mainly influenced by surface albedo changes. Vegetation changes do not exhibit significant impacts on summer precipitation or the East Asian summer monsoon, but could strengthen East Asian winter monsoon and decrease

winter precipitation in southern China. When urbanization is included, there are more significant and extensive impacts on temperature and precipitation in China, including greatly increased minimum temperatures and influences on East Asian Monsoon. Future climate projection reveals that urbanization produces strong warming effects, up to 1.9°C at local scales, which is comparable to the magnitude of greenhouse gas forcing under the RCP 4.5 scenario. The impacts of urbanization on precipitation show a combined effect from local moisture deficits and large-scale circulation changes.

In summation, land cover changes play an important role in climate over China. Not only vegetation changes, but urbanization also should be included in model simulations to provide realistic and complete climatic impacts of land cover changes.

ACKNOWLEDGEMENTS

First of all, I would like to thank my advisor, Dr. Oliver Frauenfeld, for all his support and guidance throughout these four years. He inspired me with great ideas and directions, but gave me freedom and independence in my research. His steady guiding hand, wisdom, patience, and high standards have been invaluable to me and my development as a scientist and a teacher. My gratitude also goes to my committee members, Dr. Steven Quiring, Dr. David Cairns, and Dr. Gerald North for their insightful suggestions and constructive criticism on my research.

I am grateful to my colleagues in the Climate Science Lab for their help, support, and the great time they brought me. I am so proud to have been a part of this inspiring team of climatologists and have greatly benefited from the weekly meeting with them. I also want to extend my gratitude to the Department of Geography for financial support and considerable teaching experience. I would especially like to thank the organizations and individuals who provided data for my study, and TAMU Supercomputing Facility for providing computing resources of my model simulations.

Last but not least, I would like to thank my parents and friends who have always supported my endeavors and given me the most essential elements for success − happiness and love.

NOMENCLATURE

CAM	Community Atmosphere Model
CanESM2	Canadian Earth System Model
CCSM	Community Climate System Model
CESM	Community Earth System Model
CLM	Community Land Model
CRU	Climatic Research Unit
CUR	A Control Run Forced with Current Land Cover Conditions in CESM
CMIP3	Coupled Model Intercomparison Project Phase 3
CMIP5	Coupled Model Intercomparison Project Phase 5
DJF	December-January-February
EAM	East Asian Monsoon
EASM	East Asian Summer Monsoon
EAWM	East Asian Winter Monsoon
ECMWF	European Centre for Medium-Range Weather Forecasts
ERA-Interim	ECMWF Reanalysis - Interim
ENSO	El Niño-Southern Oscillation
GCM	General Circulation Model
GHCN	Global Historical Climatology Network
GISS	NASA Goddard Institute for Space Studies
GPCC	Global Precipitation Climatology Centre

HIST	A Historical Run (1995−2005) in WRF
IPCC	Intergovernmental Panel on Climate Change
IPCC AR4	Intergovernmental Panel on Climate Change Fourth Assessment Report
IPCC AR5	Intergovernmental Panel on Climate Change Fifth Assessment Report
JJA	June-July-August
LAI	Leaf Area Index
MAE	Mean Absolute Error
ME	Mean Error
MIROC-ESM	The Model for Interdisciplinary Research on Climate − Earth System Model
MPI-ESM-LR	The coupled Max Planck Institute Earth System Model at base resolution
NAO	North Atlantic Oscillation
NAT	A Completely Natural Land Cover Run in CESM
NCAR	National Center for Atmospheric Research
NCEP	National Centers for Environmental Prediction
PFT	Plant Functional Type
POT+URB	A Potential Vegetation Run with Current Urbanization in CESM
RCP	Representative Concentration Pathways
RCP45	A RCP4.5 Scenario Run (2050−2060) in WRF
RegCM	The Regional Climate Model system
RMSE	Root Mean Square Error
RUC	Rapid Update Cycle Land Surface Scheme

SDE	Standard Deviation of the Error
SDR	Ratio of Spatial Standard Deviation in the Models against that of the Observations
SST	Sea Surface Temperature
TRMM	Tropical Rainfall Measuring Mission
WANG	Observational Time Series of Annual Mean Surface Air Temperature over China Developed by Wang
WCRP	World Climate Research Programme
WRF	Weather Research and Forecasting Model
UCM	Urban Canopy Model
UDEL	Climate Observation Dataset from University of Delaware
URB	A RCP4.5 Scenario Run (2050−2060) Forced with Future Urbanized Land Cover Condition in WRF

TABLE OF CONTENTS

Page

LIST OF FIGURES

Page

LIST OF TABLES

Page

1. INTRODUCTION AND LITERATURE REVIEW

1.1. Introduction

Land cover changes can influence regional climate through modifying the surface energy and water fluxes, and can also affect climate at large scales through adjustments in atmospheric general circulation (IPCC 2007). With its rapid population growth and economic development, China has experienced significant land cover changes, such as urbanization (Hua et al. 2008; Zhou et al. 2004), agricultural expansion (Zhang 2000), and desertification (Wang et al. 2006a; Xue 1996). Even though there have been several studies focusing on land surface-atmosphere interactions through observations (Hua et al. 2008; Li et al. 2013a; Yang et al. 2009b; Zhang et al. 2005) and numerical modeling (Fu 2003; Gao et al. 2003; Zheng et al. 2002), there is still limited scientific understanding of the impacts of land cover changes on climate in China (Hua and Chen 2013). Model-based studies on land-atmosphere interactions rely on the performance of the climate models used. The development of the Coupled Model Intercomparison Project Phase 5 (CMIP5) promoted improvement of climate models to support the Intergovernmental Panel on Climate Change's (IPCC) Fifth Assessment Report (AR5) (Flato et al. 2013). However, there has been little work applying these new climate models to investigate the climate variability and possible effects of land cover changes on climate over China. Also, most previous studies only considered vegetation changes (Fu 2003; Gao et al. 2003; Zhao and Pitman 2005; Zheng et al. 2002) or urbanizations (Feng et al. 2013; Feng et al. 2012; Feng et al. 2014; Wang et al. 2012; Wang et al. 2013) individually, however, both land surface

alterations have occurred simultaneously and contributed to land cover and land use changes. Their joint impacts on historical climate have rarely been compared. Furthermore, most previous studies only focused on the impacts of the historical land cover changes on climate. Few studies have considered the impacts of land cover changes within future climate projections, although land cover changes may have a comparable effect on climate to that of increases in greenhouse gases (Chase et al. 2001; Feddema et al. 2005b; Zhao and Pitman 2005). In this study, I therefore provide a comprehensive investigation into the performance of current GCMs in their ability to simulate climate over China, how land cover changes in China have influenced climate in the past, and what their impacts will be in the future. The specific objectives to address these overarching goals are to 1) evaluate the performance of the state-of-the-art GCMs in China, 2) investigate the climatic impacts of historical land cover changes, including both vegetation changes and urbanization over China, and 3) estimate the impacts of land cover changes on future climate. This will provide a better understanding of the land surface-atmosphere interactions over China, and provide a scientific assessment with important implications for agriculture, ecology, and water management, all of which are crucial to China's future.

1.2. Literature Review

Assessing the climate impacts of land cover change is a vital part of understanding climate change. Land cover changes can influence the local, regional, and global climate system through a series of biogeophysical and biogeochemical processes that modify the exchanges of momentum, energy, and mass between the land surface and the overlying

atmosphere (Bonan 2008). Previous studies have shown that historical land cover change has affected the climate system at local, regional, and global scales. There are two biogeophysical effects on temperature derived from changes in land cover properties: the surface albedo effect that modifies the received solar irradiance, and the evapotranspiration effect that changes the latent heat flux (Fall et al. 2010; Gibbard et al. 2005). Several studies suggested that mid-latitude land cover changes from forests to croplands can increase the surface albedo and lead to cooling (Betts et al. 2007; Feddema et al. 2005a). The IPCC 5th assessment report (AR5) indicated a radiative cooling of -0.15 W/m^2 from surface albedo changes due to human-induced land cover change since 1750 (IPCC 2013). On the other hand, studies of deforestation in tropical regions showed that deforestation can increase surface temperature through reduced evapotranspiration and increased sensible heat flux (Pongratz et al. 2006). Lawrence and Chase (2010) suggested that the current global warming has been predominantly driven by this evapotranspiration effect, with the albedo forcing playing a secondary role. Precipitation impacts of land cover change are not as straightforward as those of temperature, because they depend on many more complex factors, such as geographic location, regional atmospheric characteristics, area extent of land cover change, and teleconnections (Pielke et al. 2007). Swann et al. (2011) suggested that mid-latitude afforestation can lead to a decrease in precipitation over parts of the Amazon region and an increase over the Sahel and Sahara regions. Lawrence and Chase (2010) found a significant localized and seasonal change in precipitation response to land cover change, and specified that the largest

decrease is in annual precipitation for the China region, with the largest decrease in summer and the smallest in winter.

Since China has been experiencing dramatic changes in land cover, scientists have also recognized land cover impacts on climate at regional and broader scales. Generally, two methods have been used to investigate land-atmosphere interactions. The first is an observation minus reanalysis (OMR) approach, which exploits the difference between directly observed in situ data, and temperature data from atmospheric reanalysis models. The reanalysis data used in this approach are insensitive to surface processes associated with different land cover types, whereas the in situ observations are strongly influenced by surface changes. Therefore the OMR approach allows for an observational quantification of surface processes (Kalnay and Cai 2003). By using the OMR method, Zhang et al. (2005) suggest that urbanization in southern China, deforestation, and desertification in northern China may increase surface temperature, while vegetation cover increases may decrease surface temperature over the Yellow River Basin. Yang et al. (2009b) also indicate that surface warming is larger in barren and anthropogenically developed areas. Smaller warming trends are found in areas with vegetation cover. However, this observationally-based method can only examine the relationship between temperature and land cover types. Effects of land cover changes on other climatic elements, as well as the physical mechanisms of the land-atmosphere interactions, cannot be easily explored.

Climate models coupled with land surface models are commonly used to investigate land-atmosphere interactions. Zhao and Pitman (2005) examined climate impacts of land

cover change over eastern China and increasing CO_2 with a GCM (NCAR CCM3) coupled with the Biosphere-Atmosphere Transfer Scheme (BATS). They suggest that land cover changes have a comparable effect on climate to that of historical increases in greenhouse gases at the regional scale. By using a global atmospheric GCM (CAM4.0) coupled with an urban canopy parameterization scheme, Chen and Zhang (2013) found warming effects of large-scale urbanization in eastern China and its influence on the East Asian winter monsoon. Also, regional models are used to investigate feedbacks of land cover to climate at the regional scale. Compared with GCMs, regional climate models allow for a more detailed investigation of the interactions between land cover modification and the atmospheric conditions, because regional models provide higher spatial resolution and capture physical processes and feedbacks occurring at the regional scale, which GCMs are not able to describe due to their coarse resolution (Anav et al. 2010; Fu 2003; Li et al. 2013b; Myoung et al. 2012; Shi and Wang 2003; Wang et al. 2012; Zheng et al. 2002). For instance, a regional climate model (RegCM2) coupled with BATS was used to estimate the climate effects of historical (Gao et al. 2003) and other possible land cover changes such as desertification, afforestation, and vegetation degradation (Zheng et al. 2002) in China. There is a resulting decrease in mean annual precipitation over northwest China and a decrease in temperature in coastal areas as a result of historical land cover changes. Vegetation degradation may increase flood events over the Yangtze-Huai River valleys and intensify droughts in northern China.

These model-based studies rely strongly on the skill of climate models at the particular study regions. For instance, land surface models are a key component in climate

models for simulating the energy, matter, and momentum exchanges between the land surface and atmosphere, thereby capturing the climatic responses to land cover changes. However, most of the land surface models used in previous studies are out-of-date already, because of large uncertainties in modeling soil moisture, soil temperature, and evapotranspiration (Abramowitz et al. 2008; Yang et al. 2009a). The IPCC AR5 promoted the development of the fifth phase of the Coupled Model Intercomparison Project (CMIP5), which is comprised of state-of-the-art GCMs. These climate models have been improved and many of them have been expanded into earth system models by adding more complex land surface processes that can be important contributors to land-atmosphere interactions. However, there has been little work evaluating the performance of these new models and applying them to investigate the effects of land cover changes on climate over China.

Vegetation changes, such as deforestation and agricultural expansion, and urbanization can be considered as the two most prominent cover changes due to human activities. As mentioned before, there are plenty of studies that have discussed the possible impacts of vegetation changes and urbanization on climate in China. However, most of these studies have only considered the two types of land cover changes individually, even though their impact has occurred simultaneously in the process of land cover changes. Furthermore, the impacts from vegetation changes and urbanization on historical climate have never been compared.

For future climate projections, Feddema et al. (2005b) suggest that land cover changes can significantly alter the regional climate outcomes associated with global

warming. In CMIP5, land cover changes have been assessed for both historical and future climate simulations (Dirmeyer et al. 2010; Kumar et al. 2013b). Based on the results from CMIP5, Brovkin et al. (2013) indicate that the effects of land cover changes are significant where the spatial extent of changes exceeds 10% of the land area, even though they do not have a discernible effect globally. However, of the land cover changes assessed in CMIP5, urbanization (urban area expansion) was not included in future climate modeling efforts (Di Vittorio et al. 2014; Oleson 2011). It has been suggested that a sustained assessment of climate forcing and feedbacks of land cover changes needs to account for realistic land surface complexity, including human disturbance such as from land cover changes and urbanization (Loveland and Mahmood 2014). Mahmood et al. (2014) also indicate that urban forcing should be included in future climate modeling systems because of its impacts on atmospheric dynamics, thermodynamics, energy exchanges, cloud microphysics, and composition.

Therefore, to provide a more accurate and systematic evaluation of the climate impacts of land cover change, this dissertation evaluates the performance of the state-of-the-art climate models for China, investigates the climate impacts of land cover changes by using the fully coupled NCAR Community Earth System Model (CESM), and further explores the impacts of urbanization on future climate by using the regional Weather Research and Forecasting (WRF) climate model. This dissertation is broken down into three specific questions:

1) How skillful is the performance of current GCMs over China?

Before applying any climate modeling approach to investigate land-atmosphere interactions over China, the performance of the models must be assessed. The IPCC AR5 promoted the development of the CMIP5, which makes it possible for scientists outside of the modeling community to conduct comprehensive analyses on climate variability and change at both global and regional scale. Therefore, the first step in this study is to evaluate how well these state-of-the-art GCMs perform in our study area.

2) What are the climate impacts of land cover change over China?

Based on the model evaluation in objective 1 and availability of model code, CESM is used to explore the biogeophysical impacts of land cover changes on climate over China. This part focuses specifically on how historical land cover changes including agricultural expansion and urbanization in China influence regional climate, and whether urbanization exerts a comparable impact on climate as vegetation changes do.

3) What are impacts of urbanization on future climate over China?

Urban warming has not explicitly been taken into account in future climate change simulations to date (IPCC 2007; Oleson 2011). This part therefore focuses on the impacts of future urbanization on climate in China. Due to the uncertainties in GCMs, the WRF model, which better delineates the urban extent and is driven by the RCP 4.5 future climate projections from CESM, is used to estimate the biogeophysical effects of urban expansion on future climate. This will clarify the contribution of urbanization to future temperature changes.

2. SURFACE AIR TEMPERATURE CHANGES OVER THE 20TH AND 21ST CENTURIES IN CHINA SIMULATED BY 20 CMIP5 MODELS*

2.1. Introduction

The global average surface temperature has increased by 0.74°C ± 0.18°C during 1906–2005 (IPCC 2007). This warming trend, in particular the warming since the mid-20th century, is very likely due to the increased level of anthropogenic greenhouse gas concentrations (Wang et al. 2011). China has also experienced significant temperature increases concurrent with global warming. In fact, previous studies suggest that the central-northern continent of eastern Asia was one of the most rapidly warming regions in the world during the last two decades of the 20th century (Wang and Gong 2000). For China as a whole, Ding et al. (2007) imply that the annual mean surface air temperature has increased by 0.5–0.8°C during the 20th century, with an accelerated warming of 1.1°C during the second half of the century, which is slightly higher than the global temperature trend for the same period. Based on 486 stations during the period 1960–2000, Qian and Qin (2006) suggest that temperature increased at a rate of 0.2–0.3°C $(10\ yr)^{-1}$ in northern China, and less than 0.1°C $(10\ yr)^{-1}$ in the southern China. Seasonally, the greatest warming occurred in winter, and a cooling took place in the Yangtze River and Yellow River basins in spring and summer.

* This section is reprinted with permission from "Surface Air Temperature Changes over the 20th and 21st Centuries in China Simulated by 20 CMIP5 Models" by Chen and Frauenfeld, 2014. *Journal of Climate*, 27, 3920–3937, Copyright [2014] by the American Meteorological Society.

Accurate prediction of future climate change, especially in regard to global warming, has been one of the most important scientific and societal challenges in current climate research efforts. Simulations from coupled ocean-atmosphere general circulation models (GCMs) forced with projected greenhouse gas and aerosol emissions are the primary tools for estimating trends and variability of future climate (Kharin et al. 2007). The establishment of the third phase of the Coupled Model Intercomparison Project (CMIP3) by the World Climate Research Programme (WCRP) provided scientists outside of the modeling community an opportunity to conduct comprehensive analyses on climate variability and change at both global and regional scales, based on the output from multiple climate models (Meehl et al. 2007). The Intergovernmental Panel on Climate Change (IPCC) Fourth Assessment Report (AR4) estimates a warming of about 0.2°C $(10\ yr)^{-1}$ for a range of emission scenarios over the next two decades. By the end of the 21st century, global mean surface temperature is projected to increase by 1.1–6.4°C over the 1990 level (Van Vuuren et al. 2008). Detailed temperature projections at a regional scale are also crucial for local development and decision-making at a country-level, such as in China. Under varied emission scenarios, the annual mean temperature in China based on CMIP3 simulations is projected to increase by 3.9–6.0°C by 2100 relative to the 1961–1990 average (Ding et al. 2007). However, limitations exist in CMIP3. Wild (2009) indicates that CMIP3 models underestimate the decadal variations in global land surface warming during the 20th century. Using 19 coupled climate models driven by historical natural and anthropogenic forcings in CMIP3, Zhou and Yu (2006) found that the robustness of temperature estimates averaged over China is lower than that of the global and

hemispheric average, and discrepancies exist between the observed and simulated spatial patterns of temperature trends. By comparing output from 24 models with observational data in China, Miao et al. (2012) evaluated the performance of the CMIP3 GCMs in simulating temperature, and found that 18 models underestimate the annual mean temperature of China. Based on 24 CMIP3 models, Li et al. (2011) indicated that in simulating both the daily maximum and minimum July–August temperatures, the largest cold bias is found over western China.

The IPCC Fifth Assessment Report (AR5) promoted the development of the fifth phase of CMIP (hereafter CMIP5), which is comprised of state-of-the-art GCMs. Compared with CMIP3, CMIP5 uses new Representative Concentration Pathways (RCPs) and includes a larger number of GCMs that are more complex and have higher spatial resolution (Taylor et al. 2011). By comparing results from CMIP3 and CMIP5, Knutti and Sedlacek (2013) suggest that the projected global temperature change from CMIP5 is remarkably similar to that from CMIP3 after accounting for the different underlying scenarios. Based on 19 CMIP5 models, Kumar et al. (2013a) found that the multimodel ensemble average of the global land-averages temperature trend (0.07°C $(10\ yr)^{-1}$) agrees well with the observed trend (0.08°C $(10\ yr)^{-1}$) during the 20th century, but large uncertainties exist in the simulation of regional-scale temperature trends in CMIP5. Therefore, it is important to evaluate the performance of the state-of-the-art climate models in CMIP5 for different regions. Based on 24 CMIP3 and 10 CMIP5 models, Hua et al. (2013) found that all models capture the climatological pattern of land surface temperatures for the period 1960−2000, but a large spread exists among the models in

simulation the climatology, interannual variation, and temperature trends. Over the Tibetan Plateau, it is found that cold biases exist in the majority of the CMIP5 models, with a mean underestimation of 1.1–2.5°C for the months of December–May, and less than 1°C for June–October (Su et al. 2012). Future temperature projections suggest that there will be 1.9–3.3°C and 3.4–5°C increases in 2070-2099 under RCP4.5 and RCP8.5, respectively (Wang and Chen 2013). However, to date there is a lack of a comprehensive evaluation of CMIP5 temperature simulations and their possible improvement compared with CMIP3 over the entire region of China. China's extremely complex terrain and confluence of circulation regimes (such as the various monsoons) likely represent a particularly challenging environment for GCMs.

Therefore, the goal of this investigation is to objectively and comprehensively evaluate the performance of CMIP5 surface air temperature simulations over China. As the world's largest emitter of carbon dioxide, China is thus also the largest contributor to greenhouse gas-based climate change. Due to the continuing rapid development and industrialization of China and the contribution of this growth to regional and global change, accurate projections for this part of the world are of particular concern. Over the coming years, until the release of the IPCC's sixth assessment report in approximately 2020, these CMIP5 simulations will likely be used by various subfields of the scientific community, ranging from physical to social sciences, as the basis for future climate projections. CMIP5 simulations for China in particular will see increased usage, as the rapidly emerging science and technology community in China will also increasingly rely on these state-of-the-science projections for their region of the world. It is thus important to assess the

accuracy and skill of CMIP5 simulations for China, as well as the degree to which they have improved or otherwise changed with respect to CMIP3. Such evaluations are then also useful for identifying shortcomings and necessary improvements for future modeling efforts.

Our evaluation includes an assessment of the CMIP5 multimodel ensemble average, which is commonly used by researchers because the multimodel-average approach reduces noise in the predictions. This spatial and temporal (annual and seasonal scale) evaluation is conducted with respect to observational data, as well as with CMIP3 to identify potential CMIP5 improvements. The quality of the CMIP5 multimodel average obviously depends on the quality of the individual models. Therefore, we also evaluate and identify the most (and least) suitable individual CMIP5 models for this part of the world, to minimize the uncertainty in multimodel ensemble averages, and to improve future temperature projections. Finally, we provide a comprehensive overview of CMIP5 temperature projections for China over the 21st century. This paper is organized as follows. Section 2.2 describes the datasets and analysis methods. Section 2.3 presents a comparison between observations with the simulations from both CMIP3 and CMIP5 in temperature variability during the 20th century. Section 2.4 shows the projected temperature trends in China for the 21st century. Sections 2.5 and 2.6 provide a discussion and a summary, respectively.

2.2. Data and Methods

2.2.1. Data

We obtained monthly surface air temperature output from 20 GCMs in the CMIP5 archive (Table 2.1). Four sets of experiments were used: one historical experiment for the 20th century, and three future emission scenarios for the 21st century. The historical experiment (HIST) provides simulations of surface temperature for 1850–2005 on the basis of observed natural and anthropogenic forcings. Future climate projections for 2006–2300 include three RCPs adopted by the IPCC AR5, including RCP 8.5, RCP 4.5, and RCP 2.6, which correspond to higher, medium, and lower greenhouse gas emissions, respectively. More specifically, the RCP 8.5 scenario assumes high population growth and high energy demand without climate change policies. It thus results in the pathway with the highest greenhouse gas emissions, brought about by a radiative forcing of 8.5 W/m^2 in 2100 (Riahi et al. 2011). Under RCP 4.5, radiative forcing stabilizes at 4.5 W/m^2 in 2100 without exceeding that value (Thomson et al. 2011), which results in a medium stabilization scenario. Finally, RCP 2.6 has a peak radiative forcing of ~3 W/m^2 before 2100 and then declines to 2.6 W/m^2 by 2100, making it a low emission scenario (Vuuren et al. 2011). To assess the potential improvements in CMIP5 compared with the earlier version, historical simulations of surface air temperature from 22 GCMs in the CMIP3 archive were also used. Monthly surface air temperature output from CMIP5 was obtained from http://cmip-pcmdi.llnl.gov/index.html. Output from the CMIP3 20th century experiment (20C3M) was obtained from the CMIP3 archive (http://esg.llnl.gov:8080/).

Table 2.1. Twenty CMIP5 GCMs used in our study and their forcings used for the historical simulations. Nat: natural forcing (e.g., solar and volcanic), Ant: anthropogenic forcing (e.g., well-mixed greenhouse gases, aerosols, ozone, and land-use changes), GHG: well-mixed greenhouse gases, SA: anthropogenic sulfate aerosol direct and indirect effects, SD: anthropogenic sulfate aerosol, accounting only for direct effects, Oz: ozone, LU: land-use change, Sl: solar irradiance, Vl: volcanic aerosol, SS: sea salt, Ds: dust, BC: black carbon, OC: organic carbon, MD: mineral dust, AA: anthropogenic aerosols.

Model	Spatial Resolution	Nat	Ant	GHG	SA	SD	Oz	LU	Sl	Vl	SS	Ds	BC	OC	MD	AA
ACCESS1.3	145×192			Y	Y		Y		Y	Y			Y	Y		
BCC-CSM1.1	64×128	Y	Y	Y		Y	Y		Y	Y	Y	Y	Y	Y		
CanESM2	64×128			Y	Y		Y		Y	Y			Y	Y		
CCSM4	192×288			Y		Y	Y	Y	Y	Y	Y	Y	Y	Y	Y	Y
CESM1(CAM5)	192×288			Y		Y	Y	Y	Y	Y	Y	Y	Y	Y	Y	Y
CMCC-CESM	48×96	Y	Y	Y	Y		Y		Y							
CNRM-CM5	128×256			Y	Y				Y	Y			Y	Y		
CSIRO-Mk3.6.0	145×192	Y	Y													
EC-EARTH	160×320	Y	Y													
FGOALS-g2	60×128			Y	Y		Y		Y	Y	Y	Y	Y	Y		
GFDL-CM3	90×144			Y	Y		Y	Y	Y	Y	Y		Y	Y	Y	
GISS-E2-H	90×144			Y	Y		Y	Y	Y	Y			Y	Y		
HadGEM2-CC	73×96			Y	Y		Y	Y	Y	Y			Y	Y		
INM-CM4[1]	120×180															
IPSL-CM5A-LR	96×96	Y	Y	Y	Y		Y	Y			Y	Y	Y	Y	Y	Y
MIROC-ESM	128×256			Y	Y		Y	Y	Y	Y			Y	Y	Y	
MIROC5	128×256			Y	Y		Y	Y	Y	Y	Y	Y	Y	Y	Y	
MPI-ESM-LR	96×192			Y	Y	Y	Y		Y	Y			Y	Y		
MRI-CGCM3	160×320			Y	Y		Y	Y	Y	Y			Y	Y		
NorESM1-M	96×144			Y	Y		Y		Y	Y			Y	Y		

[1] Forcing information for INM-CM4 is not available

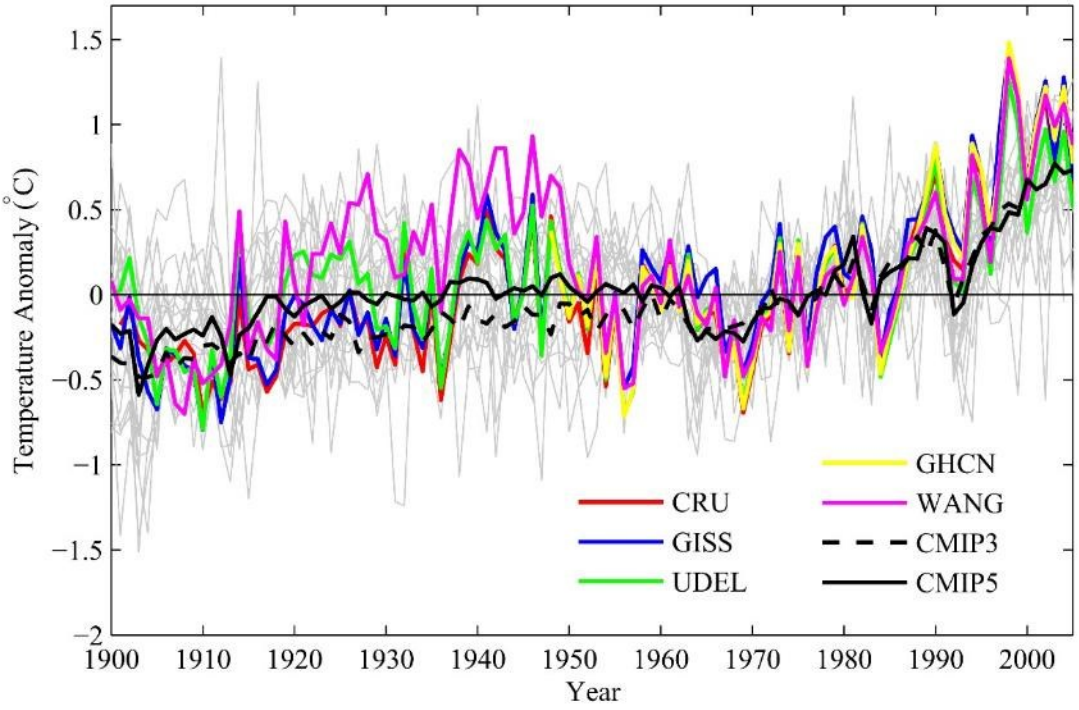

Figure 2.1. Time series of average annual temperatures derived from CRU, GISS, UDEL, GHCN, WANG, and the CMIP3 and CMIP5 multimodel ensemble averages for China. The grey lines correspond to the individual CMIP5 GCMs.

To ensure our study is not biased by the choice of observational datasets, two surface air temperature products were used to evaluate model performance. The Climatic Research Unit (CRU) time-series (TS) 3.10 dataset from the University of East Anglia provides monthly mean temperature for the global land surface at 0.5° × 0.5° resolution for the period 1901–2009 (Harris et al. 2014). This dataset is widely used for assessing climate variability and validating climate models at regional scales (Giorgi et al. 2004; Jacob et al. 2007; Xu et al. 2009). The second observational dataset is the 1900–2010 gridded air temperature time series data version 3.01 (referred to as UDEL from hereon), developed by (Willmott and Robeson 1995). This data archive contains terrestrial monthly air

temperature with 0.5° × 0.5° resolution, which is derived from the Global Historical Climatology Network (GHCN) version 2 and other mean monthly surface air temperature station records (Legates and Willmott 1990a; Legates and Willmott 1990b). Other globally gridded air temperature products are also available, such as the NASA Goddard Institute for Space Studies (GISS) surface temperature analysis, and GHCN itself (part of UDEL). GISS provides global surface temperature anomalies (2° × 2°) since 1880 (Hansen et al. 2010), while GHCN combines two individual observational datasets and contains global land surface temperatures with a high resolution (0.5° × 0.5°) since 1948 (Fan and van den Dool 2008). However, GISS temperatures are not spatially continuous in the early part of the 20th century, and the GHCN product only begins in 1948. However, with the exception of the 1915–1930 period, these products all agree reasonably well (Figure 2.1). We therefore focus on CRU and UDEL because they are both spatially and temporally complete from 1901 onward. Additionally, observational time series of annual mean surface air temperature over China were used to further validate the reliability of the two global observational temperature datasets at a regional scale. This dataset (hereafter referred to as WANG) was constructed based on temperature observations, documentary records, ice core data, and tree ring data over China for the period 1880–2009 (Gong and Wang 1999; Wang and Gong 2000; Wang et al. 2001; Wang et al. 1998). However, it is only available for surface air temperatures at the mean annual scale, hence it cannot be used for the seasonal analysis.

2.2.2. Methods

Based on the temporal coverage of observations and the CMIP5 output, the period 1901–2005 was extracted from the HIST simulations, and the period 2006–2100 was extracted from the three RCP experiments. Because the CRU observations start from 1901 and most of the CMIP3 20C3M simulations end in 1999, therefore, our 20th century analysis focuses on the period 1901–1999, and the second half of 20th century analysis focuses on the period 1950–1999. Due to the different spatial resolutions adopted by different GCMs (shown in Table 2.1), we used bilinear interpolation to regrid all GCM output into a uniform resolution (2.5° × 2.5°). Some modeling groups provide multiple realizations for each experiment (for instance, there are 6 runs for the HIST experiment in the CCSM4 output). To avoid potentially biasing our results with respect to one randomly selected realization, all available realizations were used and ensemble averages were calculated for each model. The multimodel ensemble averages of CMIP3 and CMIP5 were then created. From here on, "CMIP3" and "CMIP5" refer to these multimodel ensembles. CMIP3 and CMIP5 were compared with the two observational products to assess the performance of CMIP5, as well as CMIP5's potential improvements over CMIP3. Furthermore, the HIST simulation of each CMIP5 GCM was compared individually with observations to investigate the agreement among different models.

Linear trends were calculated to estimate the long-term trends in monthly, seasonal, and annual temperature for China during the 20th and 21st centuries. For the evaluation and comparison of GCMs, several statistical measures were used in this paper including mean error (ME), mean absolute error (MAE), standard deviation of the error (SDE), root

mean square error (RMSE), and Pearson's correlation coefficients (R). Temperature over the whole domain of China was calculated by averaging the grid cell values within the political boundaries (land areas) of China. To further assess the regional historical and future temperatures, four regions of China were selected: the north (35–43°N, 102.5–122.5°E), south (22–35°N, 102.5–122.5°E), northwest (38–48°N, 73–102.5°E), and the Tibetan Plateau (28–38°N, 80–102.5°E). Regional temperature trends were calculated as the area average for each region. Due to the likely shortcomings in the observations prior 1950s, model performance was also assessed for the second half the 20th century separately.

2.3. Temperature in the 20th Century

Figure 2.1 compares annual temperature anomalies (departures from 1961–1990 baseline) derived from observations and CMIP3 and CMIP5 multimodel ensemble averages for all of China. The CRU and UDEL observations exhibit good agreement after the 1930s ($R = 0.98$, $p<0.01$). However, when the station network was sparse before 1930, discrepancies exist between the observations. Also included here are the GISS, GHCN, and WANG observations for comparison. CRU shows better agreement with the other two observational products than UDEL. The 1901−2000 correlation of CRU and UDEL with GISS is 0.97 and 0.95, respectively. The CRU and UDEL correlations with GHCN are both 0.99 for the period 1951−2000, although this slightly higher correlation is likely due to the greatly enhanced station coverage during 1951–2000. Compared with the WANG observations, both CRU and UDEL show large discrepancies before 1950. The 1901–1950

correlation of CRU and UDEL with WANG is 0.49 and 0.45, respectively. In the WANG time series, temperature increased from the 1910s with a peak in the 1940s. This peak was also reported in other observed time series of surface air temperature over China (Tang and Ren 2005). Time series from all global datasets also indicate a warming peak in the 1940s, however, with a smaller magnitude. After 1950, both CRU and UDEL show good agreement with WANG, with 1951−2000 correlations of 0.98 and 0.97. Therefore, this time series comparison (Figure 2.1) between all the observational data products supports our choice of CRU and UDEL for subsequent evaluations. However, it is obvious that large uncertainties in temperature variability exist prior to 1950 in the currently available observational datasets. A separate model evaluation for 1951–2000 is therefore needed, in addition to the 20th-century assessment.

Evaluating the model simulations, both CMIP3 and CMIP5 illustrate an overall warming trend throughout 20th century. However, interannual variability in temperature is obvious for the individual models, but is suppressed by the multimodel ensemble averages. For instance, the multimodel ensemble average did not reproduce the highest annual temperature in 1998 as indicated by the observations. Interdecadal variability also appears muted in CMIP3 and CMIP5. For instance, neither the CMIP3 nor CMIP5 models capture the observed warming during 1920–1930. The accelerated warming trend evident in the observations since the 1970s is also underestimated in the multimodel ensembles, i.e. observed warming in China outpaced model simulations. The annual mean temperature climatology for the 1961–1990 baseline was 5.40°C in CMIP5 and 5.15°C in

CMIP3. Comparing CMIP3 and CMIP5 shows that CMIP3 has a consistent cold bias in China relative to CMIP5 before the 1960s.

Table 2.2. Annual and seasonal temperature means and trends for China during the 20th century derived from UDEL and CRU observations, and CMIP3 and CMIP5 multimodel ensemble averages. Statistically significant differences or trends (95% level) are shown in bold.

	Annual	Spring	Summer	Autumn	Winter
	Mean Temperature (°C)				
CRU	7.11	7.82	19.29	7.85	−6.52
UDEL	6.92	7.89	19.48	7.55	−7.24
CMIP3	5.04	5.50	17.94	5.53	−8.80
CMIP5	5.38	6.03	18.42	5.72	−8.66
	Temperature Difference (°C)				
CRU−UDEL	**0.19**	−0.07	**−0.19**	**0.29**	**0.72**
CMIP3−CRU	**−2.07**	**−2.31**	**−1.34**	**−2.32**	**−2.28**
CMIP5−CRU	**−1.73**	**−1.78**	**−0.87**	**−2.13**	**−2.14**
CMIP3−UDEL	**−1.88**	**−2.39**	**−1.54**	**−2.02**	**−1.56**
CMIP5−UDEL	**−1.54**	**−1.86**	**−1.06**	**−1.84**	**−1.42**
CMIP5−CMIP3	**0.33**	**0.53**	**0.48**	**0.19**	**0.14**
	Pearson Correlation				
CRU and UDEL	**0.93**	**0.95**	**0.93**	**0.94**	**0.97**
CMIP3 and CRU	**0.70**	**0.50**	**0.33**	**0.43**	**0.46**
CMIP5 and CRU	**0.65**	**0.42**	**0.55**	**0.45**	**0.37**
CMIP3 and UDEL	**0.54**	**0.36**	0.18	**0.31**	**0.36**
CMIP5 and UDEL	**0.57**	**0.33**	**0.46**	**0.38**	**0.28**
CMIP5 and CMIP3	**0.85**	**0.73**	**0.79**	**0.79**	**0.74**
	1901–1999 Trend (°C (100 yr)$^{-1}$)				
CRU	**0.79**	**1.01**	0.18	**0.54**	**1.40**
UDEL	**0.48**	**0.65**	−0.05	0.31	**0.97**
CMIP3	**0.65**	**0.61**	**0.56**	**0.62**	**0.83**
CMIP5	**0.42**	**0.39**	**0.31**	**0.42**	**0.55**

We compared the CMIP3 and CMIP5 multimodel ensemble averages of annual and seasonal air temperature with CRU and UDEL observations in the 20th century (Table 2.2). Generally, the mean annual temperatures from both CMIP3 and CMIP5 are significantly lower than both observational products. These cold biases also exist in the seasonal temperatures. Compared with CMIP3, CMIP5 shows less bias relative to observations throughout the four seasons. Both CMIP3 and CMIP5 are significantly correlated with the two observational annual temperature averages (Table 2.2). The correlation of CMIP3 and CMIP5 with CRU is 0.70 and 0.65, respectively, and their correlation with UDEL is 0.54 and 0.57, respectively. This suggests that only 29–49% of the observational temperature variability is captured by the multimodel ensembles. For seasonal temperature, CMIP5 exhibits better agreement with observations in summer and fall, while CMIP3 is better in summer and fall. These seasonal correlations, although mostly statistically significant, are even weaker than the annual relationships and account for, at most, 31% of observed temperature variability. In summer, CMIP3 has no significant correlation with UDEL.

Linear trend analysis reveals that there are significant warming trends in annual temperatures during the 20th century from both observations and model simulations (Table 2.2). The CRU observations exhibit the largest warming rate of 0.79°C $(100\ yr)^{-1}$ for China, which is in line with rates of global temperature increases. The UDEL trend is only 0.48°C $(100\ yr)^{-1}$, which is due to the ~1915–1930 period when UDEL was anomalously warm compared to other observational products (except WANG, which shows a 20th century warming trend of only 0.38°C $(100\ yr)^{-1}$). CMIP3 and CMIP5

show warming rates of 0.64 and 0.40°C (100 yr)$^{-1}$, respectively. The greater CMIP3 trend is driven by its cold bias (relative to CMIP5) prior to ~1960. Seasonally, both the CRU and UDEL observations suggest that the largest warming trends in China occurred in winter and spring. Except for CRU (autumn), there is no significant increase in temperature in summer and fall, i.e. the annual warming in China is driven by changes in winter and spring. However, this seasonality in temperature trends was not well captured by CMIP3 or CMIP5. CMIP3 exhibits consistently larger warming trends than CMIP5, and these trends are statistically significant throughout all four seasons. The seasonal variability of temperature increases is much less than that in observations, although both CMIP3 and CMIP5 do also exhibit the most warming in winter. The winter warming in the models is only about half of the observed warming.

Given the denser observational station network and hence more reliable trend estimates after ~1950, temperature biases and trends during the second half of the 20th century were also calculated separately (Table 2.3). Both the observations and model simulations indicate increasing mean annual temperature. CMIP5 shows fewer cold biases than CMIP3 in both annual and seasonal temperatures. However, CMIP3 has higher correlations with the observations (including GHCN, GISS, and WANG) except for summer temperature. For annual temperature, CRU and UDEL show an accelerated warming of 0.20 and 0.16°C (10 yr)$^{-1}$, respectively, with the largest warming occurring in winter at a rate of 0.43 and 0.35°C (10 yr)$^{-1}$. Annual temperature trends were also calculated from GHCN and WANG, showing a warming rate of 0.20°C (10 yr)$^{-1}$ and 0.16°C (10 yr)$^{-1}$, respectively. However, there is no statistically significant trend during

summer for either of the observational products. Similar to the period of 1901–1999, both CMIP3 and CMIP5 underestimate the annual temperature trends and exhibit less seasonal variability.

Table 2.3. As Table 2.2 but for the second half of the 20th century (1950–1999).

	Annual	Spring	Summer	Autumn	Winter
	Mean Temperature (°C)				
CRU	7.24	7.99	19.27	7.90	-6.24
UDEL	6.97	7.97	19.41	7.55	-7.07
CMIP3	5.18	5.63	18.06	5.66	-8.62
CMIP5	5.45	6.10	18.46	5.78	-8.55
	Temperature Difference (°C)				
CRU−UDEL	**0.27**	0.02	**-0.14**	**0.35**	**0.83**
CMIP3−CRU	**-2.05**	**-2.36**	**-1.21**	**-2.24**	**-2.37**
CMIP5−CRU	**-1.79**	**-1.89**	**-0.81**	**-2.12**	**-2.31**
CMIP3−UDEL	**-1.79**	**-2.34**	**-1.35**	**-1.89**	**-1.54**
CMIP5−UDEL	**-1.52**	**-1.87**	**-0.96**	**-1.77**	**-1.48**
CMIP5−CMIP3	**0.26**	**0.47**	**0.40**	**0.12**	**0.07**
	Pearson Correlation				
CRU and UDEL	**0.98**	**0.99**	**0.98**	**0.98**	**0.99**
CMIP3 and CRU	**0.75**	**0.46**	**0.43**	**0.49**	**0.64**
CMIP5 and CRU	**0.66**	**0.33**	**0.53**	**0.45**	**0.49**
CMIP3 and UDEL	**0.69**	**0.39**	**0.37**	**0.39**	**0.58**
CMIP5 and UDEL	**0.62**	0.28	**0.49**	**0.37**	**0.45**
CMIP5 and CMIP3	**0.89**	**0.72**	**0.88**	**0.86**	**0.68**
	1950–1999 Trend (°C (10 yr)$^{-1}$)				
CRU	**0.20**	**0.19**	0.03	**0.17**	**0.43**
UDEL	**0.16**	**0.16**	0.01	**0.12**	**0.35**
CMIP3	**0.12**	**0.11**	**0.10**	**0.13**	**0.13**
CMIP5	**0.08**	**0.07**	**0.07**	**0.09**	**0.08**

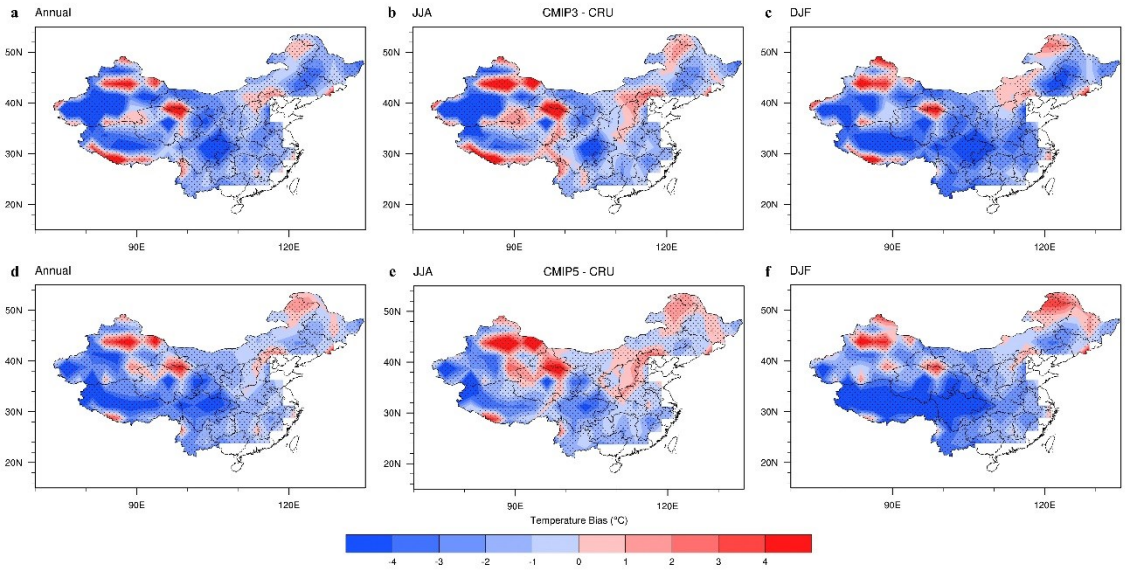

Figure 2.2. Annual and seasonal temperature biases of CMIP3 and CMIP5 relative to CRU observations. Top: the difference between CMIP3 and CRU, bottom: the difference between CMIP5 and CRU. The left column is annual temperature; the middle column is summer (JJA) temperature; and the right column is winter (DJF) temperature. Shaded regions indicate statistically significant differences (95% level).

To obtain a better sense of model variability within China, we also investigate the spatial variability of climatological annual mean temperature over the 20th century. We provide this assessment relative to the CRU observations only, because the UDEL spatial patterns are similar (not shown). We calculated the difference in annual and seasonal temperatures between CRU and CMIP3 (Figure 2.2a–c) and CMIP5 (Figure 2.2d–f). CMIP3 and CMIP5 show a similar spatial pattern of temperature bias relative to the CRU observations. Generally, cold biases exist over most parts of China, including the Tibetan Plateau, the central and southern region, and most of the north. Warm biases exist in the northeast and northwest. In CMIP3, there is a consistent warm bias along the southern

edge of the Tibetan Plateau, which does not appear in CMIP5. For both annual and seasonal temperatures, CMIP5 has a lower bias than CMIP3, especially over eastern China. In CMIP5, the largest cold bias occurs over the high elevations of the Tibetan Plateau in winter, while the largest warm bias occurs in the desert regions in northwestern China during summer. This suggests that in CMIP5, the cold regions are too cold during winter, while the warm regions are too warm during summer. We also calculated the inter-model standard deviations in annual and seasonal temperatures (not shown), and they exhibit a similar spatial pattern as the temperature bias. The regions with high inter-model standard deviations correspond to the regions of largest bias. The temperature biases for the second half of the 20th century show the same spatial pattern and are therefore not discussed here.

Figure 2.3 shows the spatial annual temperature trends over the 20th century based on observations and multimodel ensemble averages. Both CRU and UDEL show that the largest warming trend occurred in the northwest and northeast of China. However, in the UDEL observations, there is no significant warming trend over the Tibetan Plateau, but a significant cooling trend in central and southern China that is not captured by CRU. Compared with the observations, both CMIP3 and CMIP5 underestimated temperature trends over most regions of China. Spatial patterns of temperature trends in CMIP3 exhibit substantial disagreement with the observations. The largest warming trend occurred over the Tibetan Plateau, and there is significant warming in central and southern China. The spatial trend pattern is slightly improved in CMIP5, however, substantial discrepancies remain.

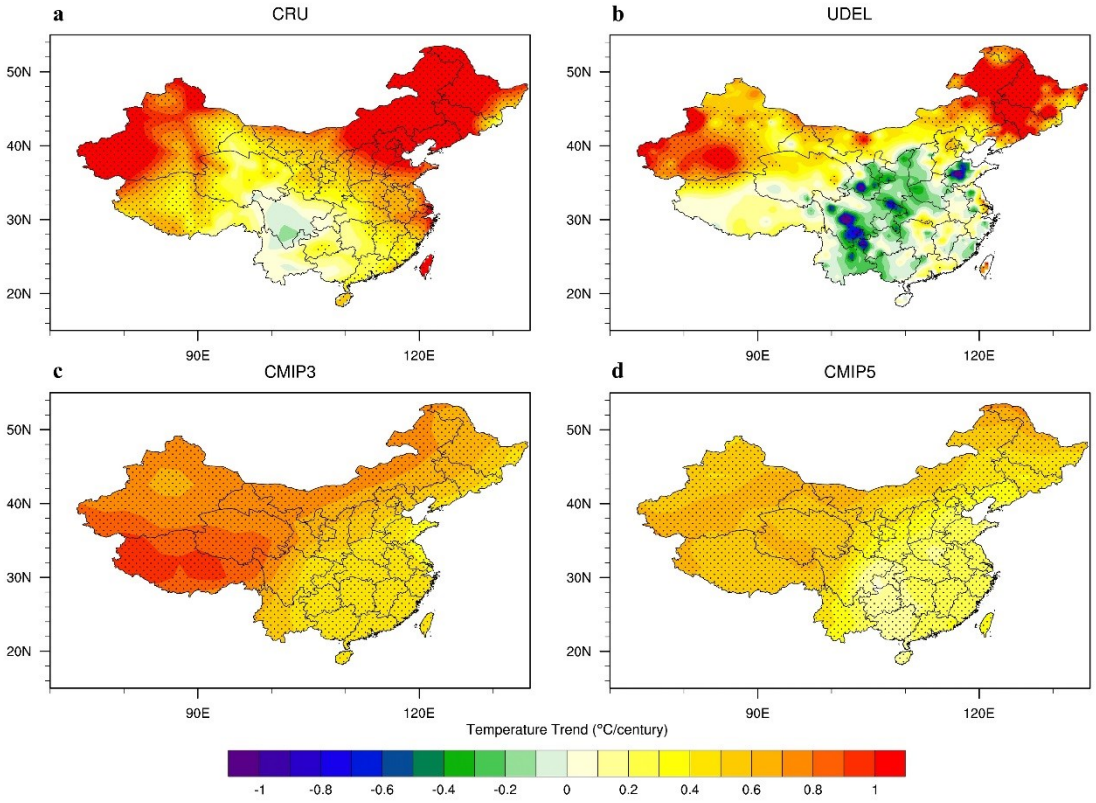

Figure 2.3. Trends in average annual temperatures over the 20th century derived from a) CRU and b) UDEL observations, and c) CMIP3, and d) CMIP5 multimodel ensemble averages. Shaded regions indicate statistically significant differences (95% level).

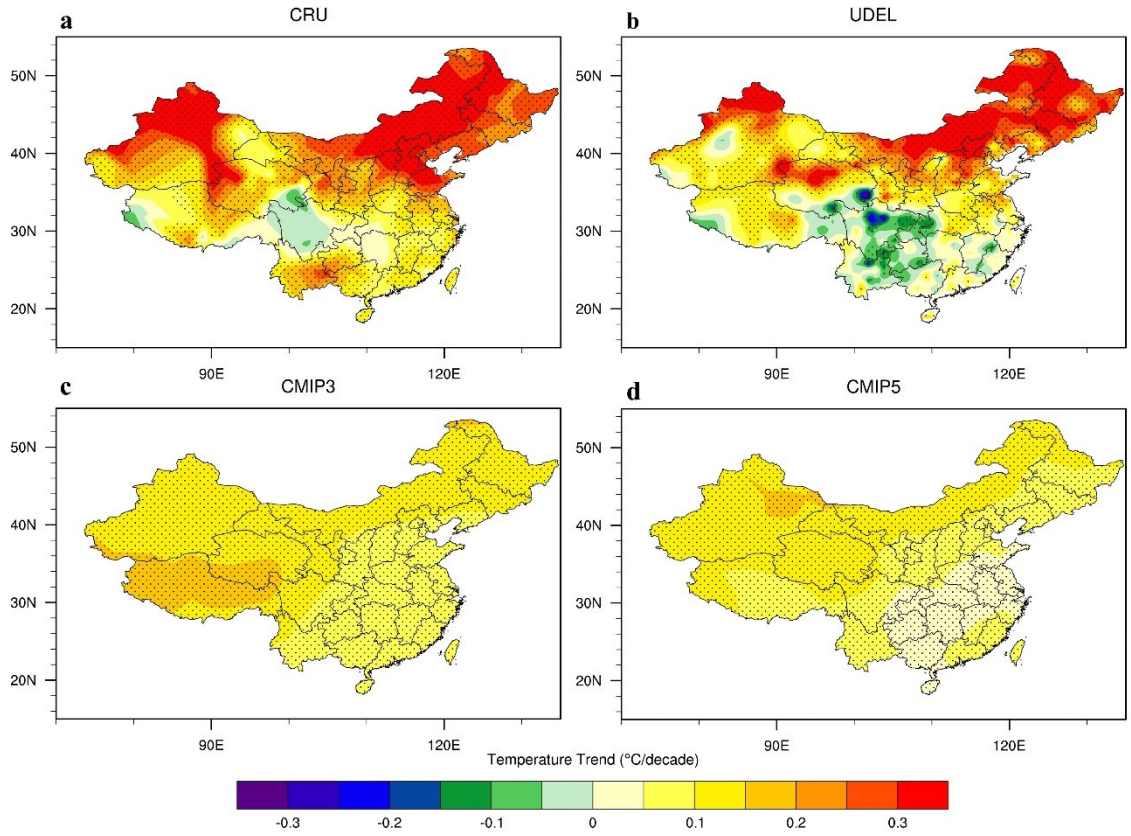

Figure 2.4. As figure 3 but for the second half of the 20th century (1950–1999).

Recognizing the inherent limitations in the observations in the early part of the 20th century, temperature trends for the second half of the 20th century were calculated (Figure 2.4). Over the past half century, there is accelerated warming over most regions of China. The two observational products show that the largest warming occurred in the northwest and northeast. There are significant warming trends over the Tibetan Plateau. In central China, especially over the Sichuan province, temperature tends to decrease. Disagreement in temperature trends also still exist over 1950–1999 between the two observational products. Over the south and southeast, CRU shows significant warming trends while

UDEL indicates cooling. As for the entire 20th century, both CMIP3 and CMIP5 underestimate the warming trends over the north, and cannot reproduce the cooling trends in central and southern China.

Table 2.4. Historical surface air temperature trends (°C (100 yr)$^{-1}$) in different sub-regions of China during the 20th century. Statistically significant trends (95% level) are shown in bold.

Regions	Data	Annual	Spring	Summer	Fall	Winter
North	CRU	**0.88**	**1.07**	0.06	**0.55**	**1.82**
	UDEL	0.17	0.32	**−0.46**	0.00	0.80
	CMIP3	**0.60**	**0.54**	**0.48**	**0.59**	**0.79**
	CMIP5	**0.37**	**0.31**	**0.21**	**0.37**	**0.57**
South	CRU	**0.40**	**0.53**	**0.31**	0.27	0.51
	UDEL	−0.04	0.03	−0.11	−0.12	0.02
	CMIP3	**0.46**	**0.45**	**0.46**	**0.37**	**0.56**
	CMIP5	**0.21**	**0.14**	**0.30**	**0.19**	**0.21**
Northwest	CRU	**0.94**	**0.95**	**0.47**	**0.71**	**1.58**
	UDEL	**0.74**	**0.73**	0.26	**0.70**	**1.21**
	CMIP3	**0.73**	**0.62**	**0.66**	**0.77**	**0.88**
	CMIP5	**0.53**	**0.45**	**0.40**	**0.54**	**0.72**
Tibetan Plateau	CRU	**0.39**	**0.48**	0.17	0.23	**0.66**
	UDEL	0.20	0.32	0.09	0.10	0.29
	CMIP3	**0.84**	**0.83**	**0.72**	**0.73**	**1.07**
	CMIP5	**0.54**	**0.69**	**0.42**	**0.50**	**0.55**

Annual and seasonal temperature trends were calculated for individual regions within China (Table 2.4). CRU shows statistically significant increases in annual temperatures in all four regions, with greater warming trends over the northeast and the northwest (0.88°C (100 yr)$^{-1}$ and 0.94°C (100 yr)$^{-1}$, respectively). In UDEL, the temperature increase is only statistically significant over the northwest at a rate of 0.74°C (100 yr)$^{-1}$. Compared with

the CRU observations, both CMIP3 and CMIP5 overestimate the warming trend over the Tibetan Plateau, and underestimate the warming trend over the northwest and northeast. Based on the two observational products, there is no significant seasonal warming trend in the northeast in summer, in the south in fall and winter, and in the Tibetan Plateau in summer and fall. However, both CMIP3 and CMIP5 exhibit significant warming trends in all four regions throughout the year.

Table 2.5. Same as Table 2.3 but for the second half of the 20th century (1950–1999).

Regions	Data	Annual	Spring	Summer	Fall	Winter
North	CRU	**2.60**	**2.55**	0.46	**2.14**	**5.30**
	UDEL	**2.29**	**2.10**	0.72	**1.77**	**4.57**
	CMIP3	**0.98**	**0.76**	**0.88**	**1.24**	**1.00**
	CMIP5	**0.72**	**0.58**	**0.61**	**0.88**	**0.72**
South	CRU	**1.00**	0.82	-0.08	**1.14**	**2.05**
	UDEL	0.23	0.03	-0.54	0.31	1.11
	CMIP3	**0.76**	**0.60**	**0.80**	**0.82**	**0.81**
	CMIP5	**0.39**	0.24	**0.47**	**0.58**	0.18
Northwest	CRU	**2.73**	**1.63**	0.34	**2.48**	**6.60**
	UDEL	**2.09**	1.17	0.28	**2.06**	**5.02**
	CMIP3	**1.33**	**1.21**	**1.17**	**1.54**	**1.41**
	CMIP5	**1.17**	**0.98**	**1.12**	**1.20**	**1.29**
Tibetan Plateau	CRU	**0.88**	0.40	0.04	0.91	**2.25**
	UDEL	0.69	0.60	0.14	0.58	**1.54**
	CMIP3	**1.49**	**1.65**	**1.18**	**1.36**	**1.75**
	CMIP5	**0.93**	**1.10**	**0.77**	**1.05**	**0.72**

The temperature trends over the second half of the 20th century indicate accelerated warming in annual mean temperature based on both observations and simulations (Table 2.5). The observed accelerated warming in the north is mainly attributed to greater

Table 2.6. Evaluation of individual CMIP5 GCMs relative to annual CRU temperatures based on Pearson's correlation coefficients (R), mean error (ME), mean absolute error (MAE), standard deviation of the error (SDE), and root mean square error (RMSE). Included also are the 20th century trends. Statistically significant differences, correlations, and trends (95% level) are shown in bold.

Simulation	R	ME (°C)	MAE (°C)	SDE (°C)	RMSE (°C)	Trend (°C (100 yr)$^{-1}$)
CMIP5	**0.66**	**−1.73**	1.73	0.31	17.58	**0.45**
ACCESS1.3	**0.25**	**−0.39**	0.47	0.43	5.81	−0.09
BCC-CSM1.1	**0.58**	**−1.96**	1.96	0.35	19.89	**0.98**
CanESM2	**0.57**	**−0.52**	0.53	0.33	6.13	**0.34**
CCSM4	**0.61**	**−1.36**	1.36	0.34	14.06	**0.97**
CESM1(CAM5)	**0.48**	**−1.53**	1.53	0.36	15.68	**0.37**
CMCC-CESM	0.12	**−1.13**	1.16	0.56	12.65	0.22
CNRM-CM5	**0.47**	**−3.15**	3.15	0.35	31.69	**0.28**
CSIRO-Mk3.6.0	**0.47**	**−1.38**	1.38	0.36	14.21	**0.17**
EC-EARTH	**0.64**	**−1.98**	1.98	0.31	20.10	**0.96**
FGOALS-g2	**0.30**	**−4.12**	4.12	0.47	41.45	**0.68**
GFDL-CM3	0.17	**−2.10**	2.10	0.45	21.46	−0.17
GISS-E2-H	**0.39**	**−0.41**	0.45	0.37	5.49	**0.20**
HadGEM2-CC	0.10	**−2.32**	2.32	0.54	23.87	−0.23
INM-CM4	**0.25**	**−4.44**	4.44	0.51	44.66	**0.81**
IPSL-CM5A-LR	**0.68**	**−3.09**	3.09	0.32	31.10	**1.08**
MIROC5	**0.20**	**0.80**	0.82	0.42	9.02	−0.07
MIROC-ESM	**0.49**	**−0.74**	0.74	0.35	8.20	**0.28**
MPI-ESM-LR	**0.62**	**−0.45**	0.48	0.32	5.55	**1.05**
MRI-CGCM3	**0.46**	**−2.13**	2.13	0.37	21.59	**0.63**
NorESM1-M	**0.51**	**−2.23**	2.23	0.36	22.59	**0.52**

temperature trends in winter and spring, and in the northwest it is attributed to temperature increases in winter and fall. In the south, temperature increased in winter and fall, but decreased in summer. Over the Tibetan Plateau, there is no significant warming except in winter. However, neither CMIP3 nor CMIP5 reproduced the seasonality of the temperature trends in these regions. Model simulations show significant warming

throughout the four seasons, with the greatest warming occurring in fall while the observations indicate that winter warming is the greatest.

Using multimodel ensemble averages is a common approach because it is thought that noise in the predictions is thereby reduced. However, as illustrated for CMIP5 in Figure 2.1 (grey lines), there is a large amount of variability among the individual model ensembles that comprise a multimodel average. CMIP5 likely includes models that are well suited for capturing the temperature variability across China, in addition to potentially underperforming models. We therefore assess the individual GCMs relative to the CRU observations for annual temperature over the 20th century (Table 2.6), to identify the most suitable models for our particular region. The assessment is based on the strength of the correlation, as well as on various error measures. Comparisons with UDEL are similar to CRU, and are therefore not shown. Several models exhibit better agreement (higher correlations and smaller errors/biases) with the observations: MPI-ESM-LR, CanESM2, MIROC-ESM, and CCSM4. Even though IPSL-CM5A-LR and EC-EARTH show the highest correlations with the observations (0.68 and 0.66, respectively), large cold biases and RMSEs exist in these models. FGOALS-g2, INM-CM4, and IPSL-CM5A-LR have the largest cold biases, and MIROC5 is the only model with a warm bias. Among the 20 models, ACCESS1.3, CMCC-CESM, GFDL-CM3, HadGEM2-CC, and MIROC5 show no trend throughout the 20th century. The correlation coefficients demonstrate that CMCC-CESM and HadGCM2-CC, which have the coarsest spatial resolution among the 20 GCMs (Table 2.1), have the largest disagreement with temperature observations in China.

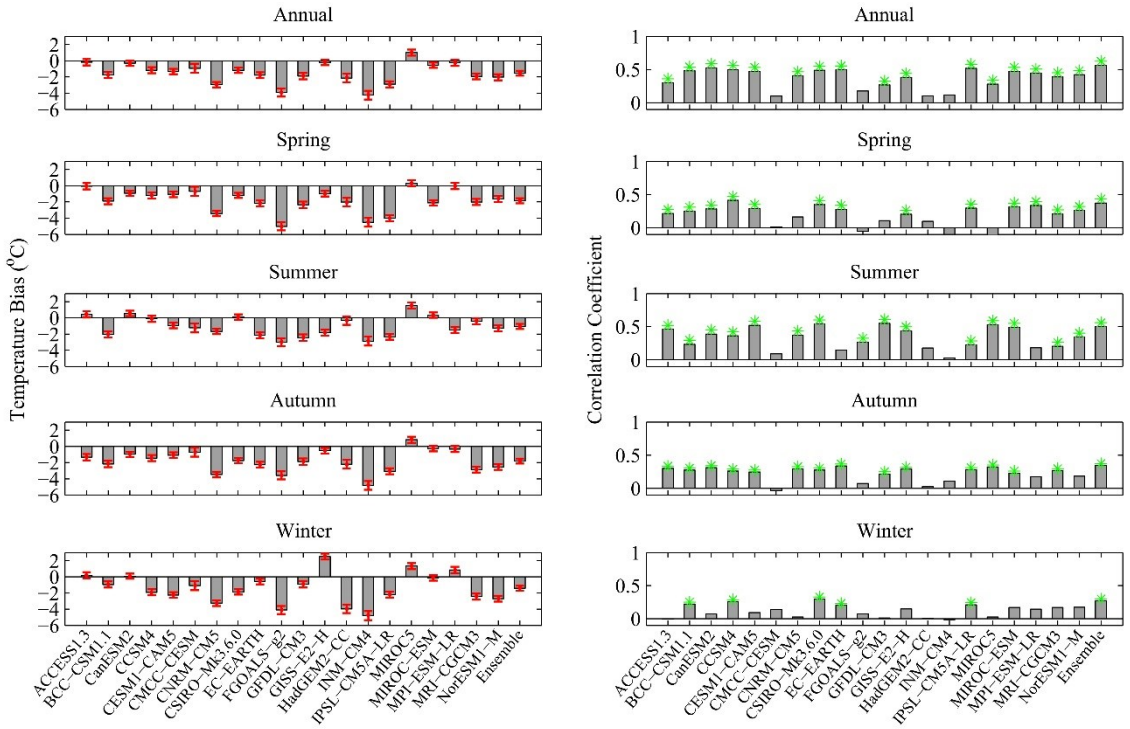

Figure 2.5. Comparison between CRU observations and individual CMIP5 GCMs for annual and seasonal temperatures: temperature bias from observations (left) and correlations between observations and individual models (right). Error bars indicate standard deviation of temperature biases, green stars indicate significant (95% level) correlations.

The individual models' performance was also compared with observations for the four seasons (Figure 2.5). The agreement between models and observations varies through the seasons. Most models show good agreement with CRU in summer. However, only six models exhibit significant correlations with the observations in winter. Individual models were also evaluated by comparing simulated surface air temperatures relative to CRU, UDEL, and WANG observations for the second half the 20th century (not shown). The models exhibit the same agreement as over the entire 20th century.

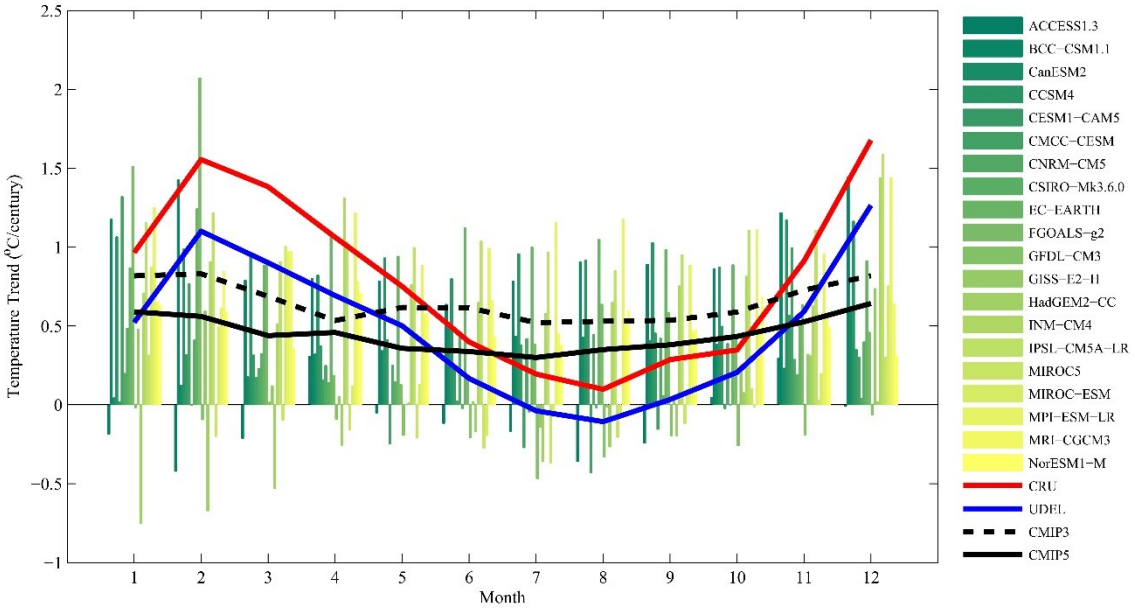

Figure 2.6. Trends in seasonal temperatures over the 20th century for China derived from CRU and UDEL observations, and CMIP3 and CMIP5 multimodel ensemble averages (color bars indicate temperature trends derived from the individual CMIP5 models).

To investigate the seasonal variability in temperature trends during the 20th century, we calculate the monthly temperature trends from CRU and UDEL observations, CMIP3 and CMIP5 multimodel ensemble averages, and the individual GCMs (Figure 2.6). Between the two observational products, CRU consistently has a greater warming trend than UDEL throughout the year. As discussed before, the two observational products exhibit a clear seasonality in temperature trends for China. Larger warming trends occurred in the cold season, and less warming or even cooling trends occurred in the warm season. However, this seasonality was not captured by CMIP3, and CMIP5 also only shows a very weak seasonal pattern in temperature trends. As was the case for the annual and seasonal trends, CMIP5 trends are lower than CMIP3 for all individual months of the

year. Based on the monthly temperature trends in the individual GCMs, some models show cooling trends during most parts of the year, including ACCESS1.3, GFDL-CM3, HadGEM2-CC, and MIROC5. Several individual models did capture the seasonality shown by the observations, including BCC, CCSM4, CMCC-CESM, CSIRO-Mk3.6, GISS-E2-H, and MIROC-ESM. However, despite capturing the seasonality of the trends, the magnitude is generally much lower. For the period 1950–1999, both CRU and UDEL exhibit temperature increases for all months, with the greatest warming in February, December, and January, and the least warming in August, July, and June. As for the entire 20th century, both CMIP3 and CMIP5 show a much weaker annual cycle. Some models do not capture the accelerated warming in winter months, such as HadGEM2-CC, GFDL-CM3, and MIROC5.

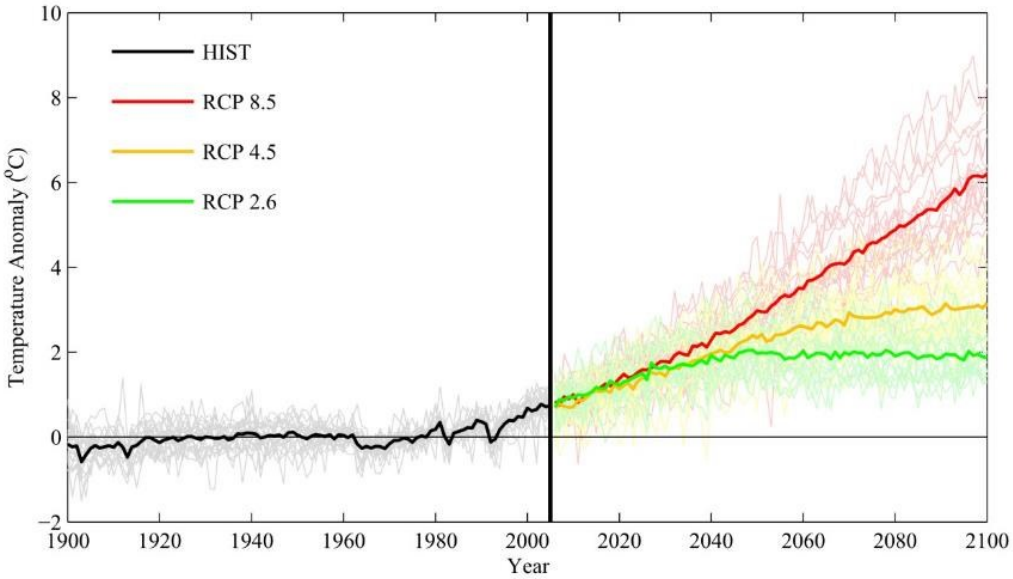

Figure 2.7. Time series of historical and projected temperature for China from different CMIP5 experiments during 1900–2100.

Table 2.7. Projected warming in different sub-regions of China during the 21st century, and the temperature change for 2090−2099 relative to 1980−1999. All trends and changes are statistically significant (95% level).

Experiments	Regions	Temperature Trend (°C (10 yr)$^{-1}$)	Temperature Change (°C)
RCP 2.6	China	0.10 ± 0.05	1.78 ± 0.56
	North	0.11 ± 0.05	1.91 ± 0.57
	South	0.11 ± 0.05	1.78 ± 0.67
	Northwest	0.10 ± 0.05	1.95 ± 0.56
	Tibetan Plateau	0.09 ± 0.06	1.49 ± 0.54
RCP 4.5	China	0.27 ± 0.07	2.84 ± 0.73
	North	0.27 ± 0.07	2.87 ± 0.76
	South	0.25 ± 0.07	2.52 ± 0.67
	Northwest	0.28 ± 0.07	3.12 ± 0.81
	Tibetan Plateau	0.29 ± 0.09	2.89 ± 1.17
RCP 8.5	China	0.60 ± 0.14	5.66 ± 1.05
	North	0.59 ± 0.14	5.59 ± 1.07
	South	0.53 ± 0.13	4.90 ± 0.95
	Northwest	0.64 ± 0.16	6.22 ± 1.20
	Tibetan Plateau	0.63 ± 0.17	5.96 ± 1.14

2.4. Temperatures in the 21st Century

The projected future temperatures for China as a whole under three emission scenarios is shown in Figure 2.7. RCP 8.5 and RCP 4.5 exhibit a gradual increase in annual temperature during the 21st century at a rate of 0.60°C (10 yr)$^{-1}$ and 0.27°C (10 yr)$^{-1}$, respectively. As the lowest-emission mitigation scenario, the RCP 2.6 experiment projects the lowest rate of temperature increase (0.10°C (10 yr)$^{-1}$). By the end of the 21st century, temperature will increase by 1.78−5.66°C over China (Table 2.7). Under the RCP 2.6 scenario, temperature will increase until 2040, and then remain stable or even decrease slightly. This indicates the effectiveness of anticipated climate mitigation strategies, while

largely reflecting the design of the RCP scenarios in terms of the radiative forcing (see section 2.1). Additionally, in the near-term (before the 2030s) the temperature increase under RCP 2.6 is greater than under RCP 4.5, even though its radiative forcing is lower than RCP 4.5.

Figure 2.8 illustrates the spatial pattern of annual temperature change over China during the 21st century under the three emission scenarios. Interestingly, there is not a common spatial pattern in temperature trends among the three scenarios (Figure 2.8 a–c). RCP 2.6 shows the greatest warming across eastern China, as well as in some isolated regions in the Himalayas and northwestern China. However, the greatest warming under the RCP 4.5 scenario will occur on the western Tibetan Plateau, while drastic countrywide warming is projected for RCP 8.5. We also calculated the temperature difference between the period 2070–2099 and 1961–1990 (Figure 2.8 d–e), to determine where changes will be greatest relative to the 20th century. We find significantly higher temperature in the late 21st century compared to the three decades in the late 20th century. Unlike the trend patterns, the temperature differences exhibit a somewhat consistent spatial pattern among the three scenarios. For RCP 4.5 and 8.5, the greatest temperature increase will occur over the Tibetan Plateau, the northwest, and the northeast, with smaller increases over eastern China. While the temperature changes are of course smallest under the RCP 2.6 scenario, the Tibetan Plateau would experience relatively smaller temperature changes than the northwest and northeast, with east-central China also being part of this greater warming region. Table 2.7 shows projected temperature changes in the different sub-regions of China under the 3 emission scenarios. For RCP 2.6, there are similar temperature trends

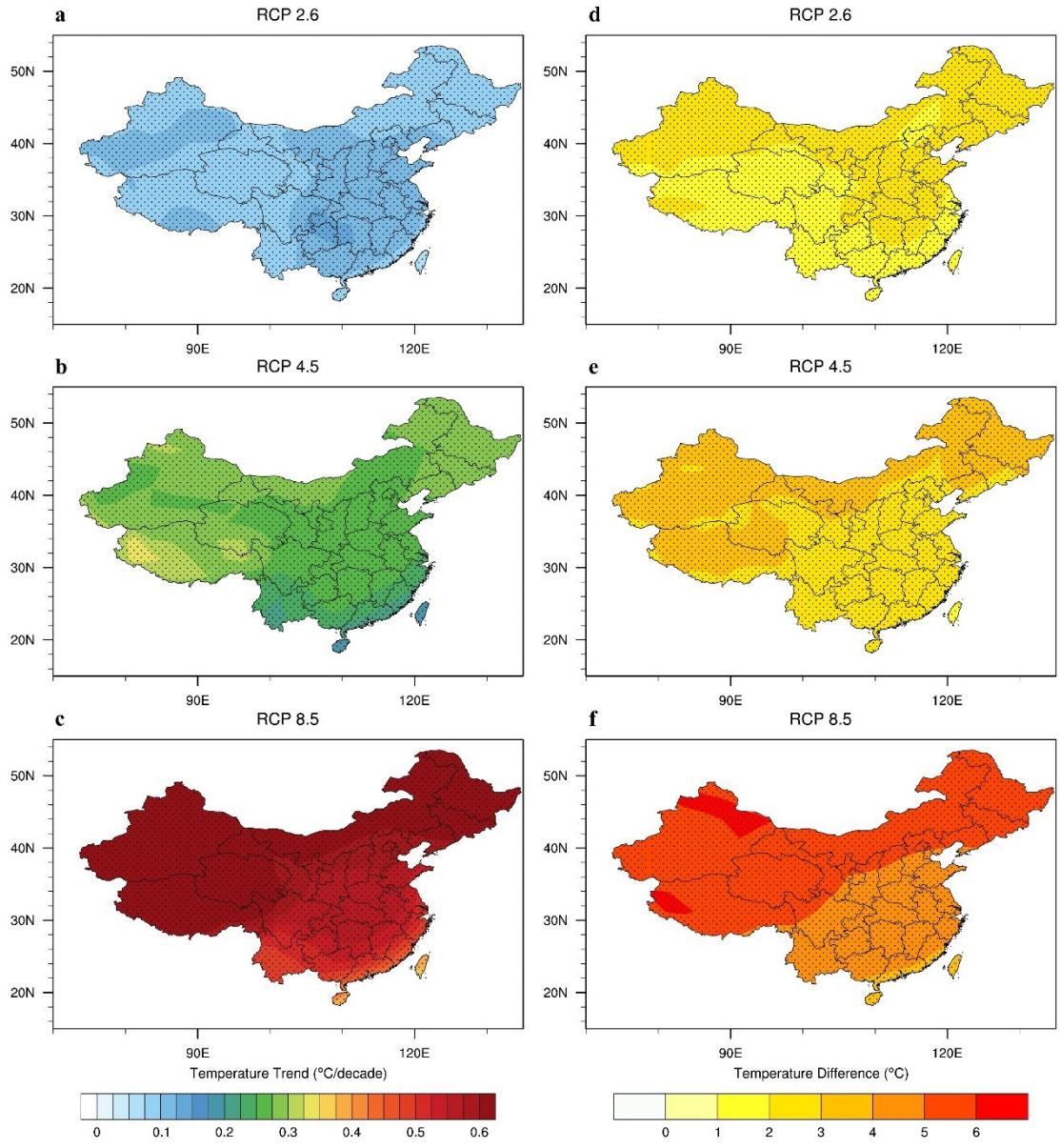

Figure 2.8. Annual temperature trends for the 21st century for three emission scenarios (left) and changes in annual temperature (2070–2099 versus 1961–1990) based on CMIP5 projections (right). Shaded regions indicate statistically significant trends/differences (95% level).

in the four sub-regions, with a slightly greater increase over the northwest and northeast (~1.9°C warming by the end of 21st century). With the increase in radiative forcing in future projections, the northwest and the Tibetan Plateau will have a larger warming trend, and the northwest will experience the greatest temperature increase, 3.1°C and 6.2°C for RCP 4.5 and RCP 8.5, respectively.

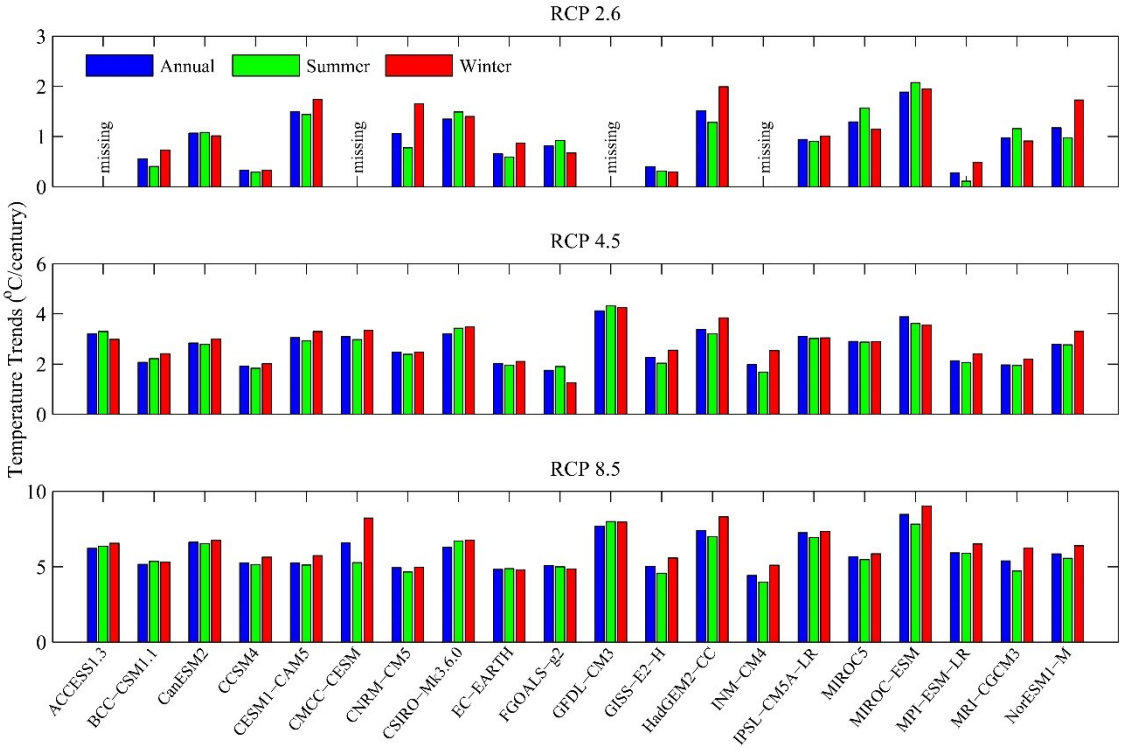

Figure 2.9. Trends in annual and seasonal temperatures over the 21st century derived from individual GCMs for the three experiments.

Figure 2.9 shows the annual as well as the winter and summer temperature trends in the individual CMIP5 GCMs for the 21st century. The variability of temperature trends

among the 20 models shows virtually the same pattern under the three scenarios. Several models project greater rates of temperature increase than others, such as CMCC-CESM, CSIRO-Mk3.6, GFDL-CM3, HadGEM2-CC, and MIROC-ESM. It is unclear which of these 21st century trend projections may be the most reliable, given that those models that agreed best with observations in terms of the mean climate states (see Table 2.6, e.g., MPI-ESM-LR, CanESM2, MIROC-ESM, and CCSM4) nonetheless did not capture the observed 20th century trends. There is also limited agreement in the seasonal patterns of future temperature trends among the 20 GCMs. For instance, CMCC-CESM, HadGEM2-CC, and NorESM1-M exhibit much higher winter warming while some other models show no obvious difference in temperature trends between the two seasons. This disagreement is evident for all three scenarios. For MIROC-ESM, there is much greater warming in winter than in summer for RCP 8.5. However, under RCP 4.5 and RCP 2.6, the warming trend is greater in summer relative to winter.

An additional interesting observation regarding the modeled trends is that, when compared to trends in the HIST experiment, the models with the lower temperature trends during the 20th century usually exhibit greater warming trends during the 21st century. Figure 2.10 illustrates the significant negative correlation between the historical and RCP 4.5 projected temperature trends ($R=-0.70$, $p<0.01$). The negative relationship also exists for the RCP 2.6 and RCP 8.5 experiments, but is not as strong as for RCP 4.5.

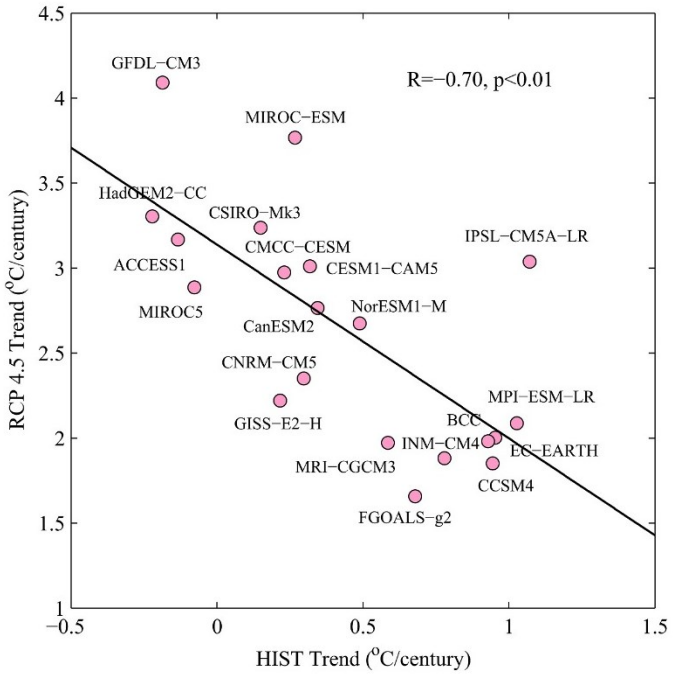

Figure 2.10. Scatterplot of historical temperature trends during the 20th century and the projected temperature trend under the RCP 4.5 scenario.

2.5. Discussion

The objective of this study is to evaluate CMIP5's performance in simulating surface air temperature during the 20th century, relative to two observational datasets. Compared with UDEL, CRU shows a stronger warming trend during the 20th century of 0.79°C (100 yr)$^{-1}$, while UDEL only shows ~60% of that warming trend (0.48°C (100 yr)$^{-1}$). This discrepancy between the two observational products can be attributed to two factors. First, as mentioned in section 2.2, different data sources were assimilated into the respective databases. Second, these two datasets were generated based on different interpolation methods. Based on four different observational datasets, Zhao et al. (2005) suggested that the country-averaged annual mean surface air temperature has increased at a rate of 0.2–

0.8°C (100 yr)$^{-1}$ from 1901 to 1999. Greater warming trends, 0.3–1.2°C (100 yr)$^{-1}$, were detected for the period 1906–2005 (Ren et al. 2012). Based on previous studies (e.g.,(Hu et al. 2003), there was a pronounced warming from 1951 to 2000 in the entire country in winter, spring, and autumn, particularly in the north. There was also a summer cooling trend reported for central China. These conclusions agree well with the results from CRU and UDEL. Therefore, CRU and UDEL provide reasonable observational temperature trends, and are likely valid for our model evaluation.

In our results, both CMIP3 and CMIP5 show a smaller warming trend than CRU observations. CMIP3 shows a more consistently linear warming trend during the whole century than CMIP5. This is also found by Knutti and Sedlacek (2013) who explain that the 20th century historical simulations in CMIP5 included more diverse and complete radiative forcings (shown in Table 2.1), but some models in CMIP3 did not consider solar and volcanic forcings, or aerosol effects. Zhou and Yu (2006) found that there is a significant correlation between CMIP3 simulations and observed annual temperatures over all of China. However, most of the CMIP3 models failed to reproduce the summertime cooling trend in the middle part of eastern China, and many models underestimate the winter warming trend. Our CMIP3 results agree well with these findings. However, our findings for CMIP5 indicate little improvement in simulating the spatial and seasonal patterns of temperature trends.

Compared with observations, there is a significant cold bias over the Tibetan Plateau where we also observe the largest inter-model variation. This disagreement implies a common deficiency among the CMIP5 models still exists for reproducing atmospheric

processes in such a highly spatially-heterogeneous and complex terrain. These cold biases have also been reported in previous studies. Substantial cold biases were found over high plateaus, especially the Tibetan Plateau, in GCM simulations (Annan et al. 2005; Gao et al. 2010; Ji and Kang 2012; Su et al. 2012). Seasonally, this cold bias is largest during the cold season and smallest in the warm season, implying that models may fail to represent snow-albedo feedbacks over this mountain region. Additionally, previous studies suggest that model deficiencies in simulating cloud properties over the plateau may introduce insufficient plateau heating, therefore resulting in temperature biases over the Tibetan Plateau (Zhou and Li 2002; Yu et al. 2004).

Based on our model evaluation, several CMIP5 models were identified as the most suitable models for China, including MPI-ESM-LR, CanESM2, MIROC-ESM, and CCSM4. Before CMIP5 had been completed, Chen et al. (2011) evaluated 28 atmosphere-ocean GCMs and five models were identified with better performance over China, including the ECHAM4 (INGV ECHAM4), the third climate configuration of the Met Office Unified Model (UKMO HadCM3), the CSIRO Mark version 3.5 (Mk3.5), the NCAR Community Climate System Model, version 3 (CCSM3), and the Model for Interdisciplinary Research on Climate 3.2 (MIROC3.2). Except for CanESM2, MPI-ESM-LR, MIROC-ESM, and CCSM4 still show the same good results as their earlier versions, indicating a consistently better performance of these models (MPI-ESM and MIROC-ESM are new earth system models incorporating ECHAM and MIROC, respectively). MPI-ESM-LR and CanESM2 were also ranked in the top five of the best models in simulating temperature over the Tibetan Plateau by Su et al. (2012).

Future temperature projections show that there will be continued warming over China. The greatest warming trend will occur over northern China and the Tibetan Plateau. However, these spatial trend patterns appear to be the least reliable statistics calculated from the CMIP5 archive. Severe temperature increases such as the ones projected as part of RCP 8.5 will probably aggravate environmental degradation in the northern China, such as drought and desertification, which have been documented to be serious problems already (Wang et al. 2008). Over the Tibetan Plateau, which is called the "third pole" of the earth, glacier retreat has occurred since the 1960s and has intensified in the past 10 years (Yao et al. 2007). Since the Tibetan Plateau is the source region for many of the major rivers of China, further warming may generate substantial hydrological impacts over China.

2.6. Conclusions

This study evaluated 20 CMIP5 GCMs' performance in simulating surface air temperature variability over China during the 20th century with respect to two observational datasets. For seasonal and annual mean temperatures, GCMs show substantial cold biases over the Tibetan Plateau, especially in the cold season. These cold biases over the Tibetan Plateau are also characterized by the greatest disagreement among the individual models, indicating GCMs' deficiencies in reproducing climatic features in this complex, high elevation terrain. CMIP5 shows slightly better agreement with observations than CMIP3 in terms of temperature biases. Both CMIP3 and CMIP5 exhibit climatic warming over the 20th century with an accelerated warming during the second

half of the century. However, annual mean temperature trends are underestimated, and the seasonal trends are poorly simulated. The spatial pattern of temperature trends over China is also not simulated well.

Based on six statistical measures, four CMIP5 models better simulate historical surface air temperature variability over China: MPI-ESM-LR, CanESM2, MIROC-ESM, and CCSM4. The two observational products both exhibit clear seasonality in temperature trends during the 20th century: larger warming trends occurred in cold season, with less warming trend or cooling during the warm season. However, the multimodel ensembles (both CMIP3 and CMIP5) as well as most individual GCMs did not capture this seasonal pattern, in particular ACCESS1.3, GFDL-CM3, HadGEM2-CC, and MIROC5.

The future temperature projections for China indicate that the RCP 8.5 and RCP 4.5 scenarios exhibit a consistent increase in annual temperature during the 21st century at a rate of 0.60°C $(10\ yr)^{-1}$ and 0.27°C $(10\ yr)^{-1}$, respectively. The lowest-emission mitigation scenario, RCP 2.6, produces the lowest rate of warming (0.10°C $(10\ yr)^{-1}$), all of which is projected to occur by approximately 2040. By the end of the 21st century, temperature is projected to increase by 1.7−5.7°C, with the larger warming over northern China and the Tibetan Plateau.

3. A COMPREHENSIVE EVALUATION OF PRECIPITATION SIMULATIONS OVER CHINA BASED ON CMIP5 MULTIMODEL ENSEMBLE PROJECTIONS*

3.1. Introduction

Precipitation is a key component in the climate system and represents a crucial link between the atmosphere, hydrosphere, and biosphere. Climate change and the associated precipitation variability produce substantial impacts on both natural environments and human society. The Intergovernmental Panel on Climate Change (IPCC) Fifth Assessment Report (AR5) indicates that the global average surface temperature has increased by 0.85 [0.65 to 1.06]°C over the period 1880−2012, with additional warming of 0.3°C to 0.7°C for the period 2016−2035 relative to the reference period of 1986−2005 (IPCC 2013). On the other hand, precipitation has likely increased since 1901 over the mid-latitude land areas of the Northern Hemisphere (IPCC 2013). Temporally, there is a slight upward trend in global annual mean land precipitation, however, with large inter-decadal variability because of the El Niño-Southern Oscillation (ENSO) and changes in atmospheric circulation patterns such as the North Atlantic Oscillation.

China is one of the most populous countries in the world. Climate change and especially precipitation variations are of particular importance due to the vulnerability of water resources in this region (Vörösmarty et al. 2000). Water availability plays an important role in agricultural and industrial development, which guarantees food supplies

* This section is reprinted with permission from "A Comprehensive Evaluation of Precipitation Variability over China Based on CMIP5 Multimodel Ensemble Projections" by Chen and Frauenfeld, 2014. *Journal of Geophysical Research-Atmospheres*, 119, 5767–5786, Copyright [2014] by John Wiley & Sons, Inc.

and thus the welfare of 1.3 billion people in this country. Increasing water consumption as a result of rapid population growth, economic development, and strong climatic variations, mean China faces substantial water-related challenges in the coming decades, such as food security and environmental degradation (Varis and Vakkilainen 2001). Furthermore, hydrological extreme events such as floods and droughts, can lead to environmental risks and economic losses. For instance, due to the drought in northern China in winter 2008–2009, more than 4 million people and 2 million livestock had insufficient drinking water (Gao and Yang 2009). The drought in southwestern China during 2009−2010 also caused a ~20% reduction in the nationwide hydro-electrical production (Barriopedro et al. 2012). Therefore, robust precipitation projections are crucial for China's future. Piao et al. (2010) suggest that annual precipitation decreased in northeast China, and increased in northwest and southeast China over the period 1960–2006. Precipitation increases over northwest China may be caused by increases in atmospheric water vapor content and an enhanced water cycle caused by global warming (Shi et al. 2007). Over east China, which is dominated by the East Asian monsoon, a "wet south-dry north" precipitation pattern has been suggested to arise from the weakening of the East Asian summer monsoon since the end of the 1970s (Zhou et al. 2009), which is associated with a strong upper-tropospheric cooling and the phase of North Atlantic Oscillation (NAO) in the preceding winter (Xin et al. 2006; Yu and Zhou 2007; Yu et al. 2004). This multi-decadal variability of the East Asian summer monsoon can also be explained by tropical ocean warming, a weakening sensible heat source over the Tibetan Plateau, aerosol forcing, and internal variability (Zhou et al. 2009).

Simulations from global coupled ocean-atmosphere circulation models forced with projected greenhouse gas and aerosol emissions are the primary tools for estimating trends and variability of future climate (Kharin et al. 2007). The Coupled Model Intercomparison Project (CMIP) was established as a standard experimental protocol to evaluate the atmosphere-ocean general circulation models (GCMs) and to estimate future climate projections under different scenarios. Based on the output of CMIP3, Tu et al. (2009) indicate that long-term precipitation trends over eastern China were largely underestimated, and the observed spatial pattern of rainfall changes was not reproduced by most models. Miao et al. (2012) evaluated the applicability of temperature and precipitation data from CMIP3 for China, and suggest that annual precipitation and temperature generated by IPCC AR4 GCMs should be used cautiously in China due to their poor performance. The most recent phase of CMIP, CMIP5, provides simulations from the latest generation of state-of-the-art GCMs, which includes more comprehensive GCMs with generally higher spatial resolution compared with CMIP3 (Taylor et al. 2011).

A number of studies have evaluated specific aspects of CMIP5 precipitation simulations for China, such as specific regions or seasons. For instance, Huang et al. (2013) examined CMIP5 summer precipitation over eastern China and suggest that the multimodel ensemble can reproduce summer precipitation, however large uncertainties exist over south China. Qu et al. (2013) indicate that the CMIP5 historical simulations reasonably capture the climatology of East Asian summer rainfall, the associated circulation, moisture, and its transport. Also, the circulation features of the East Asian winter monsoon can be reasonably reproduced by the multimodel ensemble of CMIP5

(Gong et al. 2013). By comparing CMIP3 and CMIP5 simulations with observations in regard to the Asian monsoon, CMIP5 shows better skill in capturing the monsoon characteristics both in summer (Sperber et al. 2013) and winter (Wei et al. 2013). Some studies have described future CMIP5 simulations for the entire region of China (Wang and Chen 2013; Xu and Xu 2012), however, a comprehensive assessment relative to historical observations has not yet been performed. Similarly, a comparison of CMIP5 precipitation simulations and potential improvements relative to CMIP3 has not yet been provided.

In this study, we therefore investigate precipitation simulations over all of China as well as for individual sub-regions, based on the 20 GCMs from the CMIP5 archive with simulations for both the 20th and 21st centuries. We employ a suite of model evaluation statistics to provide a comprehensive assessment of model performance. Our study focuses on the following two research questions; first, how good is the agreement between observed precipitation and CMIP5 simulations over the 20th century? As part of this assessment we also evaluate the CMIP3 models, to quantify the potential improvements in CMIP5 over the previous intercomparison. In light of CMIP5's 20th century performance, the other research question is: what is the projected precipitation variability for China over the 21 century? Section 3.2 describes the data sets and analysis methods. Section 3.3 compares the historical precipitation variability during the 20th century from two observational datasets with precipitation simulations from 20 GCMs. Section 3.4 estimates the future precipitation trends and variability over the 21st century based on the CMIP5 model projections. Section 3.5 discusses the agreement between observations and

model simulations and puts the CMIP5 projections into context with respect to the observed biases. Section 3.6 provides the conclusions of our study.

3.2. Data and Methods

3.2.1. Data

We use four sets of simulations from 20 GCMs in the CMIP5 archive (Table 3.1): one historical experiment and three future emission scenarios. We also evaluate output from the CMIP3 archive to assess the potential improvements in CMIP5. The 20 models used here are selected because they are the only ones with output available for both the historical and all emission scenarios for the future simulations. The future scenarios are three of the representative concentration pathways (RCP) developed for the IPCC Fifth Assessment Report (AR5), specifically: RCP 8.5, RCP 4.5, and RCP 2.6. The historical experiment (1850–2005) was forced by observed atmospheric composition changes (reflecting both anthropogenic and natural sources), with some models including time-evolving land cover (Taylor et al. 2011). For a full listing of all model forcings, see Table 1 in Chen and Frauenfeld (2014b). The RCP 8.5 scenario (2006–2300) assumes high population growth and high energy demand without climate change policies. Therefore, it corresponds to the pathway with the highest greenhouse gas emissions, brought about by a radiative forcing of 8.5 W/m^2 in 2100 (Riahi et al. 2011). RCP 4.5 is a scenario that stabilizes radiative forcing at 4.5 W/m^2 in 2100 without ever exceeding that value (Thomson et al. 2011). It can be considered a medium stabilization scenario. RCP 2.6

Table 3.1. List of 20 CMIP5 GCMs used in our study and their spatial resolution.

Model	Modeling Center	Spatial Resolution
ACCESS1.3	CSIRO (Commonwealth Scientific and Industrial Research Organisation, Australia), and BOM (Bureau of Meteorology, Australia)	145×192
BCC−CSM1.1	Beijing Climate Center, China Meteorological Administration, China	64×128
CCSM4	National Center for Atmospheric Research, USA	192×288
CESM1(CAM5)	National Science Foundation, Department of Energy, National Center for Atmospheric Research	192×288
CMCC−CESM	Centro Euro-Mediterraneo per I Cambiamenti Climatici	48×96
CNRM−CM5	Centre National de Recherches Meteorologiques / Centre Europeen de Recherche et Formation Avancees en Calcul Scientifique	128×256
CSIRO−Mk3.6.0	CSIRO (Commonwealth Scientific and Industrial Research Organisation, Australia), and BOM (Bureau of Meteorology, Australia)	145×192
CanESM2	Canadian Centre for Climate Modelling and Analysis	64×128
EC−EARTH	EC-EARTH consortium	160×320
FGOALS−g2	LASG, Institute of Atmospheric Physics, Chinese Academy of Sciences; and CESS, Tsinghua University, China	60×128
GFDL−CM3	Geophysical Fluid Dynamics Laboratory, USA	90×144
GISS−E2−H	NASA Goddard Institute for Space Studies, USA	90×144
HadGEM2−CC	Met Office Hadley Centre, UK	145×192
INM−CM4	Institute for Numerical Mathematics, Russia	120×180
IPSL−CM5A−LR	Institut Pierre-Simon Laplace, France	96×96
MIROC−ESM	Japan Agency for Marine-Earth Science and Technology, Atmosphere and Ocean Research Institute (The University of Tokyo), and National Institute for Environmental Studies, Japan	128×256
MIROC5	Atmosphere and Ocean Research Institute (The University of Tokyo), National Institute for Environmental Studies, and Japan Agency for Marine-Earth Science and Technology, Japan	128×256
MPI−ESM−LR	Max Planck Institute for Meteorology, Germany	96×192
MRI−CGCM3	Meteorological Research Institute, Japan	160×320
NorESM1−M	Norwegian Climate Centre, Norway	96×144

Table 3.2. List of 22 CMIP3 models in our study and their spatial resolution.

Model Name	Modeling Center	Spatial Resolution
BCCR−BCM2.0	Bjerknes Centre for Climate Research, Norway	64×128
CGCM3.1	Canadian Centre for Climate Modeling and Analysis, Canada	48×96
CNRM−CM3	Centre National de Recherches Météorologiques, France	64×128
CSIRO−MK3.0	Commonwealth Scientific and Industrial Research Organisation, Australia	96×192
CSIRO−MK3.5		96×192
GFDL−CM2.0	US Department of Commerce/National Oceanic and Atmospheric Administration (NOAA)/Geophysical Fluid Dynamics Laboratory (GFDL), USA	90×144
GFDL−CM2.1		90×144
GISS−AOM	National Aeronautics and Space Administration(NASA)/Goddard Institute for Space Studies(GISS), USA	60×90
GISS−MODEL−EH		46×72
IAP−FGOALS1.0−G	LASG/IAP, China	60×128
INGV−ECHAM4	National Institute of Geophysics and Volcanology, Italy	160×320
INMCM3.0	Institute of Numerical Mathematics, Russia	45×72
IPSL−CM4	Institute Pierre Simon Laplace, France	72×96
MIROC3.2−HIRES	CCSR of Tokyo University, Frontier of JAMSTEC, Japan	160×320
MIROC3.2−MEDRES		64×128
MIUB−ECHO−G	Meteorological Institute of the University of Bonn, Meteorological Research Institute of the Korea Meteorological Administration (KMA), and Model and Data Group, Germany/Korea	48×96
MPI−ECHAM5	Max Planck Institute for Meteorology, Germany	96×192
MRI−CGCM2.3.2	Meteorological Research Institute, Japan	96×192
NCAR−CCSM3.0	National Center for Atmospheric Research, USA	128×256
NCAR−PCM1		64×128
UKMO−HADCM3	Hadley Center for Climate Prediction and Research/Met Office, United Kingdom, UK	73×96
UKMO−HADGEM1		145×192

corresponds to a very low forcing level, with peak radiative forcing at ~3 W/m^2 before 2100 and then declining to 2.6 W/m^2 by 2100 (Vuuren et al. 2011). Monthly precipitation output from the 20 GCMs based on the historical and three future scenarios was obtained from the CMIP5 website (http://cmip-pcmdi.llnl.gov/). Model output from the climate of the 20th century experiment (20C3M) from CMIP3 was obtained from the CMIP3 archive (http://esg.llnl.gov:8080/), and was compared with the historical CMIP5 experiment (Table 3.2).

To ensure that our assessment of model performance is not biased by our choice of observations, two different observational datasets of precipitation were used to evaluate the GCMs' performance. The Climatic Research Unit (CRU) time-series (TS) 3.10 dataset from the University of East Anglia provides high-resolution gridded (0.5° × 0.5°) monthly precipitation from 1901 to 2009. This CRU dataset is based on interpolated monthly observations from meteorological stations across global land areas (Harris et al. 2014). The Global Precipitation Climatology Centre (GPCC) version 6 dataset is available for monthly precipitation at 0.5° × 0.5° from 1901 to 2010 (Rudolf and Schneider 2005; Schneider et al. 2013). Like CRU TS 3.10 it provides gridded monthly precipitation for the global land surface, but it is based on a larger number of station observations than the CRU dataset. Previous studies have discussed the consistency between these two datasets, and found that their discrepancies are small and their time evolutions are consistent (Zhang and Zhou 2011; Zhou et al. 2008a).

3.2.2. Methods

To investigate precipitation variability during the 20th and 21st centuries, the period 1901–2005 was extracted from the historical experiment, and the period 2006–2100 was extracted from the three emission scenario experiments. The observational station distribution is rather sparse prior to approximately 1950. In evaluating the GCMs beginning in 1901, the early 1901–1950 period may potentially bias the assessment of model performance due to shortcomings in the observations. We therefore assess model performance for both 1901–2000, and also separately for the more data-rich period of 1951–2000. Because of the different spatial resolutions among the GCMs, all model output was regridded to a uniform resolution of 2.5° × 2.5° through bilinear interpolation, which is a common regridding technique (Alkama et al. 2013; Hsu et al. 2013; Huang et al. 2013; Qu et al. 2013; Wang and Chen 2013). Due to the heterogeneity in precipitation in different regions of China (Piao et al. 2010; Wang and Zhou 2005), linear trends in seasonal and annual precipitation were analyzed for five individual sub-regions following the regional divisions of Ding et al. (2008) and Feng et al. (2011) (north, south, the middle and lower reaches of the Yangtze River, northwest, and the Tibetan Plateau) and for all of China (Figure 3.1). Precipitation over the whole domain of China was calculated by averaging the grid cell values within the political boundaries (land areas) of China. Over the five sub-regions, precipitation was averaged according to the latitude and longitude boundaries. To quantify the agreement between observations and model simulations, we

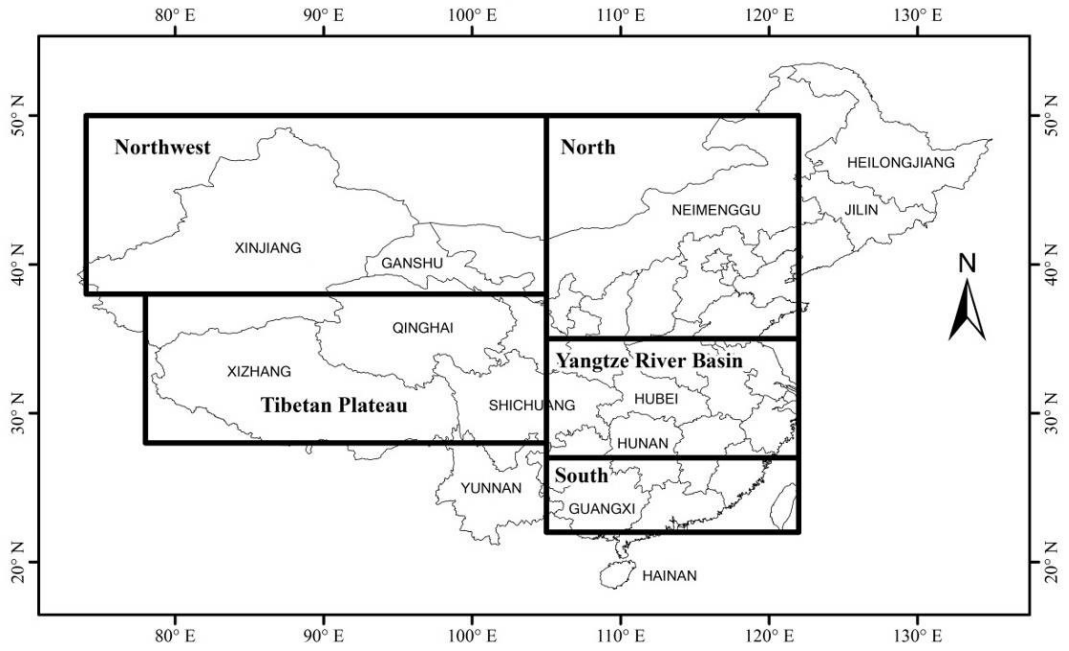

Figure 3.1. Map of China indicating the 5 regions (north, south, the middle and lower reaches of the Yangtze River, northwest, and the Tibetan Plateau) evaluated and some of major provinces' names.

calculated the differences (absolute and percentages), root mean square errors (RMSE), standard deviations of the error (SDE), and Pearson correlation coefficients (R) between the two observational datasets and the two CMIP datasets. To evaluate the GCMs' skill in reproducing the climatological precipitation distribution over China, a skill score was used as defined by (Taylor 2001):

$$S \equiv \frac{(1+R)^4}{4(SDR + 1/SDR)^2}$$

where R is the pattern correlation between the models and the observations, and SDR is the ratio of spatial standard deviation in the models against that of the observations (Hirota and Takayabu 2013). To examine the significance of improved skill in CMIP5 compared

with CMIP3, a method proposed by Song and Zhou (2014) was used. Our study domain (20°−50°N, 75°−125°E) was evenly divided into 15 subregions of 10° × 10° size. Skill scores for both CMIP3 and CMIP5 were calculated in each subregion. Based on Song and Zhou (2014)'s test method, if the CMIP5 scores are higher than CMIP3 over 80% of the subregions (here, at least 12), the improvement of the CMIP5 multimodel ensemble over CMIP3 is considered significant. Additionally, to evaluate the interannual precipitation variability in CMIP5, skills scores were calculated for interannual standard deviation (ISTD) of precipitation.

3.3. Historical Precipitation in the 20th Century

We first compare the spatial patterns of the 1901–2000 means for the calendar year, as well as the winter (December–February, DJF) and summer (June–August, JJA) seasons separately. Figure 3.2 shows the spatial distribution of the mean annual precipitation during the 20th century from CRU, GPCC, and the ensemble averages from CMIP3 and CMIP5. There is good agreement between the two observational datasets (Figure 3.2a, b). The highest precipitation occurs over southern China, likely due to the East Asian summer monsoon (Ding and Chan 2005). The lowest precipitation is observed over northwestern China, especially in Xinjiang province where the largest desert of China is found. Seasonal precipitation suggests a monsoon-induced pattern, with more precipitation in summer and less during winter. In general, both CMIP3 and CMIP5 can reproduce the spatial distribution of annual and seasonal precipitation reasonably. However, they overestimate the precipitation magnitude in many regions of China (Figure 3.2c and d). There are very

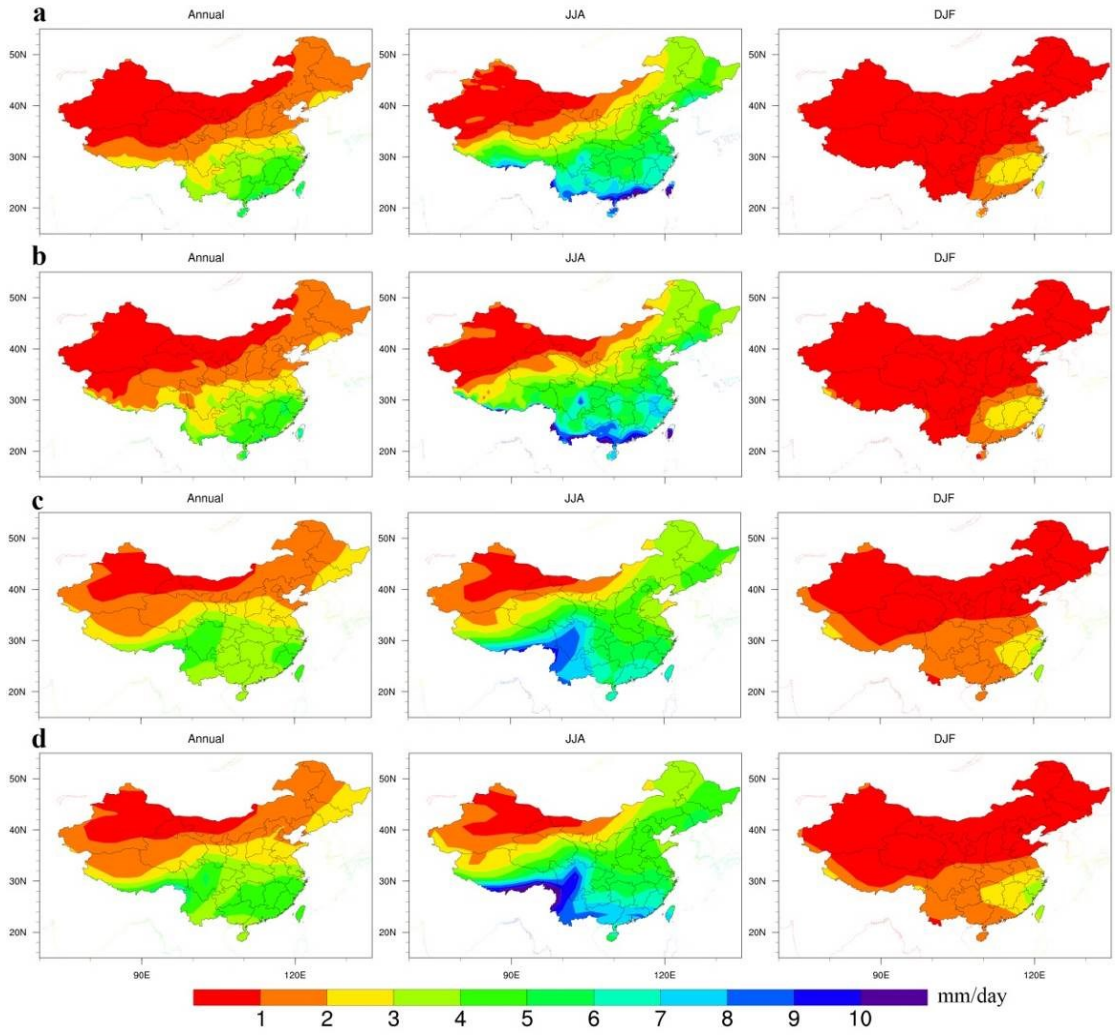

Figure 3.2. Spatial distribution of mean annual precipitation over China during the 20th century generated from a) CRU, b) GPCC, and ensemble averages from c) CMIP3, and d) CMIP5. The left column is annual precipitation; the middle column is summer (JJA) precipitation; and the right column is winter (DJF) precipitation.

large positive biases in Yunnan and Sichuan provinces, which are at the eastern edge of the Tibetan Plateau. Additionally, the models underestimate summer precipitation over southeast China.

Because the spatial pattern is extremely similar for CRU and GPCC (Figure 3.2a and b), we show only the difference with CMIP3 and CMIP5 based on GPCC (Figure 3.3). Compared with the observations, the CMIP5 models exhibit better correspondence than the CMIP3 models over 1901–2000. For CMIP3, there are much larger negative biases in eastern China during summer, and larger positive biases in the southwest during both summer and winter. The multimodel ensemble average of CMIP5 has a higher skill score (S = 0.79) compared with CMIP3 (S = 0.71), demonstrating the better performance of CMIP5 (Figure 3.4). Based on the *Song and Zhou* [2014] test method, CMIP5 skill scores are higher than CMIP3 in 13 subregions, suggesting that CMIP5 exhibits a statistically significant improvement in simulating climatological precipitation over CMIP3. There is very good agreement between the two observational products (S = 0.95). The individual models show a varying ability to capture the climatological annual precipitation distribution for China. EC-EARTH and HadGEM2-CC exhibit better skill than the other models (0.83 and 0.79, respectively), while MIROC-CAM5 and FGOALS-g2 present the lowest skills. These skill scores show little change if we focus on the 1951–2000 climatological annual precipitation distribution, rather than 1901–2000 (Figure 3.4).

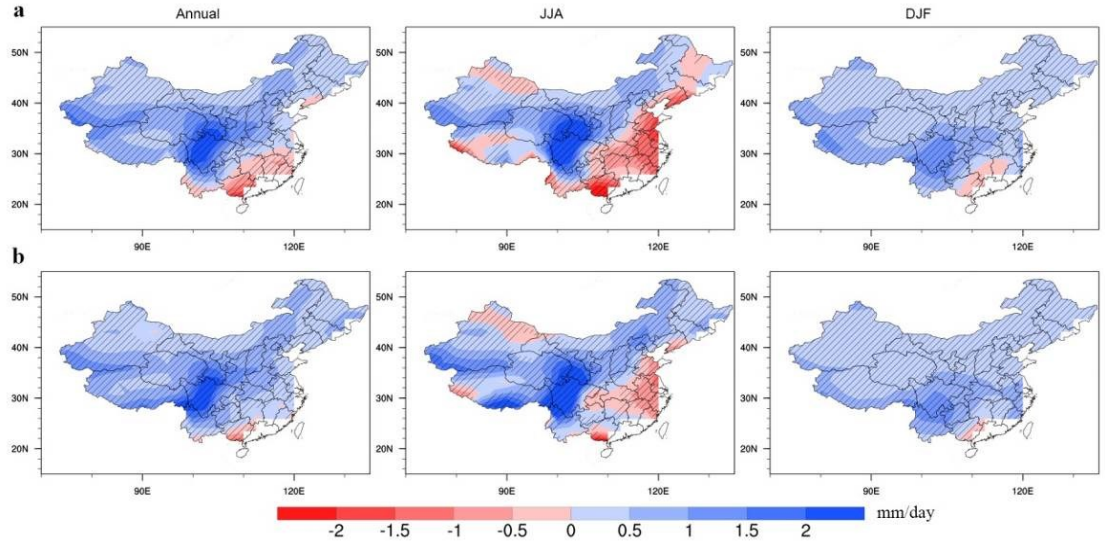

Figure 3.3. The difference in mean annual precipitation between model simulations and observations: a) CMIP3−GPCC, b) CMIP5−GPCC. The left column is annual precipitation; the middle column is summer (JJA) precipitation; and the right column is winter (DJF) precipitation. Dashed regions indicate statistically significant differences.

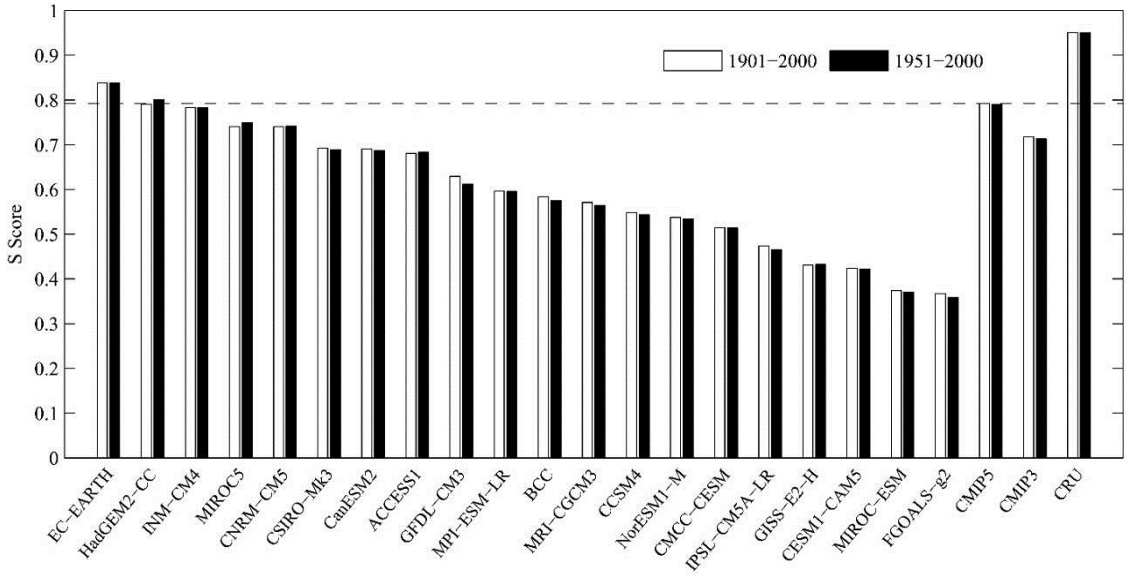

Figure 3.4. Skill scores of CMIP5, CMIP3, and CRU relative to the GPCC annual precipitation distribution over China for 1901–2000 (black) and 1951–2000 (white). The dashed line indicates the skill of the CMIP5 ensemble average (S = 0.79).

Table 3.3. Annual and seasonal precipitation means and trends for China over 1901–2000 derived from GPCC and CRU observations, and CMIP3 and CMIP5 multimodel ensemble averages; 95%-level statistically significant differences (expressed as percentage here) or trends are shown in bold.

	Annual	Spring	Summer	Fall	Winter
	Precipitation (mm/day)				
GPCC	1.94	1.56	4.29	1.57	0.46
CRU	1.88	1.52	4.17	1.49	0.43
CMIP3	2.41	2.43	4.06	2.03	1.14
CMIP5	2.49	2.42	4.40	2.06	1.08
	Percentage difference (%)				
GPCC vs. CRU	**4**	3	**3**	**6**	6
CMIP3 vs. GPCC	**24**	**55**	**-5**	**29**	**149**
CMIP5 vs. GPCC	**28**	**55**	**3**	**31**	**136**
CMIP3 vs. CRU	**29**	**60**	**-3**	**37**	**165**
CMIP5 vs. CRU	**33**	**60**	**5**	**39**	**151**
	Precipitation trend (mm/year)				
GPCC	**-0.47**	-0.48	-0.51	**-0.63**	**-0.31**
CRU	0.11	0.17	0.33	-0.06	0.00
CMIP3	**-0.08**	0.06	**-0.19**	**-0.19**	-0.01
CMIP5	**-0.26**	**-0.20**	**-0.50**	**-0.20**	**-0.15**

To further quantify the performance of CMIP3 and CMIP5, annual and seasonal mean precipitation and precipitation trends over the entire 20th century and for the period 1951–2000 are calculated (Tables 3.3 and 3.4). For the entire 20th century, the annual mean precipitation derived from GPCC and CRU, CMIP3, and CMIP5 for China are 1.94, 1.88, 2.41, and 2.49 mm/day, respectively. The two observational datasets are significantly different from each other for annual, summer, and fall precipitation. Both CMIP3 and CMIP5 models overestimate annual and seasonal precipitation over China. The annual overestimate by CMIP3 versus observations is statistically significant, and the annual CMIP5 overestimate with respect to CMIP3 is as well. CMIP3 has a smaller percentage

Table 3.4. As Table 3.3, but for the period 1951–2000.

	Annual	Spring	Summer	Fall	Winter
	Precipitation (mm/day)				
GPCC	1.91	1.53	4.25	1.53	0.43
CRU	1.88	1.53	4.18	1.48	0.43
CMIP3	2.41	2.43	4.04	2.02	1.14
CMIP5	2.47	2.41	4.36	2.04	1.07
	Percentage difference (%)				
GPCC vs. CRU	1	0	2	3	1
CMIP3 vs. GPCC	**26**	**59**	**-5**	**32**	**164**
CMIP5 vs. GPCC	**29**	**57**	**2**	**34**	**147**
CMIP3 vs. CRU	**28**	**59**	**-3**	**36**	**167**
CMIP5 vs. CRU	**31**	**57**	**4**	**38**	**150**
	Precipitation trend (mm/year)				
GPCC	-0.01	0.13	0.34	-0.63	0.19
CRU	-0.16	0.09	0.03	-0.86	0.14
CMIP3	-0.01	**0.21**	-0.15	-0.18	0.03
CMIP5	**-0.27**	**-0.24**	**-0.49**	-0.14	**-0.23**

difference in annual precipitation due to its underestimation of summer precipitation (consistent with Figure 3.3). Seasonally, CMIP3 and CMIP5 show a similar capacity to simulate precipitation in spring and fall, but CMIP5 results agree more closely with observations than CMIP3 does during summer and winter. For the 1901–2000 trends in precipitation, there is a discrepancy between GPCC and CRU observations (Table 3.3). GPCC indicates significant decreases in annual, fall, and winter precipitation of −0.47, −0.63, and −0.31 mm/year, respectively, while CRU shows no statistically significant trend in either annual or seasonal precipitation. Previous studies suggest that there is no significant linear trend in country-averaged annual precipitation over China (Ding et al. 2007; Wang et al. 2004). Therefore, the trend derived from the CRU observation is more

reasonable, while the drying trend in GPCC may arise from a precipitation bias over the Tibetan Plateau (Zhang and Zhou 2011). Both CMIP3 and CMIP5 suggest a drying trend during 1901–2000, and the trend from CMIP5 is more similar to GPCC's in both annual and seasonal precipitation. When we focus on the period 1951–2000 (Table 3.4), when there is better agreement between the two observational products, precipitation biases still show a similar pattern as for the entire 20th century. However, CMIP3 exhibits better agreement with the observations in terms of precipitation trends.

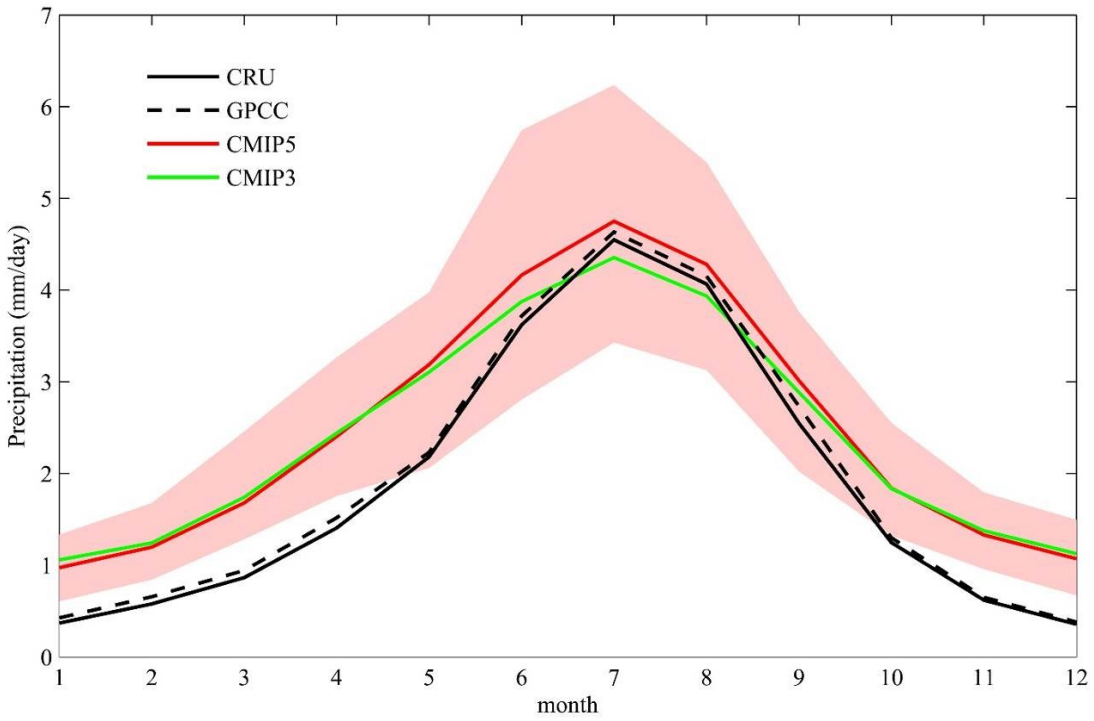

Figure 3.5. Monthly precipitation (1901–2000) based on CRU, GPCC, and the multimodel ensemble averages for CMIP3 and CMIP5. The pink shading indicates the range (maximum–minimum) of precipitation simulated by the 20 CMIP5 GCMs.

Figure 3.5 shows the 1901–2000 climatology of monthly precipitation from observations and model simulations. There is very good agreement between the two observational products, but both CMIP3 and CMIP5 overestimated precipitation throughout the year, with only a slight negative bias in CMIP3 in summer. The ranges of the maximum and minimum precipitation among individual CMIP5 models indicate that there are large uncertainties in summer precipitation simulations in CMIP5. The CMIP3 models also indicate the largest precipitation range in summer (not shown).

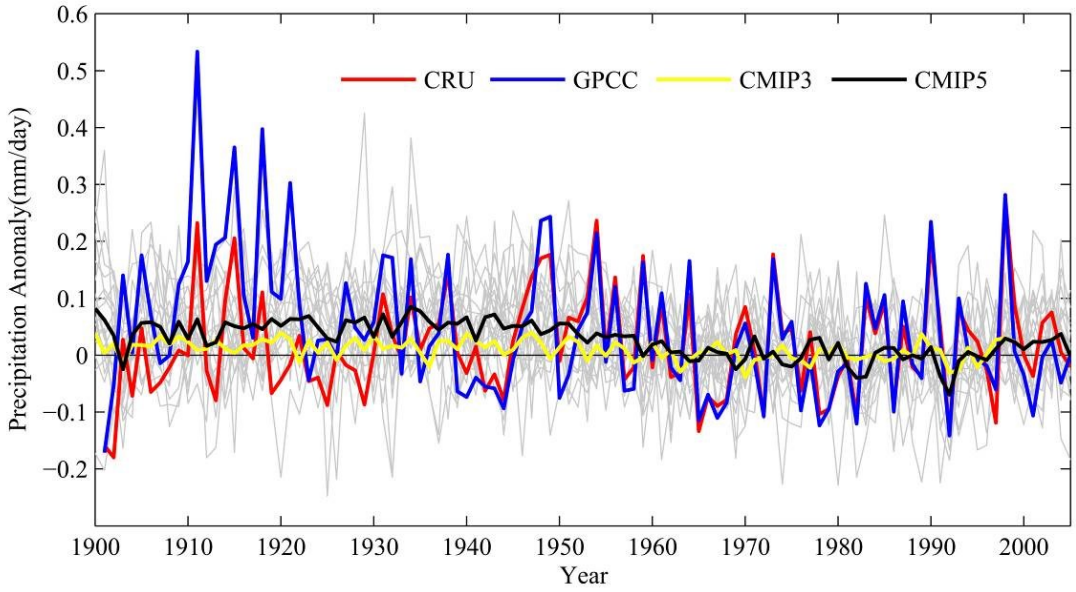

Figure 3.6. Time series of annual precipitation anomalies derived from CRU and GPCC, the ensemble average of all 20 CMIP5 GCMs, and CMIP3. Grey lines represent precipitation from the individual CMIP5 models.

Figure 3.6 shows time series of annual precipitation anomalies (relative to 1961–1990 baseline) for all of China derived from the CRU and GPCC datasets, and the

ensemble average from both CMIP3 and CMIP5. The two observational time series are significantly correlated with each other ($R = 0.75$, $p<0.01$). There are nonetheless biases between the two datasets at the beginning of the century (before 1930s) when the station data coverage is extremely sparse. After then, they exhibit much better agreement and the correlation increases to 0.95 ($p<0.01$). The consistency between the two observational products is also supported by previous studies (Zhang and Zhou 2011). However, there is a mismatch between the observations and the model simulations. CMIP5 exhibits somewhat better agreement with CRU than CMIP3, although neither multimodel ensemble is significantly correlated with CRU. The correlations between CMIP3 and CMIP5 with GPCC are very weak, and only CMIP5 is significantly correlated with GPCC over 1901–2000 ($R=0.23$, $p<0.01$), respectively. The multimodel mean shows greatly smoothed precipitation variability, as it represents an average of multiple ensembles and 20 models.

Assessing the ability of individual GCMs to simulate annual precipitation for the second half of the 20th century (Table 3.5), we find a large spread among the individual models in terms of model errors, correlations, skill scores, and long-term trends. Overestimation of annual precipitation is evident for all the models (except MRI−CGCM3). MRI−CGCM3, IPSL−CM5A−LR, CSIRO−Mk3, FGOALS−g2, and EC−EARTH have the smallest errors among the 20 models, relative to both the CRU and GPCC observations. In terms of correlations with observations, only MPI_ESM_LR correlates significantly with both observational products ($R = 0.31$ and 0.35), and ACCESS1 significantly correlated with CRU ($R = 0.33$). As suggested by Eden et al.

(2012), it is not reasonable to expect GCMs to capture the interannual variability in observations. We observe that, indeed, they cannot. However, it is interesting to note that MPI−ESM−LR does consistently (over both 1901–2000 and 1951–2000 relative to both CRU and GPCC) capture the interannual variability in observations, as gauged by correlation coefficients. We also calculated the skill scores of ISTD of precipitation to determine whether the CMIP5 models can capture the spatial pattern of interannual variability of precipitation over China. Because multimodel ensembles greatly smooth the interannual variability, both CMIP3 and CMIP5 have very low scores but CMIP5 exhibits slightly better skill than CMIP3. The models ACCESS1, HadGEM2−CC, MIROC5, EC−EARTH, and INM−CM4 show higher skill than the other models, but most have large biases compared with both observational products. Of the five models with higher skill scores, it is interesting to note that four of the models (EC−EARTH, HadGEM2, INM−CM4, and MIROC5) also exhibit better skill in simulating the climatology of precipitation over China (Figure 3.4).

Table 3.5. Evaluation of individual CMIP5 GCMs and multimodel ensemble averages of CMIP3 and CMIP5 relative to observations for annual precipitation during 1951–2000 based on root mean square errors (RMSE), Pearson's correlation coefficients, and skill scores of interannual standard deviation (ISTD). Included also are the annual mean precipitation and the trend over 1951−2000. The 95%-level statistically significant correlations and trends are shown in bold.

Model Name	Annual mean precipitation (mm/day)	RMSE (mm/day)		Correlation Coefficient		ISTD Skill Score		Trend (mm/year)
		GPCC	CRU	GPCC	CRU	GPCC	CRU	
CMIP3	2.41	3.56	3.75	0.10	0.11	0.06	0.04	-0.01
CMIP5	2.47	3.98	4.17	0.18	0.28	0.08	0.05	**-0.27**
ACCESS1	3.01	7.76	7.95	0.25	**0.33**	0.80	0.78	**-1.00**
BCC	2.51	4.32	4.51	-0.04	0.02	0.49	0.42	-0.13
CanESM2	2.26	2.57	2.75	-0.05	0.00	0.40	0.26	-0.06
CCSM4	2.52	4.38	4.57	-0.02	0.03	0.41	0.31	0.32
CESM1_CAM5	2.65	5.25	5.44	0.11	0.20	0.46	0.41	-0.31
CMCC_CESM	2.41	3.61	3.80	0.24	0.25	0.65	0.51	0.46
CNRM_CM5	2.54	4.48	4.67	-0.02	0.08	0.54	0.40	-0.36
CSIRO_Mk3	2.10	1.52	1.68	0.12	0.15	0.49	0.38	**-0.45**
EC_EARTH	2.18	2.08	2.27	0.11	0.04	0.69	0.52	0.08
FGOALS_g2	2.15	1.82	1.99	0.05	0.06	0.18	0.15	0.23
GFDL_CM3	2.32	3.02	3.20	-0.02	0.04	0.28	0.18	**-0.95**
GISS_E2_H	2.86	6.71	6.90	0.08	0.11	0.50	0.53	**-0.93**
HadGEM2_CC	2.80	6.34	6.53	0.11	0.14	0.80	0.83	**-0.80**
INM_CM4	2.71	5.73	5.92	-0.01	0.02	0.65	0.56	-0.07
IPSL_CM5A_LR	2.02	1.07	1.20	-0.06	-0.01	0.26	0.18	-0.01
MIROC5	2.89	6.91	7.10	0.00	0.10	0.78	0.69	**-1.03**
MIROC_ESM	2.50	4.20	4.38	0.02	0.09	0.29	0.20	**-0.60**
MPI_ESM_LR	2.42	3.63	3.82	**0.35**	**0.31**	0.59	0.45	**0.41**
MRI_CGCM3	1.85	0.80	0.71	0.23	0.20	0.42	0.31	**-0.40**
NorESM1_M	2.67	5.44	5.63	-0.25	-0.24	0.49	0.39	0.13

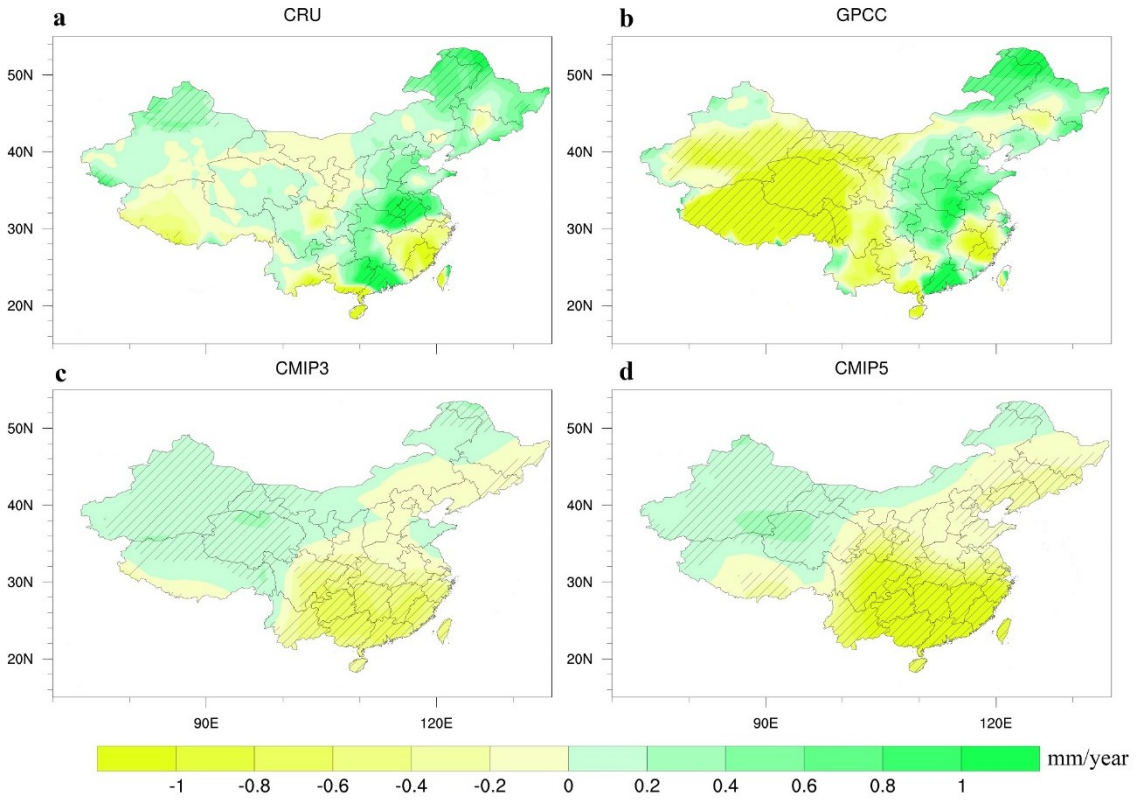

Figure 3.7. Annual precipitation trends over the 20th century; a) CRU observations, b) GPCC, c) CMIP3, and d) CMIP5; dashed regions indicate statistically significant trends (95%-level).

We next compare the annual precipitation trends over the 20th century based on the CRU and GPCC observations, and the CMIP3 and CMIP5 simulations (Figure 3.7). The CRU observations show that precipitation increased significantly over the northeast and parts of the south and northwest region, and decreased significantly over other parts of the south region, as well as the Tibetan Plateau (Figure 3.7a). The GPCC observations indicate a similar precipitation trend pattern as CRU, except for a significant decreasing trend in a large area of the northwest (Figure 3.7b). CMIP3 and CMIP5 precipitation exhibits a much simpler dipole trend pattern, consisting of significantly increasing

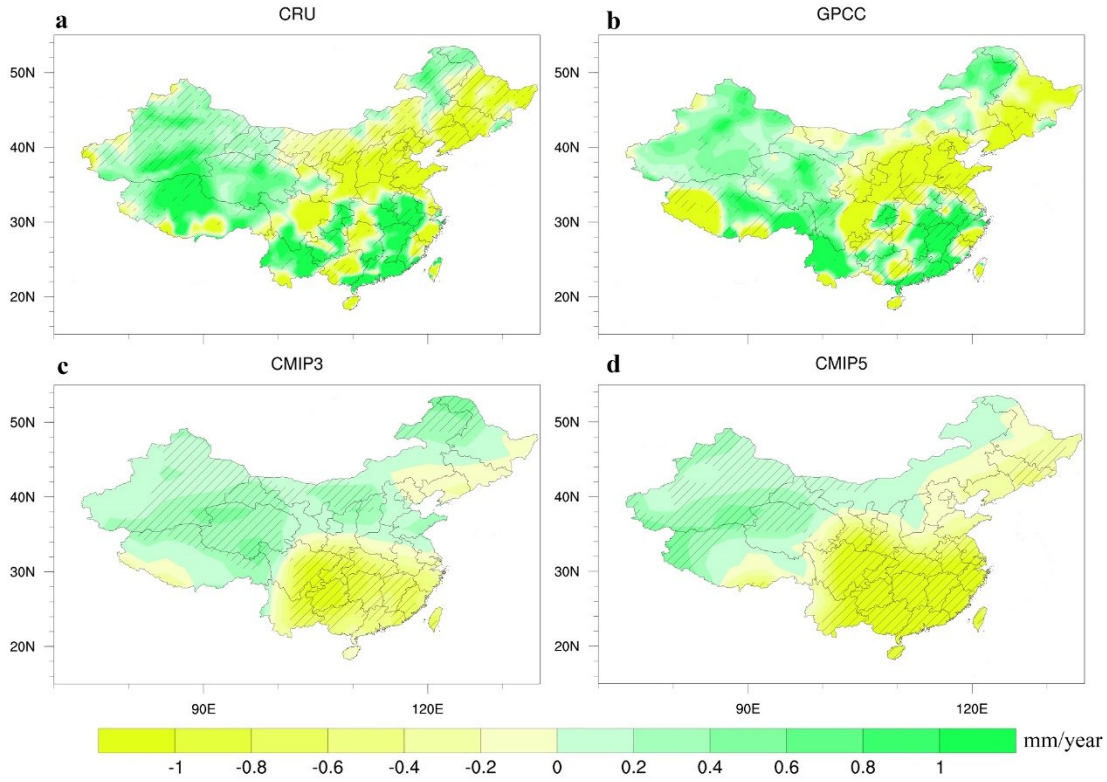

Figure 3.8. As Figure 3.7, but for the period 1951–2000.

precipitation over the northwest and parts of the northeast region, and significant drying in other regions (Figure 3.7c and d). This spatial multimodel ensemble average trend pattern does not correspond to the observed trend patterns over the 20th century.

When focusing on the more data-rich second half of the 20th century, there is much better agreement between the observational spatial patterns of precipitation trends in GPCC and CRU (Figure 3.8). There is a positive trend over the northwest, decreasing precipitation over north and central China, and increasing precipitation over large regions of the Yangtze River Basin and south China. The trends over east China reflect the decadal variations of the East Asian monsoon, also associated with a "wet south-dry north"

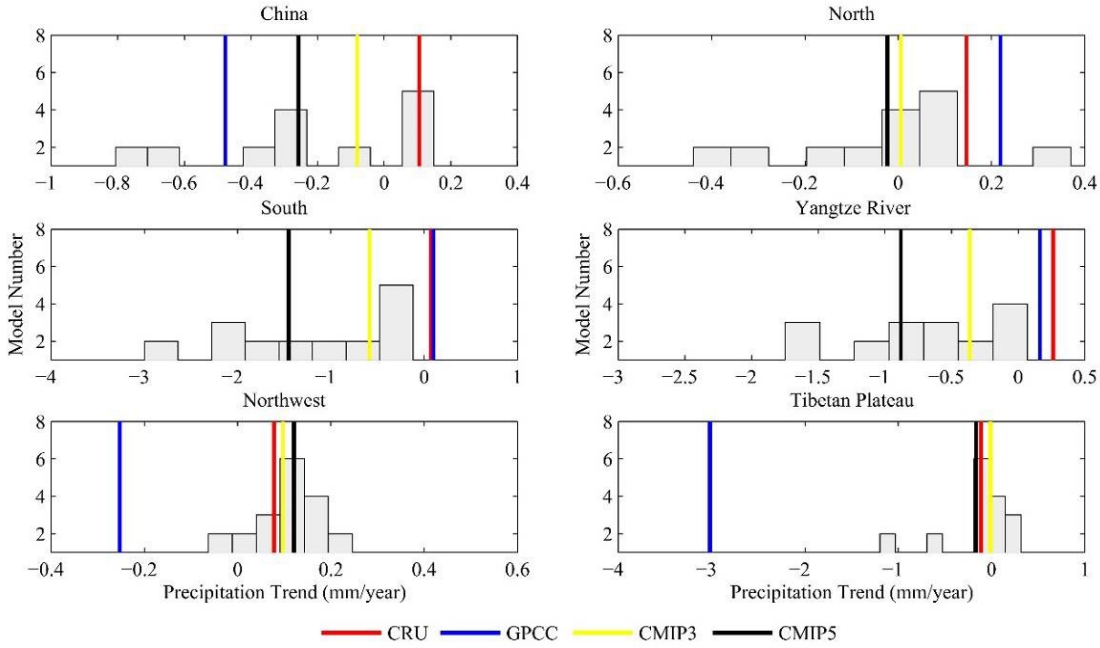

Figure 3.9. Frequency distribution of precipitation trends over the 20th century from 20 CMIP5 models (grey bars). Vertical lines indicate the precipitations trends from observations (red: CRU, blue: GPCC) and multimodel ensemble averages (yellow: CMIP3, black: CMIP5).

precipitation pattern since the end of the 1970s (Huang et al. 2012; Zhou et al. 2009). CMIP3 and CMIP5 have similar 1951–2000 trends compared to the 1901–2000 trend patterns. CMIP5's 50-year trends show improved agreement with observations over CMIP3's in the northeast, however disagreement still exist over the south.

The frequencies of 20th century precipitation trends from all 20 CMIP5 GCMs were also analyzed for the different regions of China (Figure 3.9). Overall, in terms of the sign or wetting trends over the south, the Yangtze River Basin, and the northwest. There is a decreasing trend over the south and Yangtze River Basin, and a slight increasing trend over the northwest. There is worse agreement among the 20 GCMs in precipitation trends

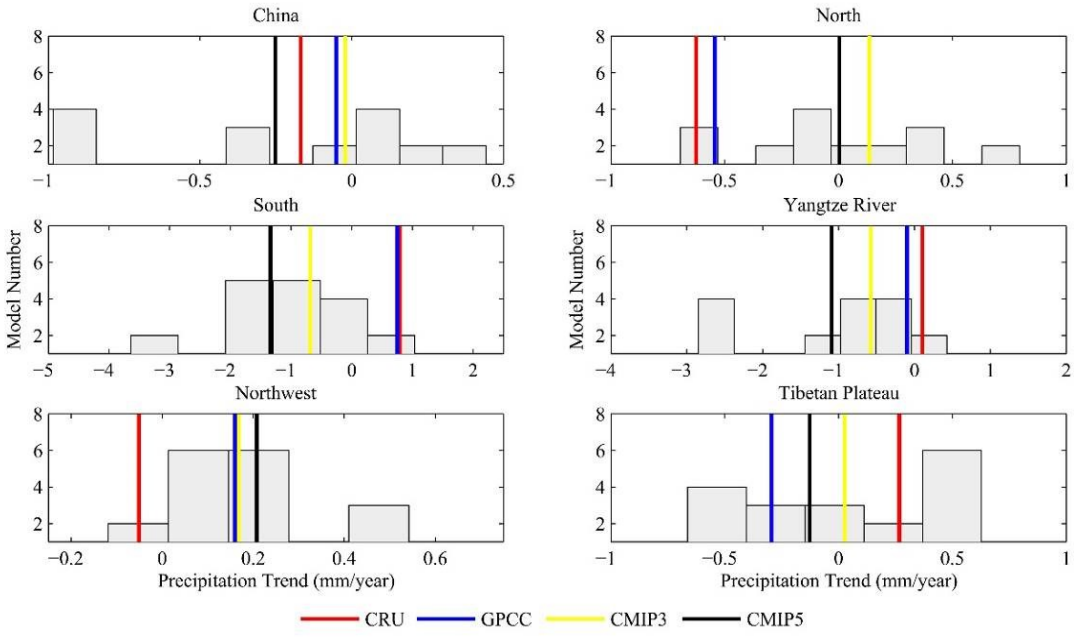

Figure 3.10. As Figure 3.9, but for the period 1951–2000.

over north China and the Tibetan Plateau where the models disagree on the sign of the trends, indicating uncertainties in simulating precipitation in this region. Multimodel ensemble means from CMIP3 show very similar precipitation trends as CMIP5, except in (positive versus negative) of the trends, the 20 GCMs reveal more consistent drying the south and the Yangtze River Basin. Compared with observational data, there is poor agreement between observed and simulated trends over the north, south, and the Yangtze River Basin, indicating poor model performance in simulating the monsoonal circulation. Both the GPCC and CRU data indicate positive trends, while CMIP5 reveals negative trends in these regions. In the northwest and the Tibetan Plateau, the CRU data show similar precipitation trends as CMIP5 and CMIP3. The precipitation trends from GPCC are substantially different, illustrating shortcomings in the observations over 1901–2000,

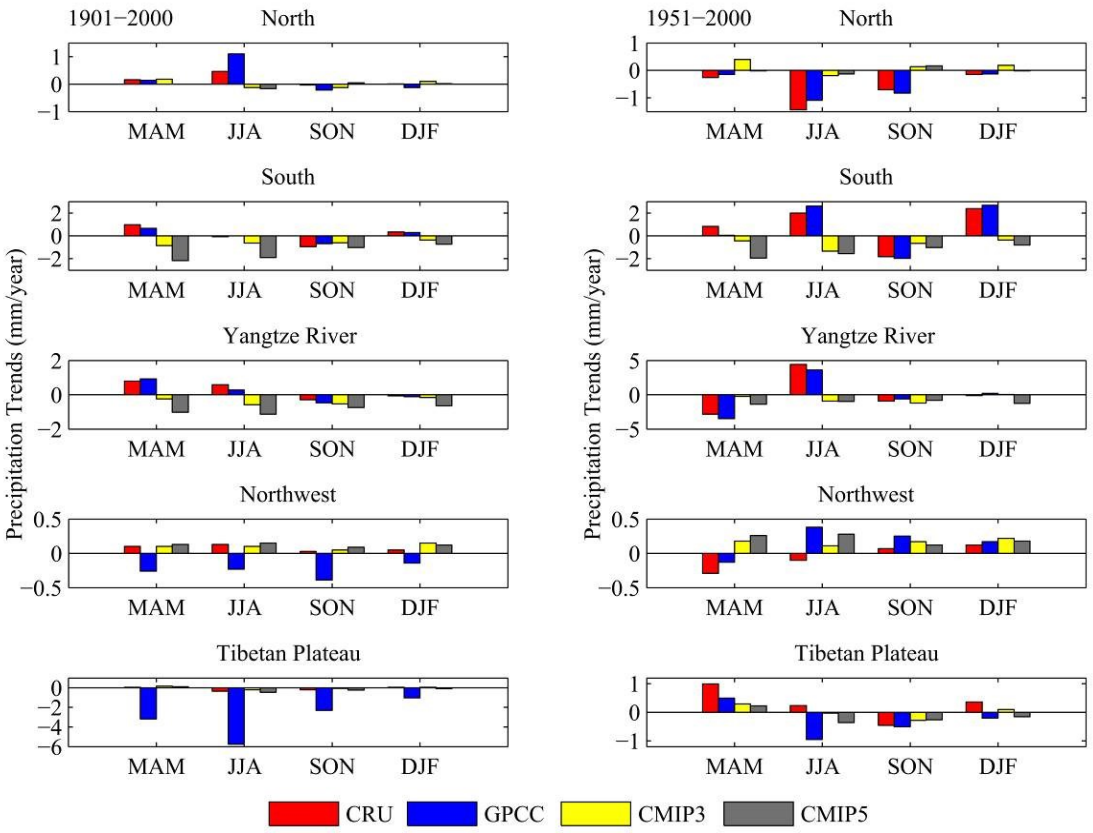

Figure 3.11. Seasonal precipitation trends in five sub-regions over the entire 20th century (left) and the second half of the century (1951–2000, right). Note the different y-axis scale between the panels.

likely driven by the data-sparse pre-1950 period. The frequency distribution of the precipitation trends over 1951−2000 from all 20 CMIP5 GCMs displays a similar pattern as over the whole century (Figure 3.10). Also, CRU and GPCC show much better agreement over the northwest and the Tibetan Plateau in the second half of the 20th century. Figure 3.11 illustrates seasonal precipitation trends in the five sub-regions of China for the periods 1901−2000 (Figure 3.11, left) and 1951−2000 (Figure 3.11, right).

In the north, the two observational products indicate positive trends in summer precipitation over the 20th century, however, this was not captured by either CMIP3 or CMIP5. For 1951−2000, drying trends were observed throughout the four seasons, with CMIP5 also exhibiting negative trends except in fall. In the south and the Yangtze River basin, there are positive trends in spring for the period 1901−2000, and positive trends in summer for the period 1951−2000. However, both CMIP3 and CMIP5 were unable to reproduce these precipitation trends. GPCC and CRU show large discrepancies over the northwest and the Tibetan Plateau in the century-scale precipitation trends due to the data scarcity before 1950. Models show similar seasonal trends as CRU observation. Over the 20th century, there are wetting trends in the northwest throughout the year, and drying in summer and fall over the Tibetan Plateau.

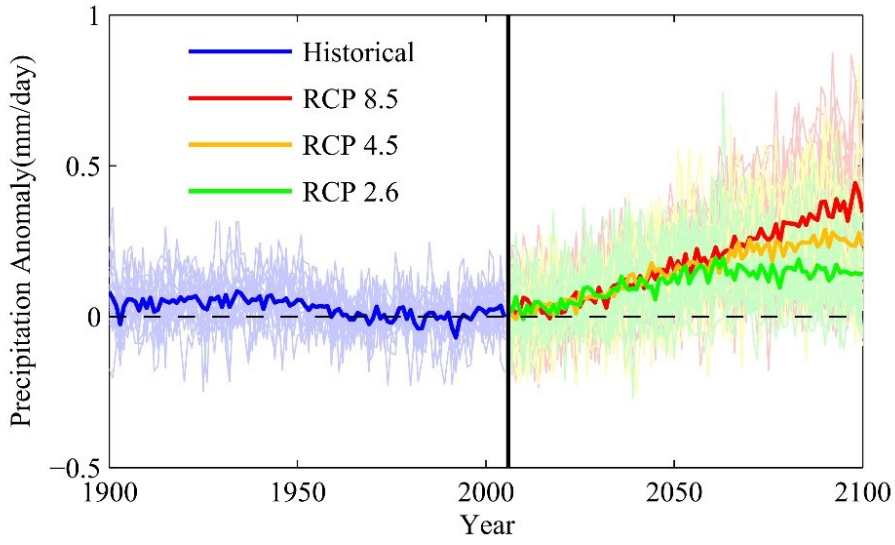

Figure 3.12. Time series of simulated precipitation in China of CMIP5 ensemble averages from different experiments during 1900–2010.

3.4. Precipitation Projections for the 21st Century

Simulated annual precipitation averaged for China from 1900 to 2100 is shown in Figure 3.12. All the emission scenario experiments exhibit significantly increasing precipitation over China during the 21st century. The RCP 8.5 scenario exhibits the largest increasing trend, at a rate of 1.5 mm/year. By the end of the 21st century, annual precipitation is projected to increase by 16% for the whole region of China. The RCP 4.5 and RCP 2.6 scenarios show a relatively smaller increasing trend, at a rate of 1.1 mm/year and 0.5 mm/year, accounting for a 12% and 6% increase by 2100, respectively.

Spatially, precipitation will increase throughout China in the 21st century (Figure 3.13). The three emission scenarios reveal the same spatial pattern of future precipitation changes, but the RCP 8.5 scenario shows the greatest increase compared to the other two. Under this scenario of highest greenhouse gas emissions (Figure 3.13a), there is a relatively high increasing trend over the Tibetan Plateau (about 3 mm/year) and relatively low increases over the northwest (about 0.6 mm/year). Comparing the two periods of 2070–2099 versus 1961–1990 reveals the same spatial pattern of changes in annual precipitation (Figure 3.13b). Under the RCP 2.6 scenario, the annual precipitation difference between the two periods does not show any significant differences between 2070–2099 versus 1961–1990 (Figure 3.13f). This projected precipitation pattern shows poor agreement with previous studies. Feng et al. (2011) suggest that annual mean precipitation will increase over southeastern China, north China, and northeast China, but will decrease over the southern Tibetan Plateau under the A1B scenario. However, Gao et al. (2008) suggest that there will be a prevailing increase in precipitation over China with

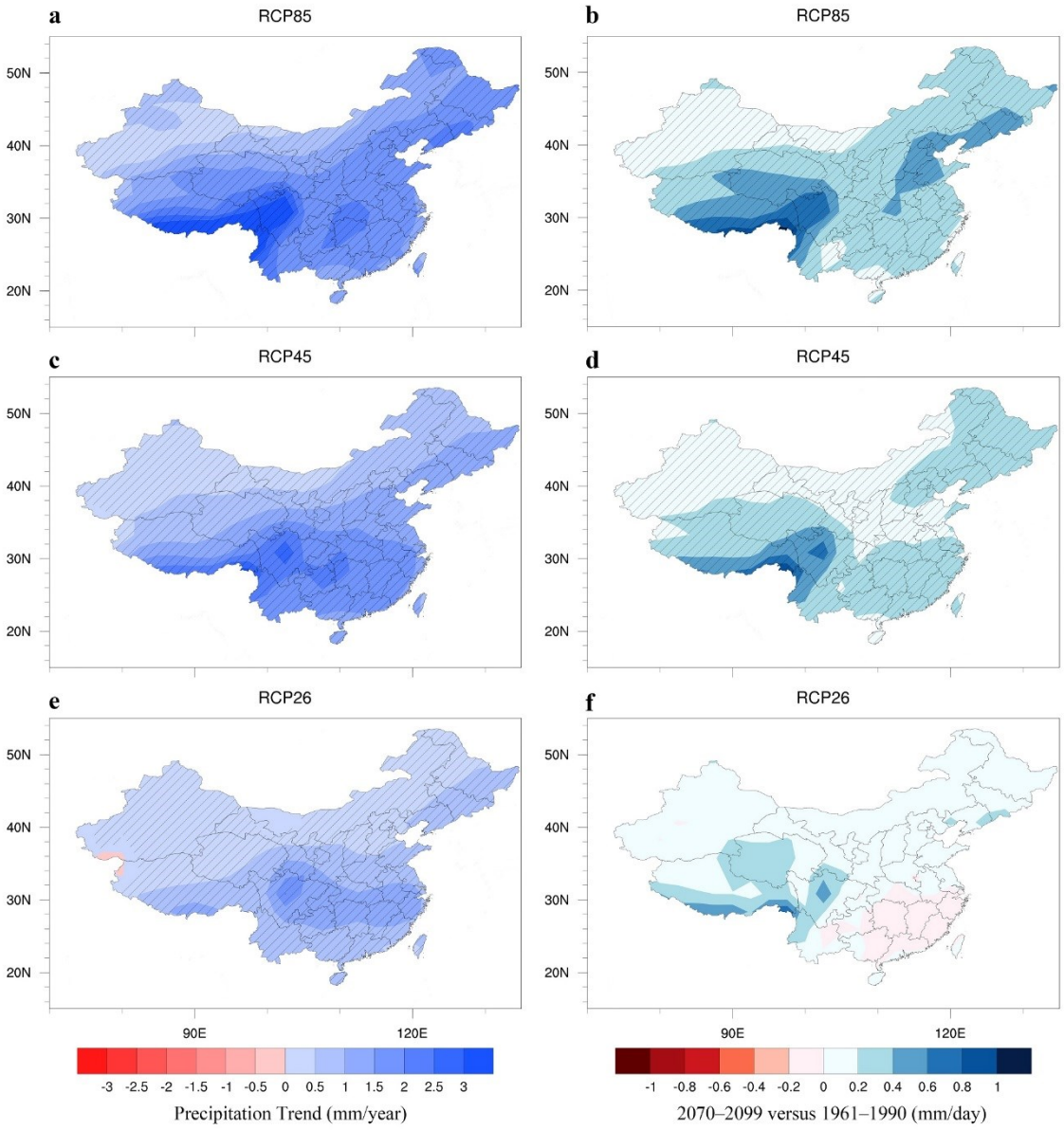

Figure 3.13. Annual precipitation trends in the 21st century for three emission scenarios (a: RCP 8.5, c: RCP 4.5, e: RCP 2.6) and changes in annual precipitation (2070–2099 versus 1961–1990) based on CMIP5 projections (b: RCP 8.5, d: RCP 4.5, f: RCP 2.6). Dashed regions indicate statistically significant trends/differences.

largest increases over the northwest and the Tibetan Plateau. However, these predictions were based on only one individual model projection. The CMIP3 multi-model ensemble indicates that there will be a significant increase in precipitation in south and northeast China, but a decrease in the Xinjiang Province in northwest China (Chen and Sun 2009). Therefore, there are large uncertainties in future precipitation projections.

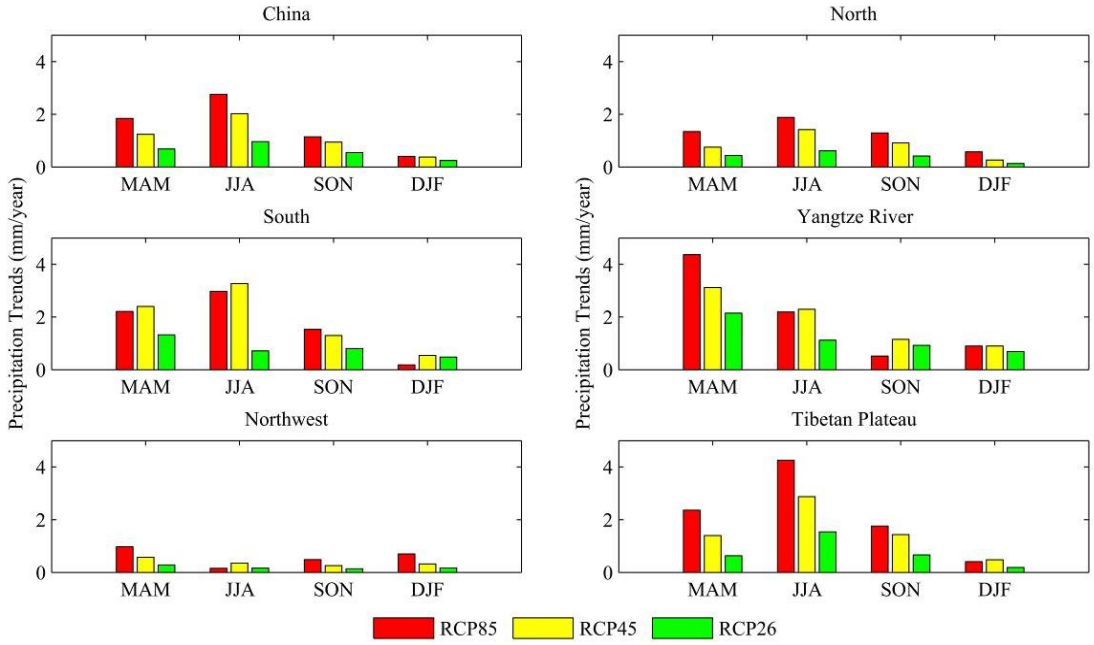

Figure 3.14. Seasonal precipitation trends over different regions of China for the 21st century based on 3 CMIP5 scenario projections.

Precipitation projections for the RCP 8.5 and RCP 4.5 scenarios exhibit similar seasonal patterns in the different regions of China over the 21st century (Figure 3.14). For China as a whole, the largest increase in precipitation will occur in JJA. There will be a similar pattern in the north, south, and the Tibetan Plateau. However, the greatest

precipitation increase will be in spring in the middle and lower reaches of Yangtze River Basin. In the northwest, the wetting trend is much smaller than in the other regions, with relatively large increases in winter and spring. Compared with the other two scenarios, the RCP 2.6 shows less seasonal variation in precipitation changes.

3.5. Discussion

In this study, the output of 20 GCMs from CMIP5 was used to assess the precipitation variability over China. The CMIP5 models show somewhat better agreement with observations than CMIP3. For instance, there are smaller biases in seasonal precipitation in CMIP5 than based on CMIP3. CMIP5 also has stronger correlations with the two observational datasets. However, significant uncertainties remain. There is a large positive bias at the eastern edge of the Tibetan Plateau, especially in summer. It is difficult to discern any improvement in CMIP5 in relative to CMIP3 over this region. These biases are likely due to the climate models' coarse resolution (Tables 3.1 and 3.2), which makes it difficult to properly reproduce the atmospheric processes in a highly spatially-heterogeneous and complex terrain (Chen et al. 2010; Su et al. 2012; Yu et al. 2000; Zhou and Li 2002). Over eastern China, both CMIP3 and CMIP5 systematically underestimate summer precipitation, even though CMIP5 shows reduced biases over CMIP3. This underestimation has also been observed in related studies (Huang et al. 2013; Sperber et al. 2013), which hypothesized that the convective and microphysical parameterization schemes and coarse resolutions of GCMs represent likely error sources in precipitation simulations. Because eastern China is dominant by the East Asian monsoon (Chang 2004;

Huang et al. 2012), previous studies have suggested GCMs' deficiencies in simulating the East Asian monsoon. The negative biases in eastern China during summer indicate that precipitation in the Meiyu front is underestimated (Song and Zhou 2014; Sperber et al. 2013). Also, the disagreement in winter precipitation may arise from the poor ENSO-winter monsoon relationship in CMIP5 models (Gong et al. 2013) since ENSO is one of main factors that influence the winter and autumn precipitation in China (Gu et al. 2012; Wang and Feng 2011).

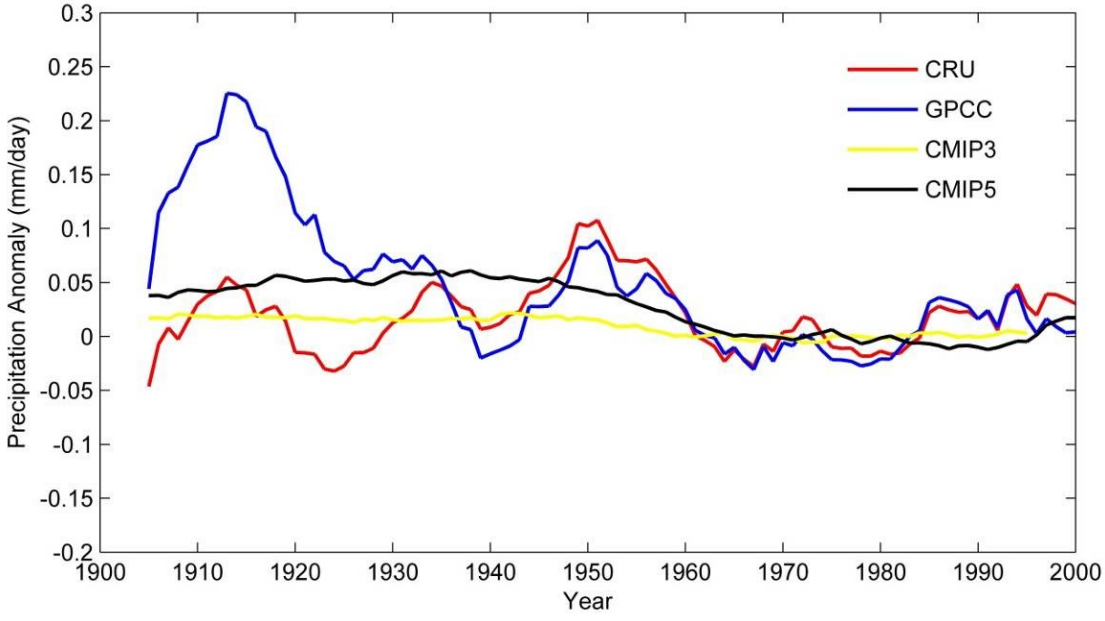

Figure 3.15. Time series of 10-year moving average precipitation from both observations and the multimodel ensemble average from CMIP3 and CMIP5.

Temporally, there is low agreement between observations and GCM simulations. Biasutti (2013) observed similar discrepancies for Sahel rainfall trends in CMIP5 output,

and suggested that the mismatch could be due to the decadal variability of sea-surface temperatures, which was not captured by the multimodel ensemble, and the underestimation of aerosol effects in climate models. Over east China, the monsoon precipitation is mainly influenced by interdecadal variability over the central–eastern Pacific and the western tropical Indian Ocean (Li et al. 2010; Zhou et al. 2008b), with aerosol forcing playing a complementary role (Song et al. 2014). However, forcing from modes of internal interdecadal variability such as the Pacific Decadal Oscillation cannot be reproduced in CMIP5 (Song et al. 2014; Zhou et al. 2013). Figure 3.15 shows the 10-year moving average of 20th century precipitation from both observations and the multimodel means. Observations exhibit decadal variability of precipitation, which is not well-captured by the multimodel means.

For the individual model evaluations, there are large uncertainties among different models, as discussed in previous studies (Huang et al. 2013; Wang and Chen 2013). The substantial differences in precipitation among CMIP5 models are likely due to differences in the forcings, the magnitude of the internal variability, and the climate sensitivity of individual models. Our results indicate that some models exhibit much better agreement with the two observational products in terms of skill scores of the climatology and ISTD of precipitation. However, it seems there is no relationship evident between model performance and their horizontal resolution. For instance, among the four models with the highest skill for both the climatology and ISTD of precipitation (EC−EARTH, HadGEM2−CC, INM−CM4 and MIROC5), EC−EARTH has a relatively high horizontal resolution (ranking 3rd of all twenty models), while the other three models have medium

horizontal resolutions. The NCAR models (CCSM4 and CESM−CAM5) with very high spatial resolution, however, do not exhibit high skill in our analysis. Therefore, spatial resolution may not be a decisive factor influencing the ability of CMIP5 to reasonably reproduce precipitation variability (Song and Zhou 2014).

The spatial pattern of CMIP5 trends over the 20th century does not correspond to observational trends. However, there is also significant disagreement in precipitation trends between the two observational datasets. The main reason for this discrepancy could be the input data source (rain gauge data) used in the different global precipitation datasets, as also observed by Harris et al. (2014) for CRU and GPCC. For instance, large differences in observed precipitation are evident at the beginning of the 20th century because of the scarcity of weather stations. Also, Schneider et al. (2013) describes the differences in input data, and that the GPCC dataset integrates more data sources than just CRU, such as the Global Historical Climate Network (GHCN), and data from the Food and Agriculture Organization (FAO). Another possible reason is the interpolation method used in the different data products. Therefore, caution is necessary when using observational datasets at long (century) time scales. To account for and reduce such biases, two observational datasets were employed in our study, although changing amounts and quality of data are of course inherent in both, as they draw from similar underlying station databases. Furthermore, our results suggest that GPCC data might be biased over the Tibetan Plateau and northwest China before 1950. This shortcoming has also been noted in previous studies (Zhang and Zhou 2011). The GPCC data exhibit artificial drying trends over northwest China and the Tibetan Plateau over 1901–2000, which is not evident in other

observational datasets (Figure 3.7 and 9, and Figure 3.3 in Zhang and Zhou (2011)). However, this shortcoming in GPCC and the discrepancy with CRU has been largely eliminated after 1950 (Table 3.4 and Figure 3.8).

Based on projections from the 20 CMIP5 GCMs, there will be an increase in precipitation throughout China in the 21st century. Higher greenhouse emission scenarios correspond to larger increases in precipitation. Under continuing positive temperature trends (Xu and Xu 2012), the increased atmospheric moisture content associated with warming is hypothesized to lead to increased precipitation (IPCC 2007). Spatially, the greatest increase will occur over the Tibetan Plateau and the eastern part of China during summer. Also, the greater precipitation increase in summer implies a change in the East Asian summer monsoon in the future. Kripalani et al. (2007) suggest that the projected increases in the East Asian summer monsoon precipitation may be attributed to the projected intensification of the subtropical high. However, the increase in atmospheric water vapor as the result of a higher sea-surface temperature over the western Pacific may play a more critical role in the enhanced precipitation than the change in monsoonal low-level circulation does (Seo and Ok 2012). The large positive precipitation trend over the south and east of China may correspond to increases in extreme precipitation events and flood risks in these regions as discussed in previous studies (Kitoh et al. 2013; Li et al. 2011), indicating a potential sensivity of the East Asian monsoon to global warming. Future precipitation increases over the Tibetan Plateau will also influence the water resource availability in other regions, as the Tibetan Plateau is the source region for major rivers of China and also plays a critical role in the East Asian summer monsoon (Zhang et

al. 2004). Even though the projected precipitation increase over northwest China is relatively small, this trend may produce significant social and environmental impacts in this arid and semi-arid region (Shi et al. 2007). Following the weakening of the East Asian summer monsoon since the late 1970s, there has been increasing drought in north China with emerging water shortages (Zhou et al. 2009). If projected precipitation increases in the 21st century hold true, this may relieve water stress and may benefit agricultural development and environmental restoration in these regions.

Finally, since there are still substantial uncertainties in the simulation of regional precipitation trends in the current CMIP5 GCMs as discussed above and in previous studies (Kumar et al. 2013a), future precipitation projections should be interpreted with caution. Based on our model performance evaluation in the 20th century, there is reasonable agreement in annual precipitation trends between observations and model simulations over the northwest and the Tibetan Plateau, particularly for the more recent 1951–2000 period (Figure 3.8). This suggests that future projections for these regions may also be reasonable. However, for the Yangtze River Basin and southern China, large biases and discrepancies between the observations and models (Figure 3.7, 8, 13) call the robustness of the CMIP5 projections into question. The future precipitation trends and their magnitude in these regions (Figure 3.13) are highly uncertain. This paper illustrates the possible precipitation changes in the 21st century based on multimodel ensemble averages from 20 GCMs. Further work is needed (such as using regional climate models with higher spatial resolution) to reduce biases and to provide more robust climate projections.

3.6. Conclusions

This paper investigates the historical precipitation trends over the 20th century by using both observational datasets and model simulations, and estimates future changes. CMIP5 models well reproduced the spatial pattern of annual and seasonal precipitation over China during the 20th century, which represents an improvement over CMIP3. However, uncertainties in climate models are still evident. CMIP5 models overestimate the magnitude of precipitation in most regions of China, especially along the eastern edge of the Tibetan Plateau, and underestimate summer precipitation over the southeast of China. For China as a whole, CMIP5 overestimates annual precipitation, even more so than CMIP3. This is mainly due to the greater underestimation of summer precipitation in CMIP3. There is large spread among individual models, with the greatest uncertainties in simulating summer precipitation. Multimodel ensembles cannot capture the amplitude of the decadal variability in observed precipitation.

Throughout the 20th century, both the observations and models show an increasing trend in precipitation over parts of the northwest region, and a decreasing trend over the Tibetan Plateau. However, there is poor agreement over the southeast and northeast regions, which calls future projections into question for these parts of China. In the 21st century, there is a generally increasing trend in precipitation over all of China under all the three emission scenarios. RCP 8.5 corresponds to the largest increases in precipitation over the 21st century. By the end of the 21st century, annual precipitation will significantly increase by 6–16% based on the lowest–highest emission scenarios, respectively. The

greatest increase will occur over the Tibetan Plateau and the eastern part of China during summer, suggesting future changes in the East Asian Monsoon.

4. CLIMATIC IMPACTS OF HISTORICAL LAND COVER CHANGES IN CHINA

4.1. Introduction

Land cover and land use changes play an important role in the climate system (Comarazamy et al. 2013; Feddema et al. 2005b; Kalnay and Cai 2003). Land cover changes can influence local and regional climate by modifying the surface energy, water, and momentum fluxes, as well as greenhouse gases (Foley et al. 2005; Mahmood et al. 2014). Also, large-scale land cover changes may affect global climate through adjustments in atmospheric general circulation (Chase et al. 2000). Biogeophysical impacts have been considered as one of most important effects of land cover changes on climate by altering surface albedo, the partitioning of surface radiation fluxes, and surface roughness, thus regulating moisture and heat transport between the land surface and the atmosphere (Anderson-Teixeira et al. 2012; Mahmood et al. 2014; Notaro et al. 2011). For instance, mid-latitude land cover changes from forests to croplands can increase surface albedo and lead to cooling (Betts et al. 2007; Feddema et al. 2005a). The Intergovernmental Panel on Climate Change (IPCC) 5th assessment report (AR5) indicated there is a "very likely" radiative cooling of −0.15 (−0.25 to −0.05) W/m^2 from surface albedo changes due to human-induced land cover change since 1750 (IPCC 2013). On the other hand, deforestation in tropical regions can increase surface temperature through reduced evapotranspiration and increased sensible heat flux (Claussen et al. 2001; Davin and de Noblet-Ducoudré 2010; Pongratz et al. 2006). Lawrence and Chase (2010) suggested that the current global warming has been predominantly driven by this evapotranspiration

effect, with the albedo forcing playing a secondary role. Impacts on precipitation are not as straightforward as those on temperature, because they depend on many more complex factors, such as geographic location, regional atmospheric characteristics, area extent of land cover change, and teleconnections (Pielke et al. 2007).

With rapid population growth and economic development, China has experienced significant land cover changes, such as urbanization (Hua et al. 2008; Zhou et al. 2004), agricultural expansion (Zhang 2000), and even desertification (Wang et al. 2006b; Xue 1996). Over recent centuries, large areas of forest have been converted to farmland. For example, (Liu and Tian 2010) found that during the last 300 years the land cover changes in China were characterized by a forest area decrease of 22%, and cropland increases of 42%, and growing urban areas. Since the 1950s, additional rapid urban area growth has occurred in China, with the most intense urbanization in East China. Therefore, studies on the climatic impacts of land cover changes are crucial for our understanding of climate change over China. Climate models coupled with land surface models are commonly used to investigate these land-atmosphere interactions (Cho et al. 2014; Fu 2003; Gao et al. 2003; Hu et al. 2014; Suh and Lee 2004; Takata et al. 2009; Wang et al. 2014; Xu et al. 2015; Yu et al. 2014; Zhao and Pitman 2005; Zheng et al. 2002). Fu (2003) suggested that human-induced land cover changes, including agricultural conversion and desertification, can weaken the East Asian summer monsoon and enhance the winter monsoon, thus resulting in significant reductions of precipitation, runoff, and soil water content. Similarly, Suh and Lee (2004) found that land cover changes can lead to a warm and dry summer. Using the same climate model, however, Gao et al. (2003) indicated that historical

vegetation changes did not lead to significant changes in precipitation over East China. This discrepancy implies that there are still uncertainties in understanding the impacts of land cover changes on climate over China. In addition to the impacts of natural vegetation changes, increasing attention focuses on the influence of urbanization on climate in China (Hua et al. 2008; Li et al. 2013a; Zhou et al. 2004). Besides the warming effect on local and regional climate, it was found that urbanization is able to influence the East Asian monsoon at to a certain extent (Chen and Zhang 2013; Feng et al. 2013; Feng et al. 2014).

Despite vegetation changes and urbanization occurring simultaneously over the historical period, these two types of land cover change have previously rarely been considered in combination. Also, few studies have examined the relative magnitude of urbanization versus vegetation changes on climate over China. For instance, while Xu et al. (2015) did examine the impacts of historical land cover changes including urbanization, assessing the relative contribution of these two land cover changes was not their focus. In this study, a state-of-the-art general circulation model (GCM) is used to investigate the biogeophysical effects of vegetation changes, urbanization, and their combined effects on the climate of China. The unique contribution of this paper is therefore that it elucidates the relative importance and magnitude of urbanization versus changes in vegetation. We thus provide a comprehensive assessment of climatic impacts of human-induced land cover changes, which improves our understanding of the drivers of climate change in China. In section 4.2 we provide the model description and experimental design. Section 4.3 presents results about changes in land surface characteristics and their influences on

temperature, precipitation, and the East Asian monsoon. Section 4.4 includes discussion and conclusions.

4.2. Model Description and Experimental Design

4.2.1. Model Description

We use the Community Earth System Model (CESM) version 1.0.4[1], developed by the National Center for Atmospheric Research. This model and its predecessor versions have been widely used for studies of land-atmosphere interactions, including land cover change (de Noblet-Ducoudré et al. 2012; Kumar et al. 2014; Lawrence and Chase 2010; Lawrence et al. 2012; Lee et al. 2011; Notaro et al. 2011) and soil moisture feedbacks (Kim and Wang 2007; Meng and Quiring 2010; Wang et al. 2007; Xu et al. 2015). Also, its ability to simulate climate specifically over China has been extensively evaluated (Chen and Frauenfeld 2014b; Islam et al. 2013) and has been successfully applied to many climate studies in China (Chen and Zhang 2013; Li et al. 2014).

To isolate the effects of land surface changes, we used prescribed climatological sea surface temperature (SST) and sea ice cover between 1982 and 2001. Therefore, our model configuration only incorporates the Community Atmosphere Model version 4 (CAM4; (Neale et al. 2010) and the Community Land Model version 4 (CLM4; (Lawrence et al. 2011). CLM allows sub-grid heterogeneity by prescribing the land surface as one of five

[1] It should be noted that CCSM4 is a subset of CESM1. Based on model evaluation in previous chapters, CCSM4 shows a better agreement with observation, especially in temperature, compared with other CMIP5 models. In this study, therefore, we did all CCSM4 experiments from the CESM1 code base.

sub-grid land cover types: glacier, lake, wetland, urban, and vegetated. The vegetated portion also specifies a fractional allocation of plant functional types (PFTs). Additionally, an urban canyon model has been incorporated into CLM4, so that climate change in urban areas and the urban heat island effect can be considered (Lawrence et al. 2011; Oleson et al. 2008). In this study, the 1.9° latitude × 2.5° longitude finite volume grid was used, with a total of 26 levels in the vertical.

To assess model performance, we compare simulated surface air temperature and precipitation from our control run (see section 2.2) with observations. We use the Climatic Research Unit (CRU) time-series (TS) 3.10 dataset (Harris et al. 2014) based on our comprehensive evaluation of this product for China (Chen and Frauenfeld 2014a, 2014b). Observations were regridded to the model resolution using bilinear interpolation. Similar to Xu et al. (2015), NCEP/NCAR reanalysis 850 hPa geopotential height and winds were also used to represent observed atmospheric circulation features for assessing the model's ability to represent the East Asian monsoon. Because the control run was forced with the 1982–2001 climatology of monthly SST, the climatology of surface air temperature, precipitation, and 850 hPa circulation during this same period was calculated.

4.2.2. Experimental Design

Three experiments with different land cover conditions were conducted to evaluate the impacts of historical land cover changes on climate in China:

1) A control run forced with current (*CUR*) land cover conditions was performed, in which the PFT distribution was derived from Moderate Resolution Imaging

Spectroradiometer (MODIS) land surface data products (Lawrence et al. 2011; Lawrence and Chase 2010).

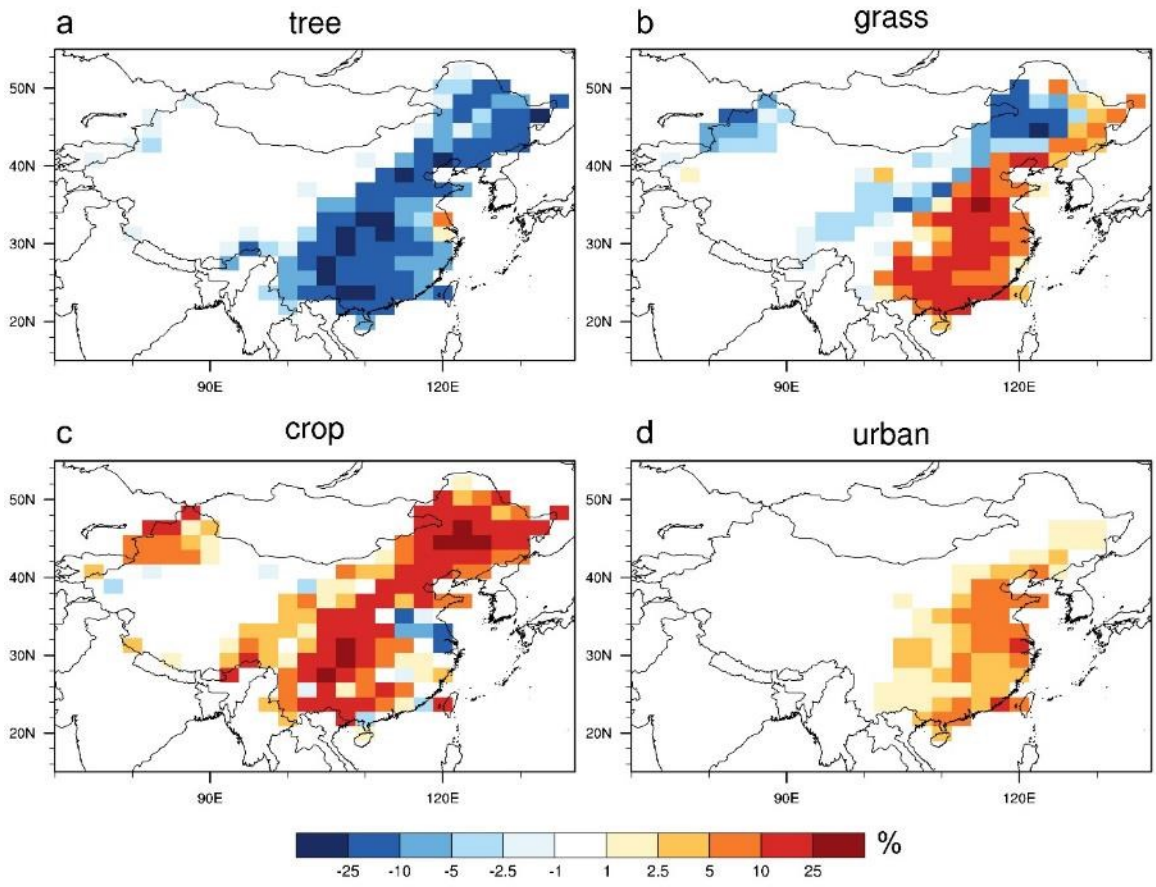

Figure 4.1. Fractional changes (percent of the grid cell) between current day and potential vegetation biomes: a. trees (including needleleaf evergreen temperate tree, needleleaf evergreen boreal tree, broadleaf deciduous temperate tree, broadleaf deciduous boreal tree); b. grass (including c3 arctic grass, c3 no arctic grass, and c4 grass); c. crop; and d. urban fractional coverage in China.

2) A potential vegetation run with current urbanization (*POT+URB*) was forced with potential vegetation conditions within China, with the *CUR* land cover in the rest of the

world. The potential vegetation distribution, which represents primary land cover conditions without human disturbance, was derived from a historical land use and potential vegetation map (Lawrence and Chase 2010; Ramankutty and Foley 1999). This dataset was selected because it has previously been evaluated and applied to climate studies in East Asia (Liu and Tian 2010; Takata et al. 2009). Figure 4.1a–c shows the fractional changes in PFTs between the *POT+URB* and *CUR* experiments, highlighting the historical vegetation changes as a results of human activities. Extensive deforestation and cropland expansion occurred in eastern and southern China. Approximately 7.4% of the area of China experienced deforestation, which is mainly attributable to the loss of needleleaf evergreen temperate trees, broadleaf deciduous temperate trees, and broadleaf deciduous boreal trees. Consequently, intensified agricultural activities led to an approximate 6.3% increase of cropland in eastern and southern China and northern Xinjiang province. Grassland area decreased in the northeast and northwest (northern Xinjiang province) due to agriculture, grazing, or desertification in these regions. However, grassland coverage increased in southeastern China.

3) A completely natural land cover (*NAT*) run with potential vegetation and no urbanization was forced with potential vegetation in China and without the urban portion, which was proportionally replaced with potential vegetation PFTs. Figure 4.1d shows the distribution of urban areas, accounting for approximately 1.5% of the area of China, and mostly located in eastern and southeastern China. Urbanization is associated with human activities. Therefore, the removal of the urban portion more realistically represents completely undisturbed natural land cover in China.

All three experiments were performed as an ensemble of three 30-year realizations with a 10-year spin-up simulation. The *CUR − POT+URB* difference indicates the possible biogeophysical effects of vegetation changes, while the *CUR − NAT* difference shows the combined effects of vegetation changes and urbanization. Because the climate of China is greatly influenced by the East Asian monsoon, results for summer (JJA) and winter (DJF) are analyzed and the impacts of land cover changes on the East Asian summer and winter monsoon are also discussed. Most of the land cover changes occurred in eastern China, so the average climatic consequences were also quantified over eastern China (20–52°N, 102–130°E).

4.3. Results

4.3.1. Model Evaluation

The model assessment indicates that CESM 1.0.4 capture the spatial distribution of surface air temperature in China well (Figure S1), with a spatial correlation coefficient of 0.88 ($p<0.01$) in summer and 0.96 ($p<0.01$) in winter. However, the model overestimates summer precipitation in the northeast and on the Tibetan Plateau, and underestimated winter precipitation in the southeast (Figure S2). The spatial correlation coefficients between observed and simulated precipitation are 0.61 ($p<0.01$) in summer and 0.64 ($p<0.01$) in winter. Figure S3 shows that the model captures the spatial pattern of atmospheric circulation at 850 hPa well, but overestimates the wind speed of the summer monsoon over eastern China, and fails to represent the southerly wind over

southern China during winter. Overall, CESM 1.0.4 provides a reasonable representation of climate in China, and should therefore be capable of assessing the climatic impacts of land cover changes for our study.

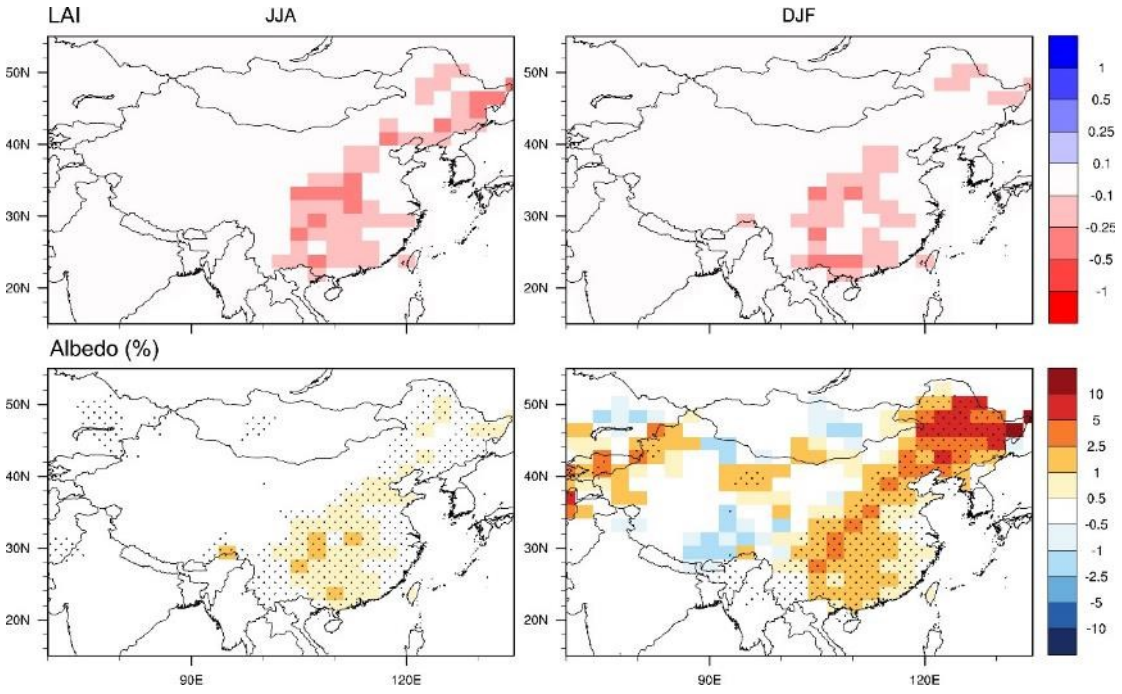

Figure 4.2. Leaf area index (top) and albedo (bottom) change in summer and winter from *CUR − POT+URB* experiments, indicating the effects of only vegetation changes. The dotted areas indicate statistically significant differences at the 95% level.

4.3.2. Changes in Land Surface Characteristics

Land cover changes can modify land surface characteristics such as albedo and leaf area index (LAI). Figure 4.2 shows the changes in LAI and albedo arising from vegetation changes (*CUR − POT+URB* difference). In eastern and southern China, LAI

decreased as a result of deforestation in these regions. Seasonally, we find a smaller decrease in winter because deciduous temperate and deciduous boreal trees already have a lower LAI in the cold season. Generally, albedo increased in the region where land cover change has occurred, which is attributable to the replacement of forest by cropland and pasture (Davin et al. 2007).The increase in albedo is stronger in winter, especially in northeastern China. This was previously reported by Boisier et al. (2013), who found that in northern temperate regions of intense deforestation, a larger albedo increase is observed in summer than in winter because of the presence of snow.

Changes in LAI and albedo from the combined effects of vegetation and urbanization changes (*CUR − NAT*) were also calculated. The same patterns as *CUR − POT+URB* were found, but with slightly greater magnitude (not shown). Urban area accounts for a relatively small portion (<10%) in most grid cells (Figure 4.1d), thus its replacement with vegetation in *NAT* only leads to a slighter greater decrease in LAI from potential vegetation to current day land cover.

As discussed above, land cover changes modify the land surface energy balance, and hence influence local and regional climate. Figure 4.3 shows sensible and latent heat flux as a result of vegetation changes. The sensible heat flux decreases in a large area of China during both summer and winter. The decrease in summer can likely be attributed to an increase in evapotranspiration, while the decrease in winter is caused by an increase in albedo (Figure 4.2). On the other hand, land cover change resulted in a remarkably increased latent heat flux in northeastern, northwestern, and east-central, and southern China in summer. This result is different from previous studies (Lawrence and Chase

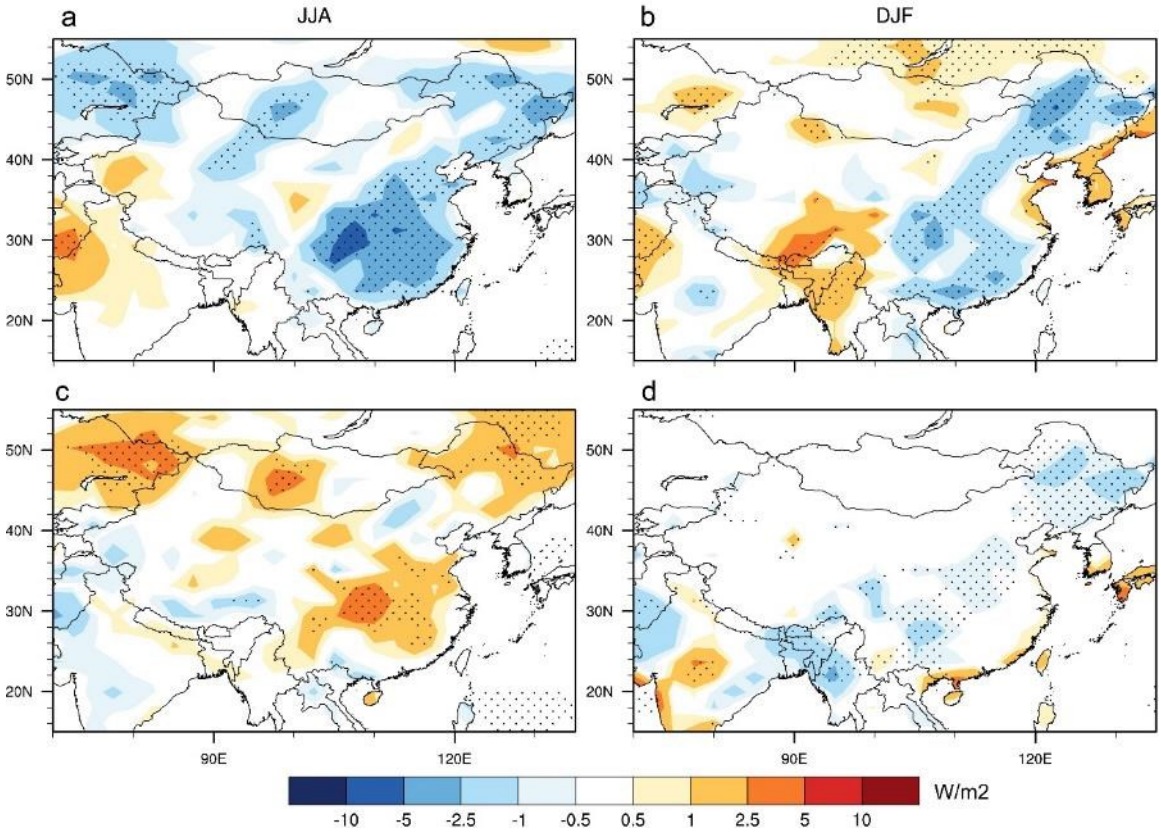

Figure 4.3. Sensible (a–b) and latent (c–d) flux change (W/m^2) in summer (left) and winter (right) from *CUR − POT+URB* experiments, indicating the effects of only vegetation changes. The dotted areas indicate statistically significant differences at the 95% level.

2010), which showed decreases in evapotranspiration in response to global land cover change. Further partitioning evapotranspiration reveals that there is a significant decrease in canopy evaporation, but a strong increase in canopy transpiration and ground evaporation after deforestation. The decrease in canopy evaporation is mainly attributable to the decrease in LAI. However, with the conversion from forest to cropland or grassland, the decreased surface roughness length and stomatal resistance can provide a favorable

environment for evapotranspiration (Bonan 1997; Mahmood et al. 2014; Suh and Lee 2004).

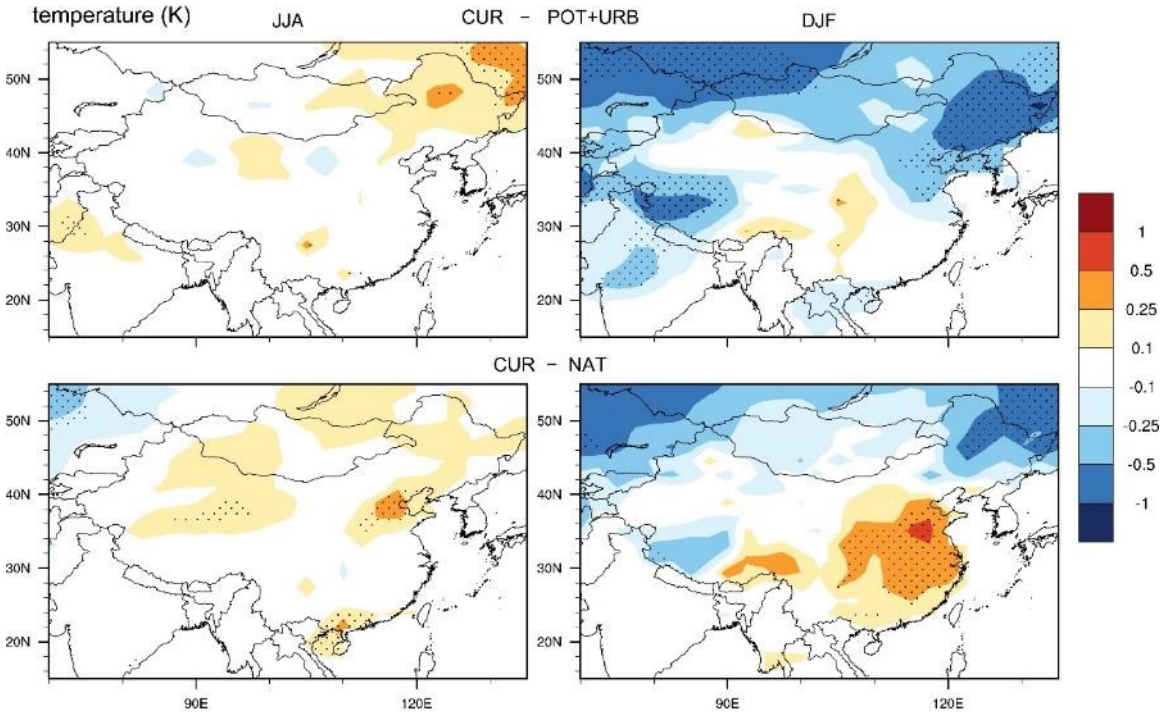

Figure 4.4. Mean surface air temperature changes from vegetation changes only (*CUR − POT+URB*, top) and the combined vegetation and urbanization changes (*CUR − NAT*, bottom). The dotted areas indicate statistically significant differences at the 95% level.

The combined effects from vegetation and urbanization are again similar to the vegetation-only effects (not shown). However, in the east-central and southeast regions, the increase in latent heat flux from agriculture in summer is even larger with the addition of urbanization effects, because urban areas have impervious surface and less vegetation

fraction. Similarly, the decrease in sensible heating from agriculture is also greater with the addition of urban heat island effects.

4.3.3. Temperature Changes

Figure 4.4 shows the mean surface air temperature response from land cover changes in China. When only considering vegetation changes, there is a statistically significant warming in the northeast in summer, and a significant cooling in the northeast and northwest in winter. However, no significant temperature change is found in east-central and southeastern China. The winter cooling is likely due to the increased albedo reported above. Averaged over eastern China, temperature shows a significant decrease (−0.24°C) during winter, but a negligible change in summer. When urbanization is included, the warming effect in summer expands to the south. During winter, a significant warming effect appears in a large area in the east and south, which corresponds well with the urbanized areas of China.

To further examine the temperature response to land cover changes, we calculate daily maximum and minimum temperature changes from *CUR − POT+URB* and *CUR − NAT* (Figure 4.5). Generally, summer daily maximum temperature (T_{max}) decreases in central and eastern China (−0.14°C on average), which is consistent with the area of relatively greater albedo increase. In winter, most of China exhibits cooling (−0.39°C on average) based on on T_{max} when only vegetation change is considered. Urbanization in the southeast offsets the cooling effects from albedo change. The overall T_{max} change in eastern China is approximately −0.15°C when urbanization is considered.

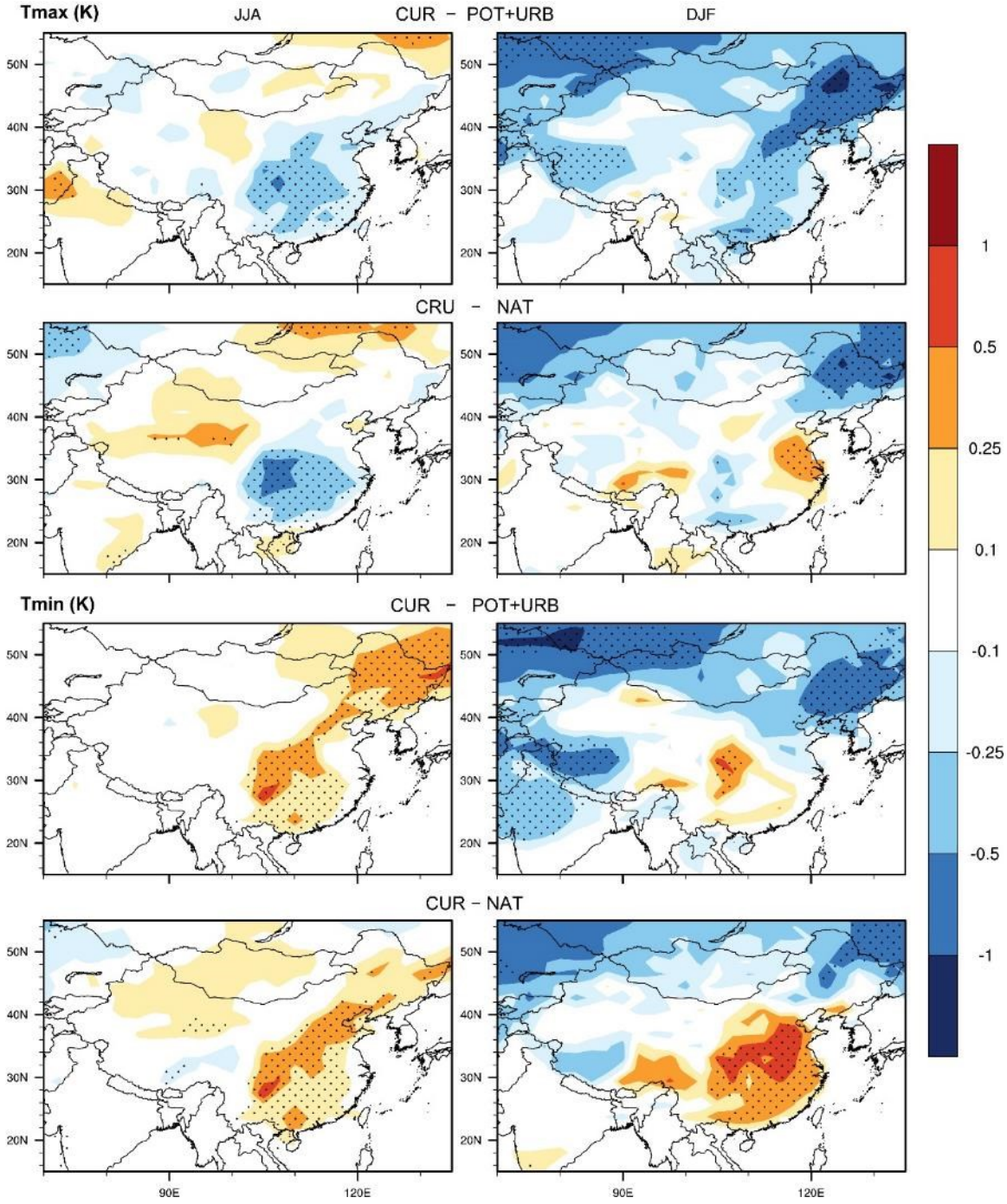

Figure 4.5. Same as Figure 4.4 but for daily maximum (T_{max}) and minimum (T_{min}) temperature (K).

Minimum temperatures (T_{min}) show extensive increases from both vegetation change and urbanization during summer. The T_{min} increased by 0.17–0.19°C in eastern China. The spatial pattern of T_{min} increase shows good agreement with the area of cropland expansion, implying the possible impacts of agricultural activities on climate. This warming effect on T_{min} during summer may be attributable to changes in cloud amount and irrigation. Intensified evapotranspiration could increase clouds, which would exert a warming effect at the surface by delaying longwave radiative losses at night, thus increasing T_{min}. Also, agricultural irrigation can increase the heat capacity of the soil, thus increasing daily minimum temperature (Kalnay and Cai 2003; Mahmood et al. 2004; Sampaio et al. 2007). During winter, T_{min} is barely influenced by agriculture, but urbanization exerts a large warming effect (0.11°C on average).

Finally, observed opposing patterns of daily maximum and minimum temperature can decrease the diurnal temperature range, and also likely explains why there is no significant change in mean surface air temperature in east-central and southeastern China. The reduced diurnal temperature range over eastern China due to land cover changes was also reported in Xu et al. (2015).

4.3.4. Precipitation Changes

The precipitation response to land cover changes is shown in Figure 4.6. Vegetation changes do not have statistically significant impacts on summer precipitation in eastern China, but slightly increase summer precipitation in the northwest while decreasing winter precipitation in southern China. Gao et al. (2003) also suggested that land cover changes in eastern China, mainly due to agricultural practices, do not affect

precipitation in a significant way. When urbanization is also considered, land cover changes are found to increase precipitation in the south and decrease precipitation in the north during summer. Such a southern increase and northern decrease pattern suggests a possible influence of land cover changes on the East Asian summer monsoon.

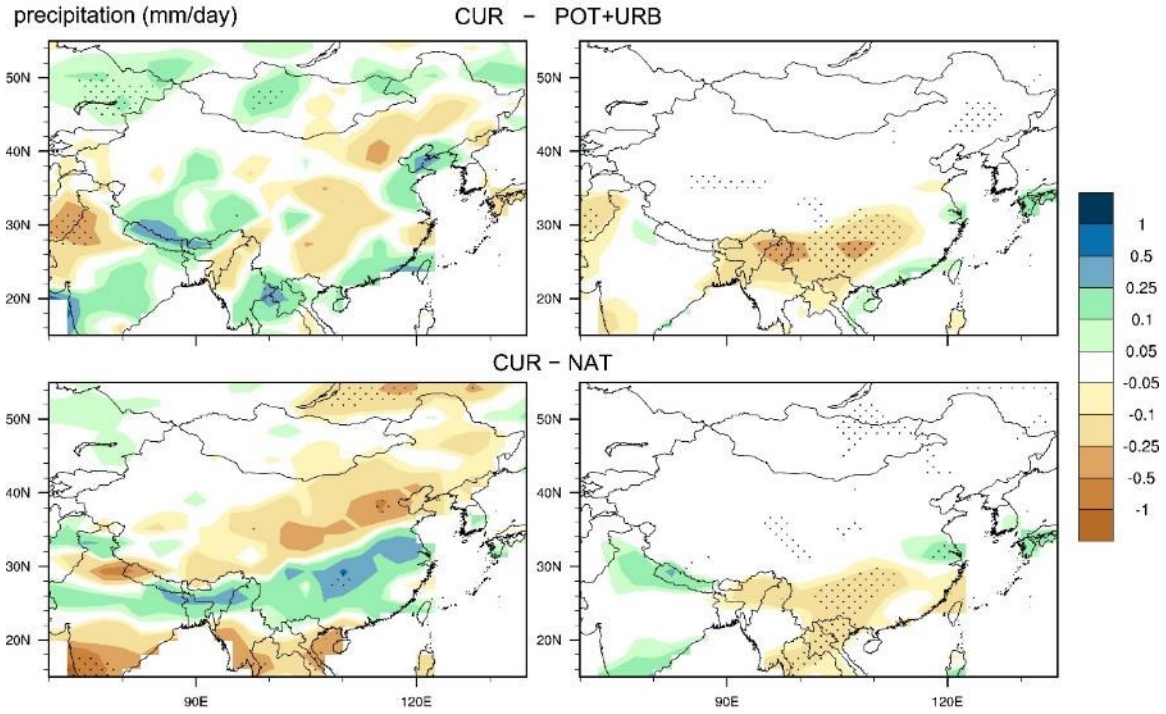

Figure 4.6. Same as Figure 4.4 but for precipitation (mm/day).

The East Asian monsoon is characterized by low-level southwesterly winds during summer and northwesterly winds during winter (Huang et al. 2012). Figure 4.7 shows the wind field changes at 850 hPa associated with historical land cover changes. Vegetation changes do not have noticeable effects on the summer monsoon, however, they can strengthen the East Asian winter monsoon. During summer, there is no significant change

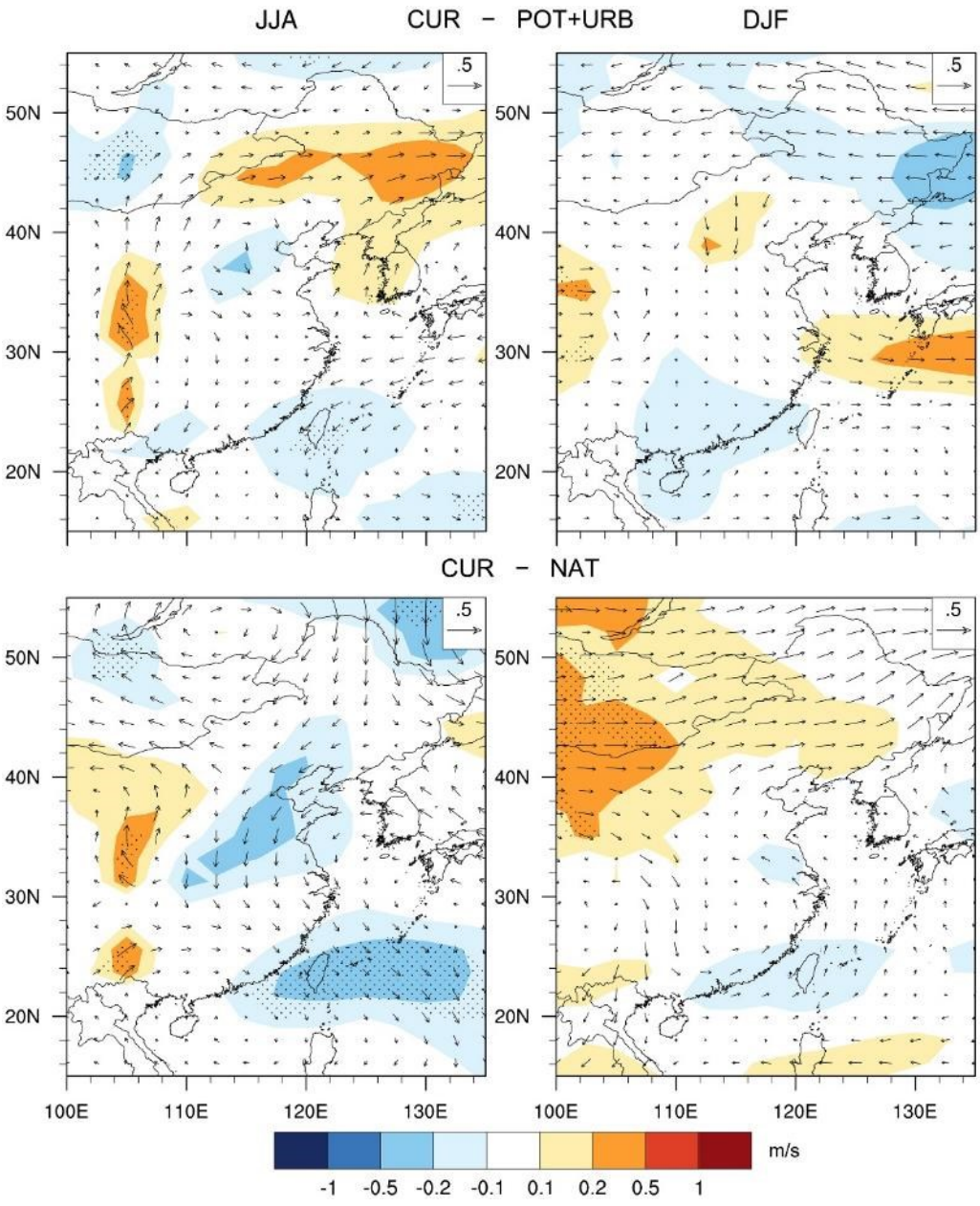

Figure 4.7. Same as Figure 4.4 but for the wind field at 850 hPa (dotted areas indicate 95%, significance for differences in wind speeds).

in surface temperature in eastern and southern China (Figure 4.4). Therefore, vegetation changes may impart little influence on broad-scale atmospheric circulation. However, in

winter there is a large-scale cooling effect in northern China. The increased temperature gradient between land and ocean could intensify the winter monsoon and bring dry and cold air masses from interior Asia to eastern and southern China, therefore decreasing humidity and precipitation.

When urbanization is included in land cover changes, it shows northerly wind anomalies in eastern China and slight southwesterly wind anomalies in southern China (Yunnan and Guangxi provinces) during summer, which can explain the southerly movement of the rain belt (as shown in Figure 4.6). Feng et al. (2013) and Shao et al. (2013) also found a similar pattern in circulation changes in response to large scale urbanization in eastern China in high-resolution regional climate models. However, during winter, there are southerly wind anomalies in eastern China and westerly wind anomalies in northern China, which offset the strengthening effects from vegetation changes, indicating that urbanization can weaken the East Asian winter monsoon due to the surface thermal forcing of urban areas. This finding also agrees with previous studies, which suggest that the weakening of the winter monsoon is forced by surface thermal heating induced by the large-scale urban expansion (Chen and Zhang 2013).

4.4. Discussion and Conclusions

This paper quantifies the biogeophysical effects of historical land cover changes on climate in China using a state-of-the-art GCM. Human-induced vegetation changes and urbanization are evaluated separately as well as combined. Our initial model evaluation

combined with previous findings (Chen and Frauenfeld 2014a, 2014b) suggests a good agreement between observations and model simulations.

Our results indicate that historical vegetation changes alone are able to alter the surface flux balance, thereby modifying regional temperatures. Summer temperature changes are likely due to evapotranspiration and cloud cover, which can decrease daily maximum temperature and increase daily minimum temperature, thus also decreasing the diurnal temperature range. Decreases in winter temperature over northern China are mainly influenced by surface albedo changes. In terms of precipitation, vegetation changes alone do not exhibit statistically significant impacts on summer precipitation or the East Asian summer monsoon, but potentially strengthen the East Asian winter monsoon and decrease winter precipitation in southern China.

Compared with impacts of vegetation changes alone, the addition of urbanization shows more significant and extensive impacts on temperature and precipitation in China. In summer, both vegetation changes and urbanization have a negligible positive effect on mean temperature. However, in winter, a 0.24°C cooling from vegetation changes is offset by a 0.27°C warming from urbanization. The urban heat island effect is also associated with greatly increased minimum temperatures, and shows a remarkable warming effect in southeastern China, especially in winter. When urbanization is also considered, land cover changes are those substantial enough to where they can impact the East Asian summer monsoon and generate increased extremes in summer precipitation where the wet south gets wetter, and the arid north gets drier. Also, urbanization can weaken the East Asian winter monsoon by reducing the land-ocean temperature gradient, and amplify the effects

from vegetation changes. Therefore, it is important to consider urbanization to properly and completely assess the climatic impacts of land cover changes.

Compared with previous studies, this study presents a more complete examination of the biogeophysical effects of historical land cover changes, because we evaluate both vegetation changes and urbanization. However, some limitations still exist. Radiative forcing from surface albedo may also depend on aerosol concentrations (IPCC 2013), which could also be influenced by land cover changes, especially urbanization. In this study, our simulations were forced with the climatological seasonal cycle of aerosol concentrations. Furthermore, due to the complexity of the system, there is still limited understanding of the mechanisms of how land cover changes (including urbanization) impact precipitation. The spatial resolution of our study might be a limitation, because GCMs with coarse resolutions are not able to resolve mesoscale circulation features induced by landscape heterogeneity (Pielke et al. 2007). However, it is still important to use state-of-the-art GCMs to assess their ability to represent climate and explore land-atmosphere interactions in China at regional scales because regional climate modeling is still highly dependent on the quality of the large-scale forcing models.

5. IMPACTS OF URBANIZATION ON FUTURE CLIMATE IN CHINA

5.1. Introduction

Human-induced land cover changes exert significant impacts on climate at regional and global scales by modifying the energy, water, and momentum exchanges between the land surface and atmosphere. Urbanization, one of most extreme and increasing land cover changes, is considered to play an important role in local weather and regional climate because of its effects on both temperature (Oke 1982) and precipitation (Shepherd 2005). Urban areas are warmer, like an "island" of heat surrounded by cooler rural areas (Shastri et al. 2015). This is known as urban heat island effect because of the low albedo, large heat-storage capacity of urban surfaces (Kalnay and Cai 2003), and anthropogenic heat emission (Grimm et al. 2008; Ichinose et al. 1999). Also, it has been reported that urbanization can influence precipitation patterns. The impervious surface of urban areas can largely reduce the moisture available for evaporation. The urban heat island effect may influence the development of clouds, convection, and rainfall patterns over the urban areas (Shepherd 2005). Furthermore, surface winds can be affected; buildings in urban areas may increase surface roughness, thus decreasing surface wind speed. The urban-induced sensible heat fluxes can modify vertical momentum fluxes through boundary layer convection (Vautard et al. 2010).

China is a fast growing country with rapid urbanization. Its gross domestic product grew at an average rate of 9.5% from 1978 to 2000, compared with 5% in developing countries and 2.5% in developed countries (Zhou et al. 2004). Urban population in China

increased from 191 million in 1980 to 622 million in 2009, which was largely driven by rural-to-urban migration (Gong et al. 2012). In the future, China is projected to have the second-largest (after India) urban population growth by 2050 (United Nations, 2014). Therefore, not only has urbanization in China become a critical socio-economic topic, but it also has crucial implications for the climate system.

Previous studies have demonstrated the possible effects of urbanization on both temperature and precipitation in China. Jones et al. (2008) found an urbanization-related warming of about 0.1°C per decade over China for the period 1951−2004. However, the warming effects are different from region to region (Li et al. 2004). Based on in-situ observations from 1979 to 1998, Zhou et al. (2004) suggested that the rapid urbanization in southeastern China has increased mean surface temperature at a rate of 0.05°C per decade. For northern China, the contribution of urban warming is estimated to be to 0.11°C per decade for the period 1961−2000 (Ren et al. 2008). In addition to this observational evidence, climate models have also been used for urbanization-related climate studies at different scales and regions, such as in Beijing (Miao et al. 2009; Zhang et al. 2014), the Yangtze River Delta (Liao et al. 2014; Wang et al. 2015), the Pearl River Delta (Wang et al. 2013; Zhao et al. 2013), and China as a whole (Chen and Zhang 2013; Feng et al. 2013; Feng et al. 2012; Feng et al. 2014; Shao et al. 2013; Wang et al. 2012). For instance, Wang et al. (2012) found that urban expansion can lead to increased surface air temperature, enhanced convergence, decreased cloud fraction, and changes in regional precipitation. Furthermore, urbanization is also able to influence the East Asian monsoon system (Feng et al. 2013).

Despite the well-documented significant impacts of urbanization on climate at both local and regional scales, projections of future climate have rarely considered the possible increases of urban area in their land cover change scenarios. In CMIP5, even though land cover changes have been included in the climatic forcings of some modeling groups (Table 2.1), usually urban fraction still remains constant over time (Di Vittorio et al. 2014). Mahmood et al. (2014) suggest that urban forcing should be included in future climate modeling systems because of its impacts on atmospheric dynamics, thermodynamics, energy exchanges, cloud microphysics, and composition.

Therefore, in this section, a regional climate model is used to investigate the impacts of urbanization in China on future climate. We use the WRF model to dynamically downscale future climate projections from CESM. Impacts of urbanization were detected based on two land cover scenarios. The unique contributions of this study are that it is the first to estimate how possible future urbanization affects climate in China, and also the first to examine whether future urbanization has a comparable impact on climate as greenhouse gas forcing.

5.2. Model Description and Experimental Design

5.2.1. WRF Model

The WRF model version 3.5 is used for regional climate simulations. A regional climate model is used here because the coarse resolution of GCMs precludes an accurate depiction of urbanization. In section 4, the horizontal resolution of CESM is 1.9° latitude

× 2.5° longitude, which cannot adequately resolve the scale of urban areas or mesoscale physical processes. Therefore, regional climate modeling is better suited because it provides a higher spatial resolution and a better representation of physical processes and feedbacks occurring at regional scales, especially in areas with complex land surface conditions, such as heterogeneous land cover and terrain. Furthermore, a number of studies have successfully used WRF to examine the influence of urbanization on climate in China (Feng et al. 2012; Feng et al. 2014; Miao et al. 2009; Wang et al. 2012). Therefore, the WRF model seems able to capture the land-atmosphere interactions such as those related to urbanization over China.

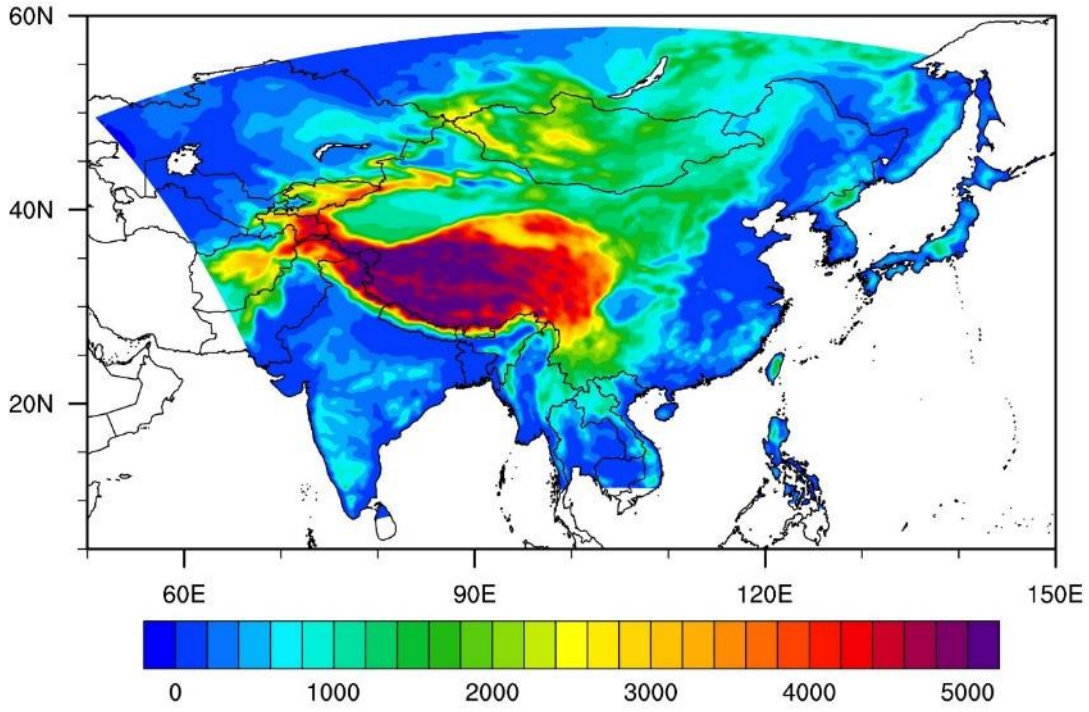

Figure 5.1. The model domain with elevation in meters at 30 km × 30 km resolution.

The model domain of this study covers the entire region of China at a horizontal resolution of 30 km (Figure 5.1). The domain is centered at 35°N and 103°E, with dimensions of 240 grid cells west–east × 180 grid cells south–north, and the top model level is at 50 hPa. In this study, the resolution might still not be adequate to describe some cities. However, this spatial resolution has been adopted in previous studies employing WRF climate downscaling over China (Feng et al. 2013; Gao et al. 2015; Liu et al. 2013) and should also be effective for capturing land-atmosphere interactions in our study.

Table 5.1. Parameterization of physical processes in the WRF model configuration.

Physical processes	**Parameterization**
Microphysics	WRF Single-Moment 3-class scheme (Hong et al. 2004)
Longwave Radiation	RRTM scheme (Mlawer et al. 1997)
Shortwave Radiation	Dudhia scheme (Dudhia 1989)
Planetary Boundary layer	Yonsei University scheme (Hong et al. 2006)
Cumulus Parameterization	Kain-Fritsch scheme (Kain 2004)
Land Surface	Noah Land Surface Model (Tewari et al. 2004)
Urban Surface	Single-layer UCM (Kusaka and Kimura 2004)

The parameterization of physical processes (Table 5.1) was chosen based on previous studies (Feng et al. 2012; Wang et al. 2012). For land surface processes, the Noah land surface model (Chen and Dudhia 2001) was coupled with the Urban Canopy Model (UCM; Kusaka and Kimura 2004; Kusaka et al. 2001). The UCM is a single-layer model that

simulates energy and momentum exchange between an urban surface and the atmosphere (Kusaka et al. 2001). Over urban areas, surface temperatures and heat fluxes are estimated from three surface types: roof, wall, and road.

5.2.2. Lateral Boundary and Initial Conditions

For the WRF downscaling of future climate projections, the "Global 6-hourly Bias-corrected CMIP5 CESM" (Monaghan et al. 2014) dataset is used as the lateral boundary and initial conditions. This dataset is generated based on the output from the simulation of CCSM4 ensemble member #6 for each scenario in the CMIP5 archive. This dataset was chosen because CESM (CCSM4) ranks as the best of the CMIP5 GCMs in terms of simulating observed temperature and precipitation at the global scale (Knutti et al. 2013). It also performs well in simulating climate (especially temperature) variability in China (Chen and Frauenfeld, 2014a). Therefore, it likely provides relatively robust boundary conditions for WRF, compared to other GCMs. Furthermore, the CESM output has been bias corrected. As indicated in section 2, all GCMs, including CESM, contain biases at the regional scale due to both their coarse resolution, and their limited representation of certain physical processes. These biases will also affect the quality of the downscaling. In the Monaghan et al. (2014) dataset, the ECMWF's Interim Reanalysis (ERA-Interim; Dee et al. 2011) was used for bias correction, where the bias-corrected CESM output is generated by summing the 1981-2005 average 6-hourly annual cycle from ERA-Interim with a 6-hourly perturbation term from CESM (Bruyère et al. 2014).

From the bias-corrected CESM output, 11-year historical (1995−2005) and RCP4.5 (2050−2060) simulations are used as lateral boundary and initial conditions in WRF. The

RCP4.5 scenario represents a moderate future climate warming pathway. The first year is considered as spin-up period and only 10-year results are analyzed. The SST and deep soil temperature are actively updated during the simulations.

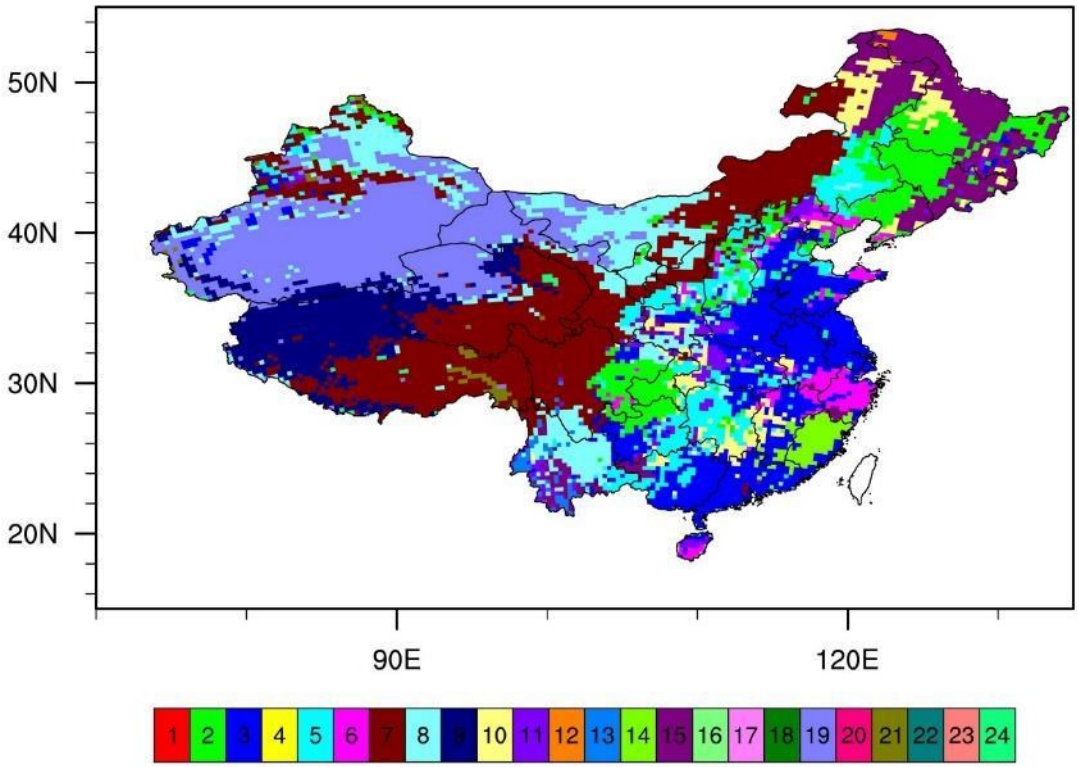

Figure 5.2. The USGS 24-category land use conditions over China used in the *HIST* run; 1: Urban and Built-Up Land, 2: Dryland Cropland and Pasture, 3: Irrigated Cropland and Pasture, 4: Mixed Dryland/Irrigated Cropland and Pasture, 5: Cropland/Grassland Mosaic, 6: Cropland/Woodland Mosaic, 7: Grassland, 8: Shrubland, 9: Mixed Shrubland/Grassland, 10: Savanna, 11: Deciduous Broadleaf Forest, 12: Deciduous Needleleaf Forest, 13: Evergreen Broadleaf, 14: Evergreen Needleleaf, 15: Mixed Forest, 16: Water Bodies; 17: Herbaceous Wetland, 18: Wooden Wetland, 19: Barren or Sparsely Vegetated, 20: Herbaceous Tundra, 21: Wooded Tundra, 22: Mixed Tundra, 23: Bare Ground Tundra, 24: Snow or Ice.

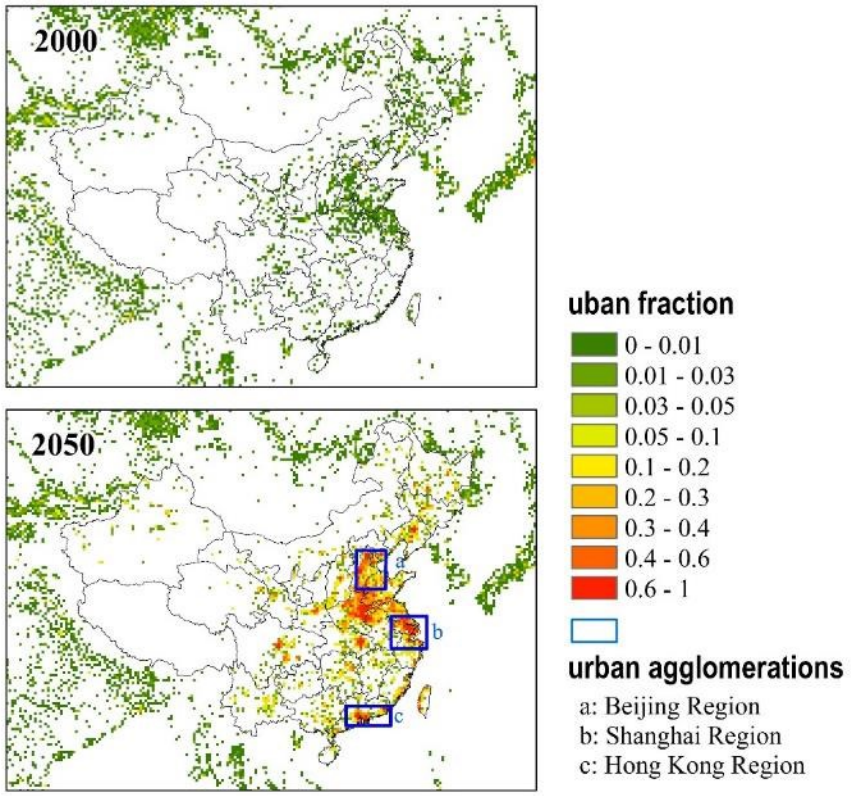

Figure 5.3. Urban fractions in 2000 and 2050 specified in the WRF model, with the three subregions (bottom) considered as urban agglomerations.

5.2.3. Experimental Design

We conduct three experiments to investigate the climatic impacts of future urbanization in China. 1) *HIST*: A historical run (1995−2005) forced with current land cover conditions, which is prescribed using the USGS 24-category land use data (Figure 5.2). 2) *RCP45*: An RCP4.5 scenario run (2050−2060) forced with current land cover conditions. 3) *URB*: An RCP4.5 scenario run (2050−2060) forced with future urbanized land cover conditions. The *RCP45 – HIST* difference shows future climate change due to

greenhouse gas forcing in RCP 4.5, while the *URB – RCP45* difference shows the impacts of urbanization on future climate.

Future urban area was derived from global forecasts of urban expansion (Seto et al. 2012). The probability of urbanization in 2030 was estimated based on global urban extent circa 2000, urban population, population density, and country-level gross domestic product projections in 2030. From the 2030 urban forecast data, grid cells with urbanization probability higher than 75% (Güneralp et al. 2015) were considered as urban area in 2050. This is based on the assumption that, if a pixel has a high probability of urbanization in 2030, it will likely have a similar or higher probability of becoming urban in 2050. Figure 5.3 shows the urban fractions in 2000 and 2050 specified in the WRF model. Extensive urbanization is evident in eastern and southeastern China, which correspond to the most developed and populated areas in this country.

In the future urbanized land cover scenario, urban fraction in each grid cell was increased based on the urban projection from Seto et al. (2012). Vegetated land cover categories were proportionally replaced by urban area. Only grid cells in China were modified for future urbanization, while other grid cells were kept the same as current land cover conditions. Figure 5.4 shows the four land cover types with the largest changes in 2050 after the projected urbanization has occurred. Cropland is the major land cover type that will be encroached upon by urban area in the future. The total increase in urban area will be 2.6% in China. Consequently, cropland will decrease by 2.2% in 2050 due to urbanization, with the remaining 0.4% accounted for grassland and forest.

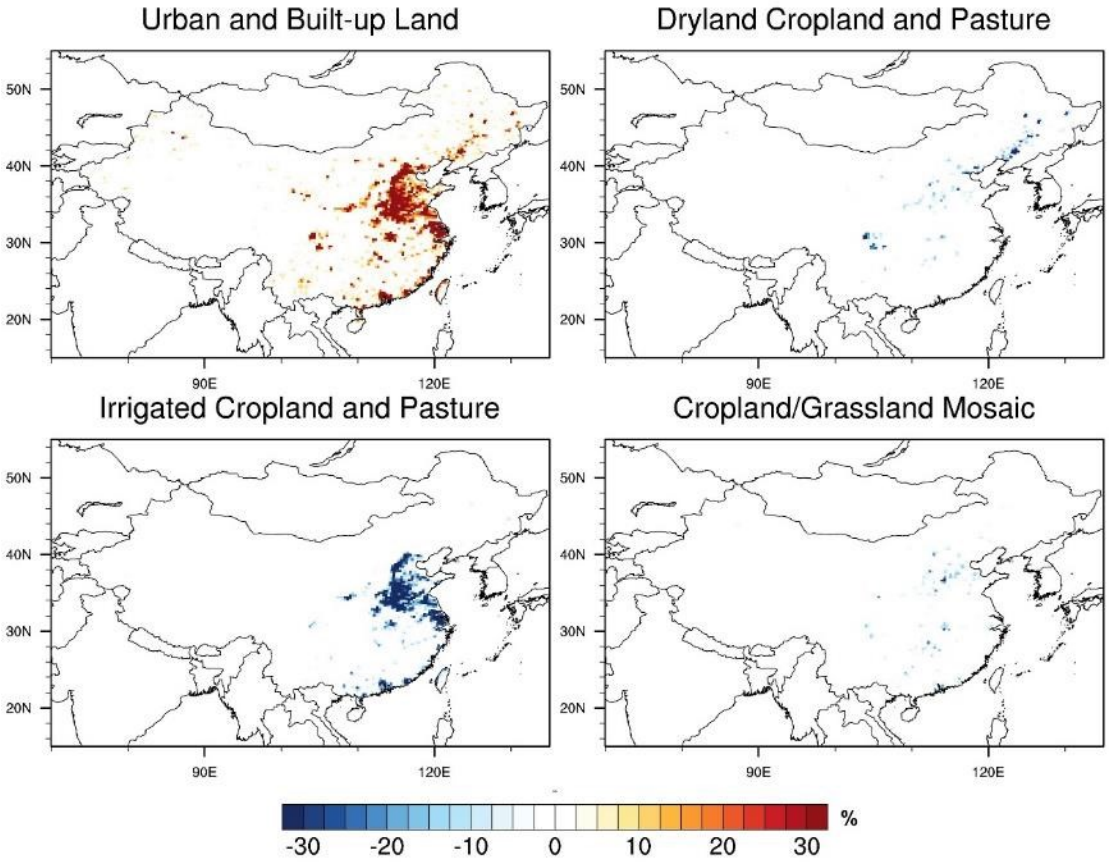

Figure 5.4. Four land cover types with the largest changes in 2050 after urbanization has occurred.

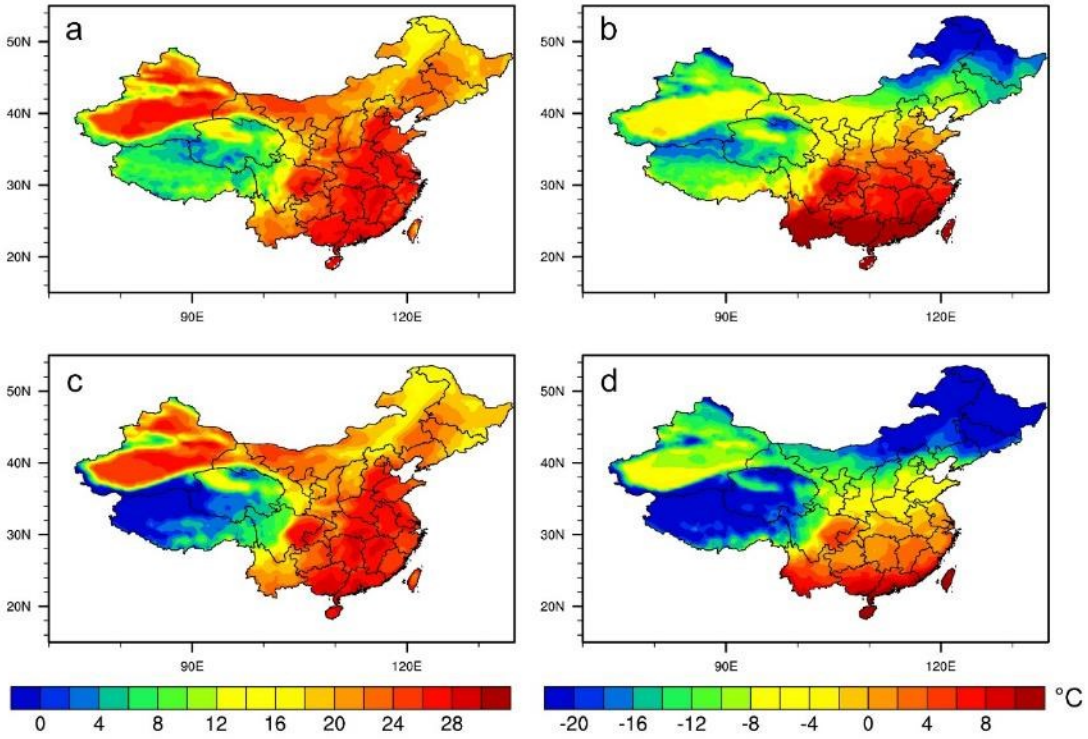

Figure 5.5. Comparison of summer (JJA, left column) and winter (DJF, right column) 2 m air temperature (°C) between CRU observation and *HIST* run.

5.3. Results

5.3.1. Evaluation of WRF Downscaling

To first assess the performance of the WRF downscaling, results from *HIST* are compared with CRU temperature and precipitation observations (Harris et al. 2014). Figure 5.5 shows that WRF exhibits a good spatial agreement with the observed climatology of seasonal surface air temperature, with a spatial correlation coefficient of 0.96 ($p<0.01$) in both summer and winter. In summer, WRF well captures the hot regions, such as the Tarim Basin in the Xinjiang Province, Sichuan Basin, Hubei, and Hunan

provinces. In winter, a systematic cold bias exists in simulated temperature. This cold bias is large over the Tibetan Plateau, which can be attributed to cold biases in the original GCMs (Chen and Frauenfeld 2014b) and the high elevation and complex terrain in this region (Gao et al. 2015).

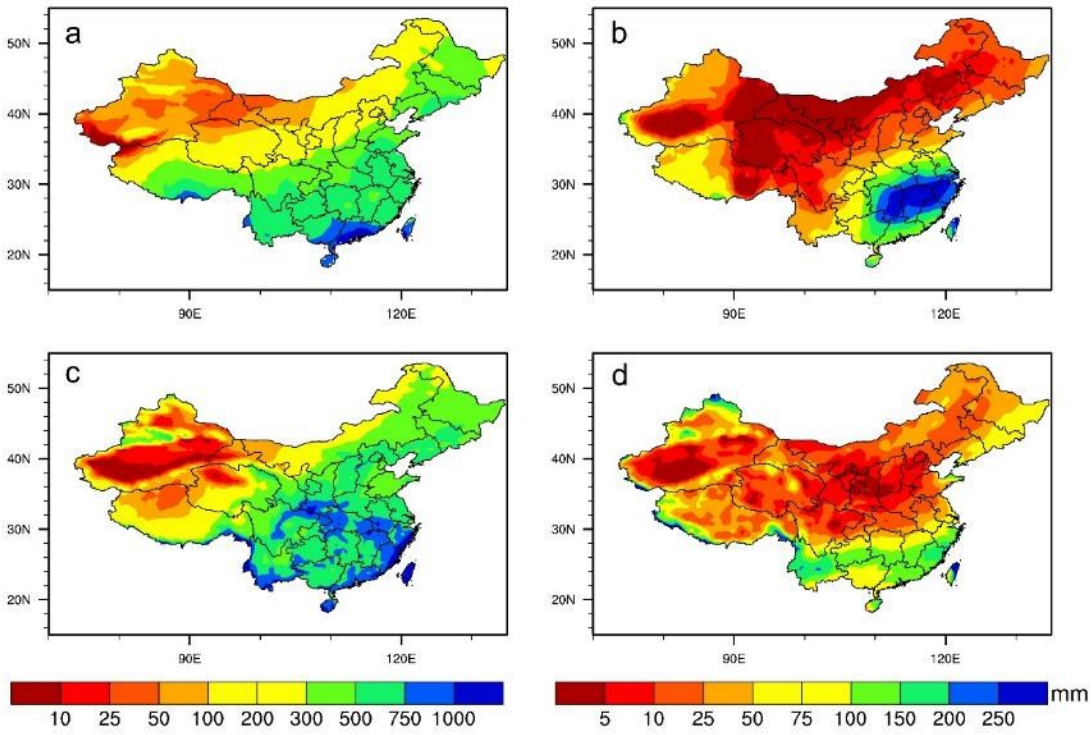

Figure 5.6. Same as Figure 5.5 but for precipitation (mm).

Figure 5.6 shows the comparison between observed seasonal precipitation and the *HIST* WRF simulation. Similar to previous studies applying dynamically downscaled precipitation over China (Gao et al. 2011; Gao et al. 2012; Liu et al. 2013), WRF only simulates precipitation fairly over China, with a spatial correlation coefficient of 0.77

($p<0.01$) in summer and 0.54 ($p<0.01$) in winter (Figure 5.6). In summer, the CRU observations show low precipitation in northern China, and high precipitation in the southeast with the largest precipitation amounts in southern China as a result of the East Asian summer monsoon. WRF well reproduces the basic spatial pattern of precipitation distribution, however, it overestimates the precipitation in southwestern China and the Yangtze River delta regions. The wet bias in southwestern China can result from the overestimated precipitation in the GCMs (Chen and Frauenfeld 2014a) and the influence of the Tibetan Plateau. However, the wet bias over the Yangtze River delta region may be attributed to the uncertainties of the observational data. Feng et al. (2012) presented observed precipitation over China based on Tropical Rainfall Measuring Mission (TRMM) data, which show high precipitation over the Yangtze River delta region. During winter, the observed precipitation decreases from the southeast to the northwest. However, WRF largely underestimated precipitation in the southeast and overestimated precipitation in the southwest. Yuan et al. (2012) also found such a winter dry bias over southeastern China, which might be attributed to the selection of land surface schemes. They suggested that the Rapid Update Cycle (RUC) land surface scheme can a produce better climatology of winter precipitation in southern China than the Noah land surface scheme. However, the RUC land surface scheme does not support the urban model in WRF, which is only available for the Noah model. Based on the above assessment and previous studies, WRF seems capable of providing reasonable dynamically downscaled high-resolution climate simulations for this study. However, due to the large bias evident over the Tibetan Plateau, this region will be excluded from our analyses.

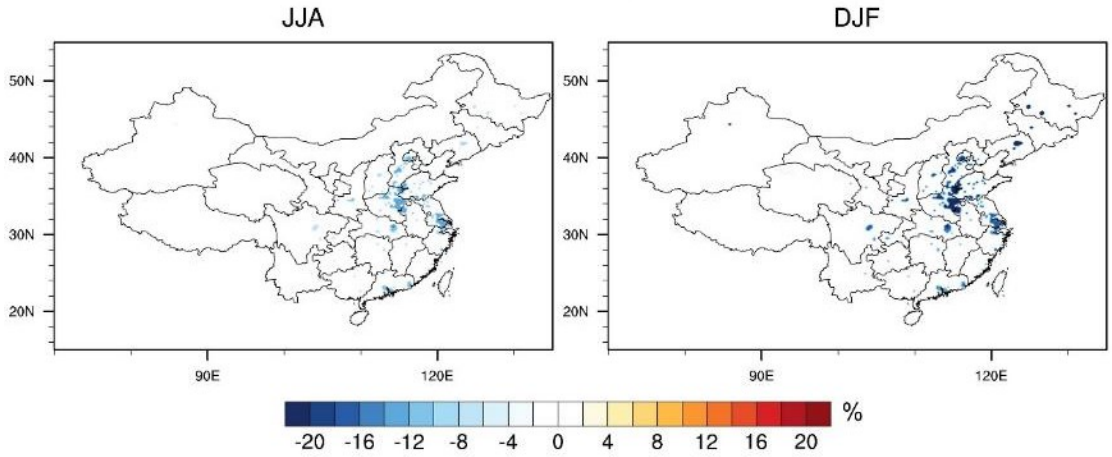

Figure 5.7. Albedo changes (%) in summer and winter after urbanization.

5.3.2. Changes in Land Surface Characteristics after Urbanization

Urbanization can modify the surface characteristics and influence the land surface energy balance. Figure 5.7 shows surface albedo in the *HIST* experiment and its changes after urbanization in 2050. The surface albedo is high in northern China and low in eastern and southeastern China. After urbanization, albedo decreased mainly over the urbanized area. In the Noah model, the surface albedo is calculated based on vegetation fractions for each grid cell. Compared with vegetated areas (e.g., cropland), urban surfaces have a lower albedo. Also, it is found that the albedo decrease in winter is larger than in summer. This is because cropland has a low albedo in summer during the growing season, and a high albedo in winter after harvest.

Due to the unique thermal properties of urban surfaces, we also examine the changes in surface sensible and latent heat fluxes after urbanization (Figure 5.8). Generally, urbanization tends to increase the surface sensible heat but decrease the latent heat flux

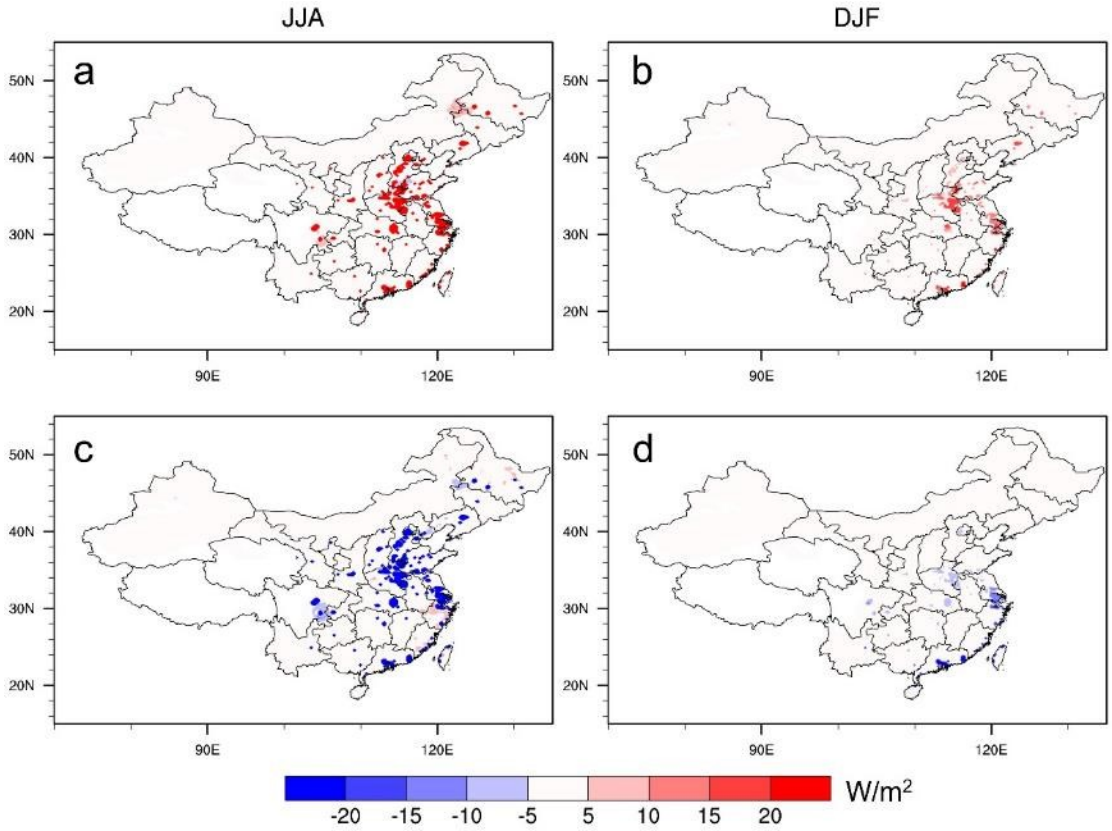

Figure 5.8. Same as Figure 5.7 but for sensible heat (a-b) and latent heat (c-d) fluxes (W/m^2).

over the urban area. The decrease in vegetation, which is replaced with urban area, combined with the impervious surface of urban area, may reduce evapotranspiration and thus decrease the latent heat flux. For the sensible heat flux, its increase can also be attributed to the albedo decrease and the thermal properties of urban surfaces. Seasonally, larger heat flux changes are found in summer. This can be explained in terms of the surface receiving the highest insolation in summer, which exerts the strongest influence on the surface energy budget. Also, evapotranspiration is the strongest in summer, therefore the

latent heat flux would be decreased the most during this season as a consequence of urbanization.

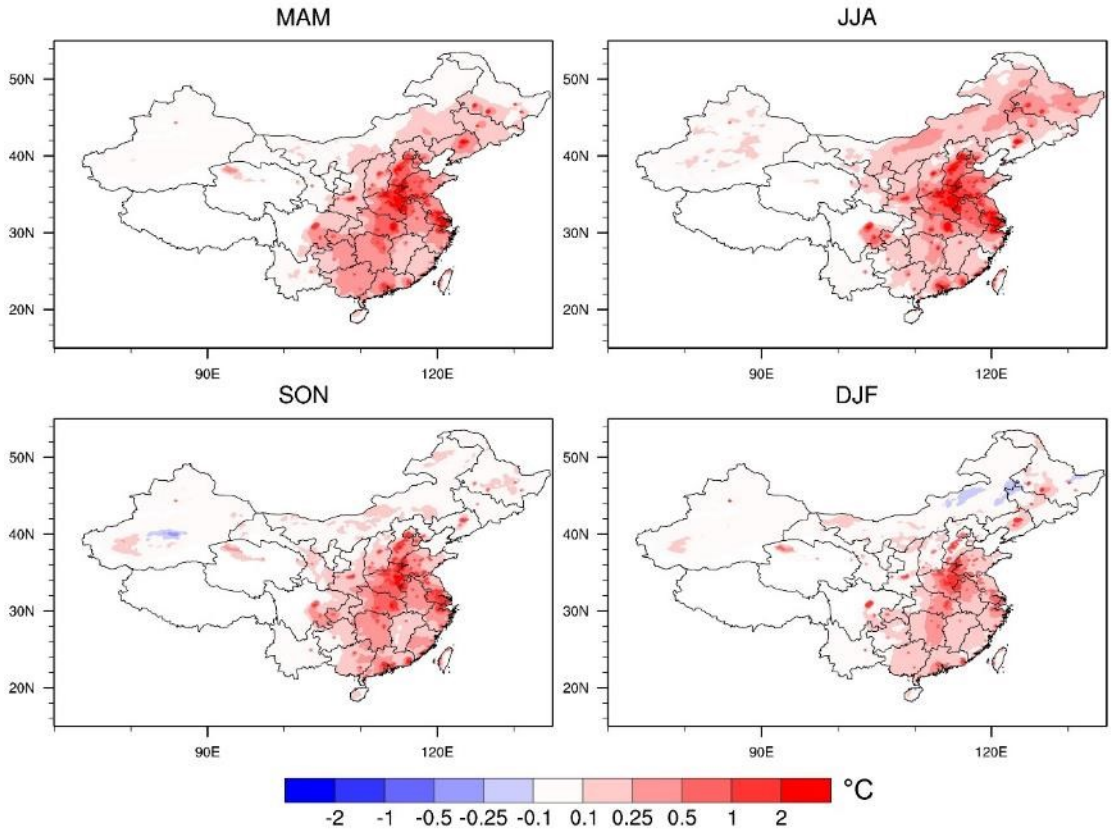

Figure 5.9. Seasonal temperature changes (°C) after urbanization.

5.3.3. Impacts on Surface Temperature

With the decreased surface albedo and increased sensible heat flux, urbanization exhibits a significant impact on future temperature (Figure 5.9). Warming effects are found in eastern China, with the greatest temperature increase over the urban agglomerations. The small urban areas, especially in the northwest (such as Lanzhou, Gansu Province and Urumqi, Xinjiang Province), also show warming after urbanization.

The increase in temperature is the greatest and most extensive during summer, followed by spring and autumn, while winter undergoes the smallest projected warming. The seasonal pattern of temperature change can be explained by the surface heat flux changes. Previous observation-based studies similarly found that the greatest warming due to urbanization is observed in the warm season. Based on 282 meteorological stations in northern China, Ren et al. (2008) suggested that urban warming contributes the most to temperature changes in summer, and fall and spring also show large contributions. This largest contribution of urban warming in summer and smallest contribution in winter was previously also reported for eastern China (Yang et al. 2011).

We also focus on three important urban agglomerations in China: the Beijing region, Shanghai region, and Hong Kong region (Figure 5.3). These regions are defined based on Feng et al. (2013), and allow us to further assess the temperature impacts of urbanization at local and regional scales. The three urban agglomerations are chosen because they exhibit the greatest increases in urban development nationwide (Feng et al. 2013). Table 5.2 compares the warming effects of greenhouse gas forcing and urbanization for China, and for three urban agglomerations. The grid cells with urban fractions higher than 50% are considered as metropolitan areas and are calculated separately, so that the impacts of urbanization at local and broader (regional) scales can be discerned. Under the RCP 4.5 scenario, surface air temperature increases significantly throughout the year. Mean annual temperature is projected to be 1.8°C higher than present over China, with a larger warming in winter than in summer. The temperature increase is larger in the north (Beijing) than the southeast (Shanghai and Hong Kong). Similar warming is found in the metropolitan

and surrounding areas, because urbanization is not included in the RCP experiments for future climate projections in CMIP5. At the regional (country-wide) scale, urbanization increases the mean annual temperature by only 0.2°C over all of China, with a larger warming in summer. However, urbanization has much stronger impacts on temperature at local scales, such as metropolitan areas. Temperature can increase as much as 1.9°C in urban areas, which is comparable to and has even exceeded the warming effects resulting from greenhouse gases.

Table 5.2. Temperature changes for the three subregions and China in the *RCP* (*RCP45* − *HIST*) and *URB* (*URB* – *RCP45*) experiments. Statistically significant differences (95% level) are shown with asterisks. Metro indicates that only urban areas (urban fraction > 50%) were considered.

Regions	***RCP*** (°C)			***URB*** (°C)		
	Annual	Summer	Winter	Annual	Summer	Winter
Beijing Region	1.9*	1.3*	3*	0.6*	1.0*	0.3
Shanghai Region	1.4*	1.2*	1.1*	0.8*	1.3*	0.3
Hong Kong Region	1.2*	0.5*	1.4*	0.6*	0.8*	0.3
China	1.8*	1*	2.3*	0.2	0.2	0.1
Beijing Metro	1.9*	1.2*	3*	1.8*	2.6*	1.0
Shanghai Metro	1.3*	1.3*	0.9*	1.8*	2.7*	0.7
Hong Kong Metro	1.9*	0.5*	0.9*	1.4*	1.9*	0.7
China Metro	1.6*	1*	2*	1.9*	2.4*	1.1*

The impacts of urbanization on temperature during day versus night were also examined (Figure 5.10). Generally, the warming effects of urbanization are stronger

during night than day (except in Hong Kong). The larger warming effect during night was also found in previous studies (Kalnay and Cai 2003; Wang et al. 2012), and can be explained by the high heat capacity in urban areas. During day, urban surfaces with low albedo absorb and store energy, but less evapotranspiration limits surface-to-atmosphere energy release, which persists into the night and thereby increases nighttime temperatures.

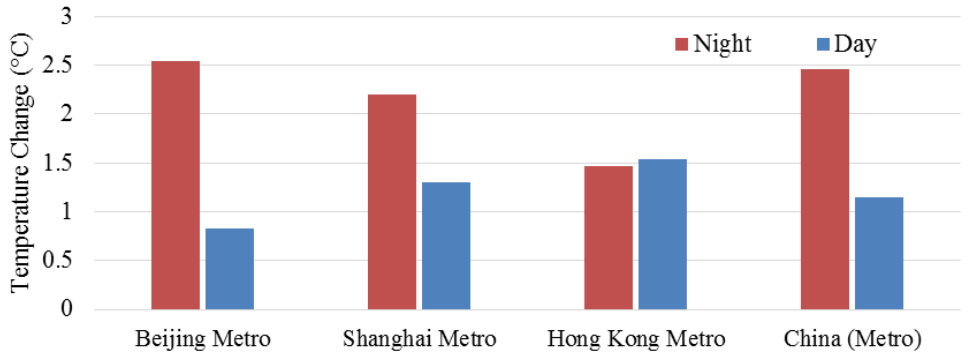

Figure 5.10. Daytime and nighttime 2 meter air temperature changes (°C) over urban areas in three subregions and China after urbanization.

5.3.4. Impacts on Precipitation

The impacts of urbanization on precipitation do not have uniform patterns, like those on temperature changes. The spatial distribution of seasonal precipitation changes is shown in Figure 5.11. In summer, precipitation decreases in southeastern China, especially over the Shanghai region, and increases over southern China (Hong Kong region) and Beijing region. These results agree with the conclusions of Feng et al. (2012), who also found an increase in precipitation in the Beijing-Tianjin-Hebei region and a decrease in

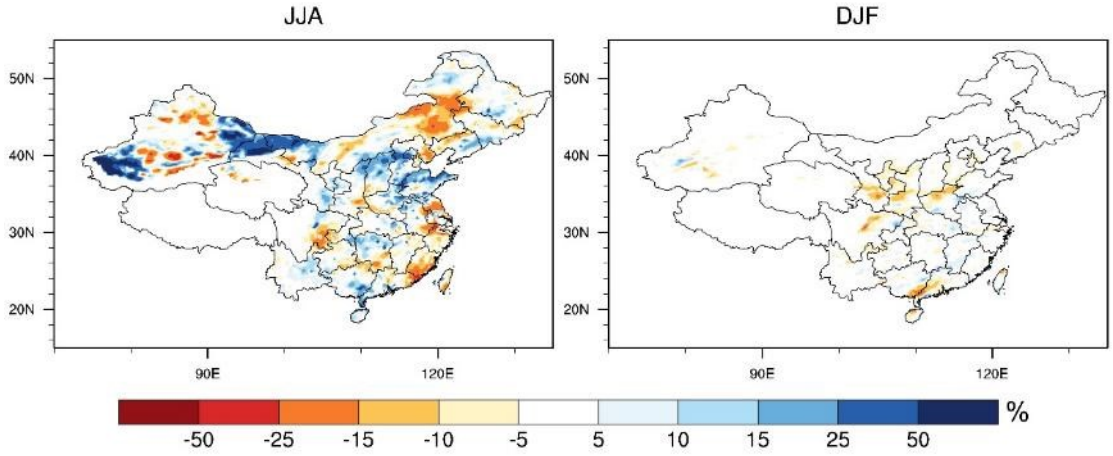

Figure 5.11. Same as Figure 5.7 but for precipitation (%).

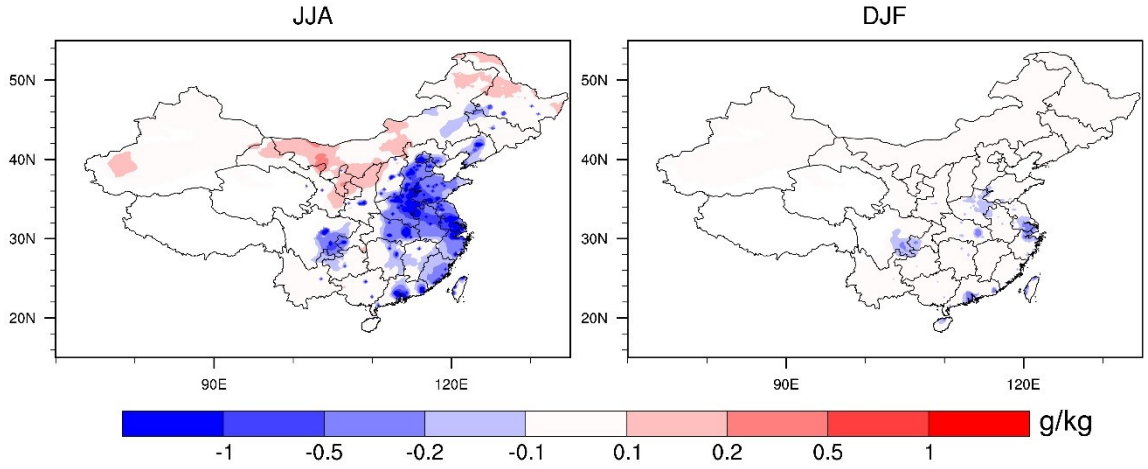

Figure 5.12. Same as Figure 5.7 but for 2 meter specific humidity (g/kg).

the Yangtze River delta region. Using two nested domains in the WRF model, Wang et al. (2013) suggested urbanization in the Pearl River Delta (Hong Kong region) may increase annual total precipitation due to an increase in heavy and extreme rain events. In winter, the impacts of urbanization on precipitation are very small. This is because the

precipitation in most areas of China is controlled by the East Asian monsoon system, in which precipitation is dominant in summer whereas there is little winter precipitation.

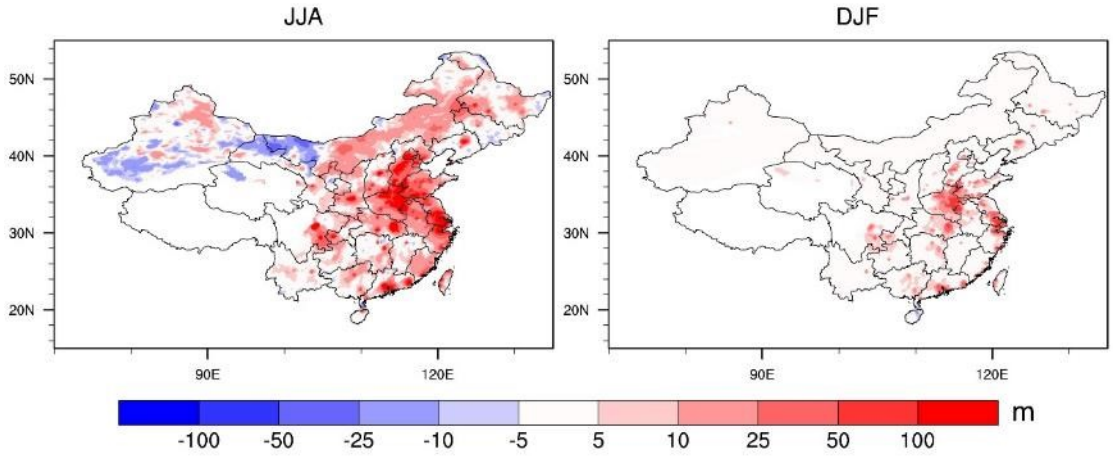

Figure 5.13. Same as Figure 5.7 but for planetary boundary layer height (meter).

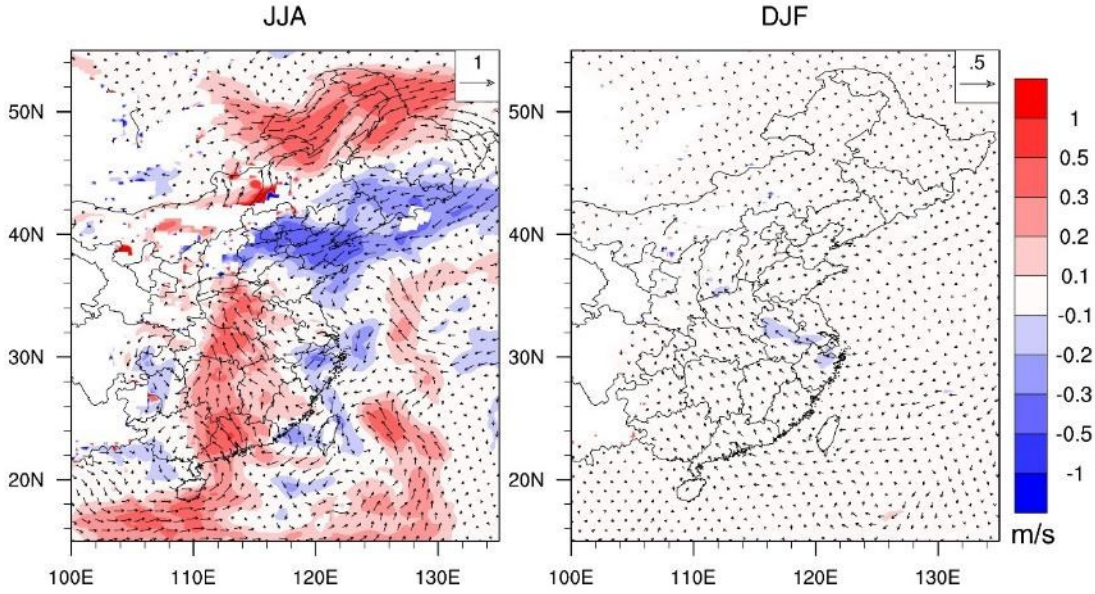

Figure 5.14. Same as Figure 5.7 but for wind field at 850 hPa (m/s).

To investigate the possible reasons for precipitation changes, impacts on 2 m specific humidity, the height of the planetary boundary layer (PBL), and the East Asian monsoon are also examined. Figure 5.12 shows the changes in surface specific humidity after urbanization. During summer, there is a significant decrease in specific humidity over urban areas (by up to -1.0 g/kg over Shanghai and Hong Kong). The change in specific humidity in winter shows a similar pattern, but with a much smaller decrease. Decreasing specific humidity can be attributed to the decrease in evapotranspiration after urbanization. This may reduce atmospheric moisture and therefore decrease precipitation in these regions. Many studies indicate that precipitation over urban areas is strongly related to the structure of the urban boundary layer (Huszar et al. 2014; Niyogi et al. 2010; Wang et al. 2012). The impacts of urbanization on the PBL height are presented in Figure 5.13. Generally, the PBL height increases over the urban area, with a stronger and more extensive increase in summer (up to 100 m) than in winter, as a result of the increased sensible heat fluxes. As also found in previous studies (Shimadera et al. 2014), the increased PBL height indicates that the atmosphere over the urban area is likely more unstable and tends to develop more convective clouds, causing more precipitation from afternoon to evening. However, the deficit of atmospheric moisture over the urban area may offset the impacts from the elevated PBL.

Finally, urbanization likely influences the East Asian monsoon system. To investigate this potential effect, we quantify the changes in the 850 hPa wind field in summer and winter (Figure 5.14). In summer, the strong warming effects of urbanization can increase the temperature gradient between the ocean and the land, thus strengthening

the summer monsoon in the south. Indeed, easterly wind anomalies are evident in the 850 hPa fields, advecting moisture over the Beijing region. This potentially accounts for the precipitation increases over this region. However, because urban heating in winter is not as strong as in summer, the influence of urbanization on the winter monsoon is very small, and is only evident over the Yangtze River delta region. That likely also explains why the winter precipitation changes are negligible in response to urbanization.

5.4. Discussion and Conclusions

Urbanization in China impacts future climate through changes in the energy, water, and momentum exchanges between the urban surface and the lower atmosphere. In terms of temperature, urbanization shows strong warming effects during summer and at night. Over the three urban agglomeration regions, we find a possible warming of 0.6–0.8°C in annual mean temperature by the 2050s caused by urbanization. Ren et al. (2008) estimated the trend of urban warming to be 0.11°C $(10\ yr)^{-1}$ in northern China based on 1960−2000 temperature observations. The magnitude of warming is slightly higher in our study because we focused on urban agglomeration regions. For the entire area of China, the annual mean surface air temperature will increase by 0.2°C by 2050. This temperature increase agrees with previously suggested urbanization-contributed warming rates (Zhou et al. 2004).

As discussed in section 4, urbanization has a comparable impact on historical climate as vegetation changes. For future climate, vegetation changes are projected to induce a significant annual surface temperature increase of 0.4°C in east Eurasia (Jiang et al. 2011).

Vegetation conversion from grassland to forestland in southeastern China may decrease annual mean temperatures by 0.11°C (Yu et al. 2013). In other regions in the world, Trail et al. (2013) found that reforestation of cropland in the southeastern U.S. tends to increase surface air temperature by 0.5°C, while deforestation tends to decrease surface air temperature by 0.5°C. The reported grassland degradation in Mongolia may lead to a warming (0.1–0.4°C) of annual mean temperature in the future (Zhang et al. 2013). In terms of the magnitude of future regional temperature changes, we find the effects of urbanization to be on par with those from vegetation changes. Therefore, urban forcing should be included in future climate simulations.

At local scales, future urbanization tends to increase summer temperature by as much as 2.7°C over urban areas. Previous studies have shown intensified heat stress—a leading cause of weather-related human mortality—as a result of urbanization and future climate change (Oleson et al. 2015). Therefore, the vulnerability and adaptation of urban populations need to be considered in future climate projection.

Precipitation changes show a more complex pattern than temperature. Urbanization tends to decrease atmospheric moisture as a result of decreased evapotranspiration, but increases PBL height by increasing the sensible heat flux. Feng et al. (2014) also found strengthened vertical motion due to urbanization. However, it did not result in increased precipitation because of the decreased surface moisture in urban areas. We did not see a consistent change in precipitation over China's three main urban agglomerations. Kaufmann et al. (2007) suggests that there is no causal relationship between urbanization and precipitation, because the East Asian monsoon plays a dominant effect in this region.

We did indeed find that urbanization may strengthen the summer monsoon, and slightly weaken the winter monsoon. Therefore, the impacts of urbanization on precipitation are due to the combined effects of both local moisture changes and large-scale circulation features.

Compared with the results for the present climate from section 4, the impacts of urbanization on future climate show a different magnitude. For example, the combined effects of vegetation changes and urbanization on historical temperature can be up to 1°C (Figure 4.4). However, further urbanization shows a greater warming effect, as much as 2°C (Figure 5.9). This could be due to using different land surface models in these two sets of experiments, as the parameterizations for energy exchanges between the urban surface and the atmosphere are different. Furthermore, the spatial resolutions differ for the historical and future simulations. In CESM (section 4), urban area only accounts for a small portion (less than 30%) of each grid cell. In the WRF model with its higher spatial resolution, urban area can be as much as 90% in some grid cells in eastern China. Therefore, the urban heating is likely higher in these regions in the regional climate model. Finally, climate change may increase the urban heat islands' effects on climate (Oleson 2011). Therefore, global warming in the RCP 4.5 scenario may strengthen the warming effects in urban areas compared to the present climate conditions.

Urban aerosol effects are another factor that can influence the regional climate during urbanization (Kaufmann et al. 2007). However, in this study we only focused on the biogeophysical effects of urbanization. Future work will also consider the aerosol impact of urbanization.

6. CONCLUSIONS

This study provided a comprehensive investigation of the impacts of land cover changes on climate in China. First, we evaluated the performance of state-of-the-art climate models in simulating temperature and precipitation in China. Based on our evaluation, a well-performing climate model (CESM) was used to explore the land-atmosphere interactions over China. We examined the biogeophysical impacts of historical vegetation changes and urbanization on climate in China. Also, the WRF model was used to dynamically downscale future CESM projections and estimate the impacts of possible urbanization on future climate.

6.1. Performance of CMIP5 over China

The performance of 20 CMIP5 GCMs was evaluated in their ability to simulate the variability of surface air temperature and precipitation over China during the 20th century with respect to observational datasets. The multimodel ensemble of CMIP5 models can well capture the spatial patterns of seasonal and annual mean temperatures, however, with substantial cold biases over the Tibetan Plateau, especially in the cold season. Models also reproduce the observed climatic warming over the 20th century with an accelerated warming in the second half of the 20th century. However, the seasonal and spatial patterns of temperature trends are not well simulated. Inter-model comparisons suggest that four CMIP5 models better simulate historical surface air temperature variability over China: MPI-ESM-LR, CanESM2, MIROC-ESM, and CCSM4. Based on three future climate

scenarios (RCP 2.6, RCP 4.5, and RCP 8.5), temperature in China is projected to increase by 1.7–5.7°C by the end of the 21st century, with larger warming over northern China and the Tibetan Plateau. In terms of precipitation, CMIP5 models well reproduce the spatial pattern of annual and seasonal precipitation over China during the 20th century, however with an overestimation in most regions of China, especially along the eastern edge of the Tibetan Plateau. An underestimation is found in summer precipitation over the southeast of China. There is a large variability among individual models, with the greatest uncertainties in simulating summer precipitation. In the 21st century, there is a general increasing trend in precipitation over all of China based on all the three emission scenarios. RCP 8.5 corresponds to the largest increases in precipitation over the 21st century. By the end of the 21st century, annual precipitation will significantly increase by 6–16% based on the lowest–highest emission scenarios, respectively. The greatest increase will occur over the Tibetan Plateau and the eastern part of China during summer, suggesting future changes in the East Asian Monsoon.

6.2. Impacts of Historical Land Cover Changes on Climate over China

Based on the model evaluation from objective 1 and the model code availability, CESM is selected to specifically investigate the biogeophysical effects of historical land cover changes over China. Using this general circulation model, both vegetation and urbanization changes were considered as land cover changes, and their impacts on climate in China were assessed separately and in combination. Results show that vegetation changes alone are able to alter the surface flux balance, therefore modifying regional

temperature. Summer temperature changes are regulated by evapotranspiration and clouds. This can decrease daily maximum temperature but increase daily minimum temperature, thereby decreasing the diurnal temperature range. Decreases in winter temperature over northern China are mainly influenced by surface albedo changes. Vegetation changes do not exhibit significant impacts on summer precipitation or the East Asian summer monsoon, but could strengthen the East Asian winter monsoon and decrease winter precipitation in southern China. Compared to impacts of vegetation changes, the combination of vegetation and urbanization changes show more significant and extensive impact on temperature and precipitation in China. Urban heating produces greatly increased minimum temperatures and shows a remarkable warming effect in southeastern China, especially in winter when it offsets the cooling effects from vegetation changes. When urbanization is included, land cover changes can influence the East Asian summer monsoon and are associated with a significant southern increase and northern decrease pattern based on summer precipitation changes. Also, with the combined urbanization and vegetation changes, the East Asian winter monsoon is actually weakened, and exceeds the effects from vegetation changes. Therefore, we conclude that urbanization should be included in model simulations to provide realistic and complete climatic impacts of land cover changes.

6.3. Impacts of Urbanization on Future Climate over China

The regional climate model WRF was used to estimate the impacts of possible urbanization on future climate in China. WRF shows good performance in downscaling

CESM output, however, with large biases over the Tibetan Plateau; this high-altitude region is therefore excluded from subsequent analyses. Urban expansion shows strong impacts on the surface energy balance due to low albedo and the thermal properties of urban surface. Over urban areas, the decrease in latent heat flux and increase in sensible heat flux lead to higher surface air temperature and less humidity in the atmosphere. Larger urban warming effects are found during night and in summer, which can be attributed to the high heat capacity of urban areas. Urbanization does not exert a significant impact on the overall future temperature trend in China. However, at regional and local/urban scales, urbanization shows strong warming effects of up to 1.9°C, which is comparable to the greenhouse effects under RCP 4.5 scenarios. The impacts of urbanization on precipitation show a combined effect from changes in both local moisture and the large-scale atmospheric circulation. There is a decrease in atmospheric moisture over urban areas. The East Asian summer monsoon is strengthened in southern China, but the East winter monsoon is slightly weakened in the Yangtze River Delta.

6.4. Overall Contributions

The robustness of future climate projections and model-based land-atmosphere interactions relies strongly on the performance of climate models. This dissertation is the first to evaluate the performance of CMIP5 GCMs in simulating climate in China, and analyze future climate projections under three scenarios. The results provide useful information for future climate-related studies, in that they outline the limitations of current climate models, recommend which model has a better ability to capture the climate

variability over China, and describe how temperature and precipitation will change in future.

The biogeophysical feedbacks of land cover changes are an essential part in land-atmosphere interaction studies. This investigation is the first to compare the impacts of both major types of historical land cover changes—vegetation changes and urbanization—on climate in China. We found that the effects of urbanization have a comparable magnitude and impact on climate as vegetation changes; however, urbanization is usually not considered in the climate modeling of land cover changes. Our results may benefit future climate modeling design, especially for the upcoming CMIP6 experimental design.

This study is also the first to investigate how urbanization influences future climate in China. Even though further urbanization in China does not exhibit significant warming at the larger scale, its strong warming effects at the local scale are as strong as those from greenhouse gas forcing under the RCP 4.5 scenario, indicating a higher risk of heat stress for increased urban populations. Our results are informative for decision makers in climate change adaptation and mitigation in China. Furthermore, the possible impacts of urbanization on summer precipitation in China may benefit water management confronting future climate changes.

6.5. Future Work

The limitation of GMCs in simulating climate at regional scale has been discussed in section 2 and 3. The WRF model has demonstrated its ability to reasonably downscale GCM output (section 5). Therefore, my future work will continue to focus on the

dynamical downscaling of long-term climate projections in China under various scenarios, so that we will have a better understanding of future climate changes in China.

Further urbanization is not the only possible land cover change in China's future. China has the largest afforested area in the world (Peng et al. 2014). In our current study, we only focus on the historical deforestation and its impacts on climate (section 4). China's policy of returning farmland to forests will promote further afforestation, which has a large potential to influence regional climate. Therefore, an improved understanding of the impacts of afforestation on future climate is needed.

REFERENCES

Abramowitz, G., R. Leuning, M. Clark, and A. Pitman, 2008: Evaluating the performance of land surface models. *J. Clim.*, **21,** 5468-5481, doi:10.1175/2008JCLI2378.1.

Alkama, R., L. Marchand, A. Ribes, and B. Decharme, 2013: Detection of global runoff changes: results from observations and CMIP5 experiments. *Hydrol. Earth Syst. Sci.*, **17,** 2967-2979, doi:10.5194/hess-17-2967-2013.

Anav, A., P. M. Ruti, V. Artale, and R. Valentini, 2010: Modelling the effects of land-cover changes on surface climate in the Mediterranean region. *Clim. Res.*, **41,** 91-104, doi:10.3354/cr00841.

Anderson-Teixeira, K. J., P. K. Snyder, T. E. Twine, S. V. Cuadra, M. H. Costa, and E. H. DeLucia, 2012: Climate-regulation services of natural and agricultural ecoregions of the Americas. *Nature Clim. Change*, **2,** 177-181, doi:10.1038/nclimate1346.

Annan, J. D., D. J. Lunt, J. C. Hargreaves, and P. J. Valdes, 2005: Parameter estimation in an atmospheric GCM using the Ensemble Kalman Filter. *Nonlin. Processes Geophys.*, **12,** 363-371, doi:10.5194/npg-12-363-2005.

Barriopedro, D., C. M. Gouveia, R. M. Trigo, and L. Wang, 2012: The 2009/10 Drought in China: possible causes and impacts on vegetation. *J. Hydrometeorol.*, **13,** 1251-1267, doi:10.1175/JHM-D-11-074.1.

Betts, R. A., P. D. Falloon, K. K. Goldewijk, and N. Ramankutty, 2007: Biogeophysical effects of land use on climate: Model simulations of radiative forcing and large-

scale temperature change. *Agric. For. Meteorol.*, **142,** 216-233, doi:10.1016/j.agrformet.2006.08.021.

Biasutti, M., 2013: Forced Sahel rainfall trends in the CMIP5 archive. *J. Geophys. Res. Atmos.*, **118,** 1613-1623, doi:10.1002/jgrd.50206.

Boisier, J. P., N. de Noblet-Ducoudré, and P. Ciais, 2013: Inferring past land use-induced changes in surface albedo from satellite observations: a useful tool to evaluate model simulations. *Biogeosciences*, **10,** 1501-1516, doi:10.5194/bg-10-1501-2013.

Bonan, G., 1997: Effects of land use on the climate of the United States. *Clim. Change*, **37,** 449-486, doi:10.1023/A:1005305708775.

Bonan, G. B., 2008: Forests and climate change: Forcings, feedbacks, and the climate benefits of forests. *Science*, **320,** 1444-1449, doi:10.1126/science.1155121.

Brovkin, V., L. Boysen, V. K. Arora, J. P. Boisier, P. Cadule, et al., 2013: Effect of anthropogenic land-use and land-cover changes on climate and land carbon storage in CMIP5 projections for the twenty-first century. *J. Clim.*, **26,** 6859-6881, doi:10.1175/JCLI-D-12-00623.1.

Bruyère, C., J. Done, G. Holland, and S. Fredrick, 2014: Bias corrections of global models for regional climate simulations of high-impact weather. *Clim. Dyn.*, **43,** 1847-1856, doi:10.1007/s00382-013-2011-6.

Chang, C.-P., 2004: *East Asian Monsoon.* World Scientific Press, Singapore, 572 pp.

Chase, T. N., R. A. Pielke Sr, T. G. F. Kittel, R. R. Nemani, and S. W. Running, 2000: Simulated impacts of historical land cover changes on global climate in northern winter. *Clim. Dyn.*, **16,** 93-105, doi:10.1007/s003820050007.

Chase, T. N., R. A. Pielke, T. G. F. Kittel, M. Zhao, A. J. Pitman, S. W. Running, and R. R. Nemani, 2001: Relative climatic effects of landcover change and elevated carbon dioxide combined with aerosols: A comparison of model results and observations. *J. Geophys. Res. Atmos.*, **106,** 31685-31691, doi:10.1029/2000JD 000129.

Chen, F., and J. Dudhia, 2001: Coupling an advanced land surface–hydrology model with the Penn State–NCAR MM5 modeling system. part I: model implementation and sensitivity. *Mon. Wea. Rev.*, **129,** 569-585, doi:10.1175/1520-0493(2001)129 <0569:CAALSH>2.0.CO;2.

Chen, H., and J. Sun, 2009: How the "best" models project the future precipitation change in China. *Adv. Atmos. Sci.*, **26,** 773-782, doi:10.1007/s00376-009-8211-7.

Chen, H., and Y. Zhang, 2013: Sensitivity experiments of impacts of large-scale urbanization in East China on East Asian winter monsoon. *Chin. Sci. Bull.*, **58,** 809-815, doi:10.1007/s11434-012-5579-z.

Chen, H., T. Zhou, R. B. Neale, X. Wu, and G. J. Zhang, 2010: Performance of the new NCAR CAM3.5 in East Asian summer monsoon simulations: sensitivity to modifications of the convection scheme. *J. Clim.*, **23,** 3657-3675, doi:10.1175/ 2010JCLI3022.1.

Chen, L., and O. W. Frauenfeld, 2014a: A comprehensive evaluation of precipitation simulations over China based on CMIP5 multimodel ensemble projections. *J. Geophys. Res. Atmos.*, **119,** 5767–5786, doi:10.1002/2013JD021190.

——, 2014b: Surface Air temperature changes over the 20th and 21st centuries in China simulated by 20 CMIP5 models. *J. Clim.*, **27,** 3920-3937, doi:10.1175/JCLI-D-13-00465.1.

Chen, W., Z. Jiang, and L. Li, 2011: Probabilistic projections of climate change over China under the SRES A1B scenario using 28 AOGCMs. *J. Clim.*, **24,** 4741-4756, doi:10.1175/2011JCLI4102.1.

Cho, M.-H., K.-O. Boo, J. Lee, C. Cho, and G.-H. Lim, 2014: Regional climate response to land surface changes after harvest in the North China Plain under present and possible future climate conditions. *J. Geophys. Res. Atmos.*, **119,** 4507-4520, doi:10.1002/2013JD020111.

Claussen, M., V. Brovkin, and A. Ganopolski, 2001: Biogeophysical versus biogeochemical feedbacks of large-scale land cover change. *Geophys. Res. Lett.*, **28,** 1011-1014, doi:10.1029/2000GL012471.

Comarazamy, D. E., J. E. González, J. C. Luvall, D. L. Rickman, and R. D. Bornstein, 2013: Climate impacts of land-cover and land-use changes in tropical islands under conditions of global climate change. *J. Clim.*, **26,** 1535-1550, doi:10.1175/JCLI-D-12-00087.1.

Davin, E. L., and N. de Noblet-Ducoudré, 2010: Climatic impact of global-scale deforestation: radiative versus nonradiative processes. *J. Clim.*, **23,** 97-112, doi:10.1175/2009JCLI3102.1.

Davin, E. L., N. de Noblet-Ducoudré, and P. Friedlingstein, 2007: Impact of land cover change on surface climate: Relevance of the radiative forcing concept. *Geophys. Res. Lett.*, **34,** L13702, doi:10.1029/2007GL029678.

de Noblet-Ducoudré, N., J.-P. Boisier, A. Pitman, G. B. Bonan, V. Brovkin, et al., 2012: Determining robust impacts of land-use-induced land cover changes on surface climate over North America and Eurasia: results from the first set of LUCID experiments. *J. Clim.*, **25,** 3261-3281, doi:10.1175/JCLI-D-11-00338.1.

Dee, D. P., S. M. Uppala, A. J. Simmons, P. Berrisford, P. Poli, et al., 2011: The ERA-Interim reanalysis: configuration and performance of the data assimilation system. *Q. J. Roy. Meteorol. Soc.*, **137,** 553-597, doi:10.1002/qj.828.

Di Vittorio, A. V., L. P. Chini, B. Bond-Lamberty, J. Mao, X. Shi, et al., 2014: From land use to land cover: restoring the afforestation signal in a coupled integrated assessment–earth system model and the implications for CMIP5 RCP simulations. *Biogeosciences*, **11,** 6435-6450, doi:10.5194/bg-11-6435-2014.

Ding, Y., and J. C. L. Chan, 2005: The East Asian summer monsoon: an overview. *Meteorol. Atmos. Phys.*, **89,** 117-142, doi:10.1007/s00703-005-0125-z

Ding, Y., Z. Wang, and Y. Sun, 2008: Inter-decadal variation of the summer precipitation in East China and its association with decreasing Asian summer monsoon. Part I: Observed evidences. *Int. J. Climatol.*, **28,** 1139-1161, doi:10.1002/joc.1615.

Ding, Y., G. Ren, Z. Zhao, Y. Xu, Y. Luo, Q. Li, and J. Zhang, 2007: Detection, causes and projection of climate change over China: An overview of recent progress. *Adv. Atmos. Sci.*, **24,** 954-971, doi:10.1007/s00376-007-0954-4.

Dirmeyer, P. A., D. Niyogi, N. de Noblet-Ducoudré, R. E. Dickinson, and P. K. Snyder, 2010: Impacts of land use change on climate. *Int. J. Climatol.*, **30,** 1905-1907, doi:10.1002/joc.2157.

Dudhia, J., 1989: Numerical study of convection observed during the winter monsoon experiment using a mesoscale two-dimensional model. *J. Atmos. Sci.*, **46,** 3077-3107, doi:10.1175/1520-0469(1989)046<3077:NSOCOD>2.0.CO;2.

Eden, J. M., M. Widmann, D. Grawe, and S. Rast, 2012: Skill, correction, and downscaling of GCM-simulated precipitation. *J. Clim.*, **25,** 3970-3984, doi:10.1175/JCLI-D-11-00254.1.

Fall, S., D. Niyogi, A. Gluhovsky, R. A. Pielke, E. Kalnay, and G. Rochon, 2010: Impacts of land use land cover on temperature trends over the continental United States: assessment using the North American Regional Reanalysis. *Int. J. Climatol.*, **30,** 1980-1993, doi:10.1002/joc.1996.

Fan, Y., and H. van den Dool, 2008: A global monthly land surface air temperature analysis for 1948–present. *J. Geophys. Res. Atmos.*, **113,** D01103, doi:10.1029/2007JD008470.

Feddema, J., K. Oleson, G. Bonan, L. Mearns, W. Washington, G. Meehl, and D. Nychka, 2005a: A comparison of a GCM response to historical anthropogenic land cover change and model sensitivity to uncertainty in present-day land cover representations. *Clim. Dyn.*, **25,** 581-609, doi:10.1007/s00382-005-0038-z.

Feddema, J. J., K. W. Oleson, G. B. Bonan, L. O. Mearns, L. E. Buja, G. A. Meehl, and W. M. Washington, 2005b: The importance of land-cover change in simulating future climates. *Science*, **310,** 1674-1678, doi:10.1126/science.1118160.

Feng, J.-M., Y.-L. Wang, and Z.-G. Ma, 2013: Long-term simulation of large-scale urbanization effect on the East Asian monsoon. *Clim. Change*, 1-13, doi:10.1007/s10584-013-0885-2.

Feng, J.-M., Y.-L. Wang, Z.-G. Ma, and Y.-H. Liu, 2012: Simulating the regional impacts of urbanization and anthropogenic heat release on climate across China. *J. Clim.*, **25,** 7187-7203, doi:10.1175/JCLI-D-11-00333.1.

Feng, J., J. Wang, and Z. Yan, 2014: Impact of anthropogenic heat release on regional climate in three vast urban agglomerations in China. *Adv. Atmos. Sci.*, **31,** 363-373, doi:10.1007/s00376-013-3041-z.

Feng, L., T. Zhou, B. Wu, T. Li, and J.-J. Luo, 2011: Projection of future precipitation change over China with a high-resolution global atmospheric model. *Adv. Atmos. Sci.*, **28,** 464-476, doi:10.1007/s00376-010-0016-1.

Flato, G., J. Marotzke, B. Abiodun, P. Braconnot, S.C. Chou, et al., 2013: Evaluation of climate models. In: Climate Change 2013: The Physical Science Basis. *Contribution of Working Group I to the Fifth Assessment Report of the Intergovernmental Panel on Climate Change*, T.F. Stocker, D. Qin, G.-K. Plattner, M. Tignor, S.K. Allen, et al., Eds., Cambridge University Press, Cambridge, United Kingdom and New York, NY, USA, 741–866.

Foley, J. A., R. DeFries, G. P. Asner, C. Barford, G. Bonan, et al., 2005: Global consequences of land use. *Science*, **309,** 570-574, doi:10.1126/science.1111772.

Fu, C., 2003: Potential impacts of human-induced land cover change on East Asia monsoon. *Glob. Planet. Change*, **37,** 219-229, doi:10.1016/S0921-8181(02) 00207-2.

Gao, H., and S. Yang, 2009: A severe drought event in northern China in winter 2008–2009 and the possible influences of La Niña and Tibetan Plateau. *J. Geophys. Res. Atmos.*, **114,** D24104, doi:10.1029/2009JD012430.

Gao, J., V. Masson-Delmotte, T. Yao, L. Tian, C. Risi, and G. Hoffmann, 2010: Precipitation water stable isotopes in the south Tibetan Plateau: observations and modeling*. *J. Clim.*, **24,** 3161-3178, doi:10.1175/2010JCLI3736.1.

Gao, X., Y. Shi, and F. Giorgi, 2011: A high resolution simulation of climate change over China. *Sci. China Earth Sci.*, **54,** 462-472, doi:10.1007/s11430-010-4035-7.

Gao, X., Y. Shi, D. Zhang, and F. Giorgi, 2012: Climate change in China in the 21st century as simulated by a high resolution regional climate model. *Chin. Sci. Bull.*, **57,** 1188-1195, doi:10.1007/s11434-011-4935-8.

Gao, X., Y. Luo, W. Lin, Z. Zhao, and F. Giorgi, 2003: Simulation of effects of land use change on climate in China by a regional climate model. *Adv. Atmos. Sci.*, **20,** 583-592, doi:10.1007/BF02915501.

Gao, X., Y. Shi, R. Song, F. Giorgi, Y. Wang, and D. Zhang, 2008: Reduction of future monsoon precipitation over China: comparison between a high resolution RCM

simulation and the driving GCM. *Meteorol. Atmos. Phys.*, **100,** 73-86, doi:10.1007/s00703-008-0296-5.

Gao, Y., J. Xu, and D. Chen, 2015: Evaluation of WRF mesoscale climate simulations over the Tibetan Plateau during 1979-2011. *J. Clim.*, **28,** 2823–2841, doi:10.1175/JCLI-D-14-00300.1.

Gibbard, S., K. Caldeira, G. Bala, T. J. Phillips, and M. Wickett, 2005: Climate effects of global land cover change. *Geophys. Res. Lett.*, **32,** L23705, doi:10.1029/2005GL024550.

Giorgi, F., X. Bi, and J. S. Pal, 2004: Mean, interannual variability and trends in a regional climate change experiment over Europe. I. Present-day climate (1961–1990). *Clim. Dyn.*, **22,** 733-756, doi:10.1007/s00382-004-0409-x.

Gong, D., and S. Wang, 1999: 1998: The warmest year on record of the century in China (in Chinese). *Meteorol. Mon.*, **25,** 3-5, doi: 10.3969/j.issn.1000-0526.1999.08.001.

Gong, H., L. Wang, W. Chen, R. Wu, K. Wei, and X. Cui, 2013: The climatology and interannual variability of the East Asian winter monsoon in CMIP5 models. *J. Clim.*, **27,** 1659-1678, doi:10.1175/JCLI-D-13-00039.1.

Gong, P., S. Liang, E. J. Carlton, Q. Jiang, J. Wu, L. Wang, and J. V. Remais, 2012: Urbanisation and health in China. *The Lancet*, **379,** 843-852, doi:10.1016/S0140-6736(11)61878-3.

Grimm, N. B., S. H. Faeth, N. E. Golubiewski, C. L. Redman, J. Wu, X. Bai, and J. M. Briggs, 2008: Global change and the ecology of cities. *Science*, **319,** 756-760, doi:10.1126/science.1150195.

Gu, W., W. Li, L. Chen, and X. Jia, 2012: Interannual variations of autumn precipitation in China and their relations to the distribution of tropical Pacific sea surface temperature (in Chinese). *Clim. Environ. Res.*, **17,** 467-480, doi:10.3878/ j.issn.1006-9585.2011.10164.

Güneralp, B., İ. Güneralp, and Y. Liu, 2015: Changing global patterns of urban exposure to flood and drought hazards. *Glob. Environ. Change*, **31,** 217-225, doi:10.1016/j.gloenvcha.2015.01.002.

Harris, I., P. D. Jones, T. J. Osborn, and D. H. Lister, 2014: Updated high-resolution grids of monthly climatic observations – the CRU TS3.10 Dataset. *Int. J. Climatol.*, **34,** 623-642, doi:10.1002/joc.3711.

Hirota, N., and Y. Takayabu, 2013: Reproducibility of precipitation distribution over the tropical oceans in CMIP5 multi-climate models compared to CMIP3. *Clim. Dyn.*, **41,** 2909-2920, doi:10.1007/s00382-013-1839-0.

Hong, S.-Y., J. Dudhia, and S.-H. Chen, 2004: A revised approach to ice microphysical processes for the bulk parameterization of clouds and precipitation. *Mon. Wea. Rev.*, **132,** 103-120, doi:10.1175/1520-0493(2004)132<0103:ARATIM> 2.0.CO;2.

Hong, S.-Y., Y. Noh, and J. Dudhia, 2006: A new vertical diffusion package with an explicit treatment of entrainment processes. *Mon. Wea. Rev.*, **134,** 2318-2341, doi:10.1175/MWR3199.1.

Hsu, P.-c., T. Li, H. Murakami, and A. Kitoh, 2013: Future change of the global monsoon revealed from 19 CMIP5 models. *J. Geophys. Res. Atmos.*, **118,** 1247-1260, doi:10.1002/jgrd.50145.

Hu, Y., X.-Z. Zhang, R. Mao, D.-Y. Gong, H.-b. Liu, and J. Yang, 2014: Modeled responses of summer climate to realistic land use/cover changes from the 1980s to the 2000s over eastern China. *J. Geophys. Res. Atmos.*, **120,** 167-179, doi:10.1002/2014JD022288.

Hu, Z.-Z., S. Yang, and R. Wu, 2003: Long-term climate variations in China and global warming signals. *J. Geophys. Res. Atmos.*, **108,** 4614, doi:10.1029/2003JD003651.

Hua, L. J., Z. G. Ma, and W. D. Guo, 2008: The impact of urbanization on air temperature across China. *Theor. Appl. Climatol.*, **93,** 179-194, doi:10.1007/s00704-007-0339-8.

Hua, W., H. Chen, and S. Sun, 2013: Uncertainty in land surface temperature simulation over China by CMIP3/CMIP5 models. *Theor. Appl. Climatol.*, **117,** 463-474, doi:10.1007/s00704-013-1020-z.

Hua, W. J., and H. S. Chen, 2013: Recognition of climatic effects of land use/land cover change under global warming. *Chin. Sci. Bull.*, **58,** 3852-3858, doi:10.1007/s11434-013-5902-3.

Huang, D.-Q., J. Zhu, Y.-C. Zhang, and A.-N. Huang, 2013: Uncertainties on the simulated summer precipitation over Eastern China from the CMIP5 models. *J. Geophys. Res. Atmos.*, **118,** 9035-9047, doi:10.1002/jgrd.50695.

Huang, R. H., J. L. Chen, L. Wang, and Z. D. Lin, 2012: Characteristics, processes, and causes of the spatio-temporal variabilities of the East Asian monsoon system. *Adv. Atmos. Sci.*, **29,** 910-942, doi:10.1007/s00376-012-2015-x.

Huszar, P., T. Halenka, M. Belda, M. Zak, K. Sindelarova, and J. Miksovsky, 2014: Regional climate model assessment of the urban land-surface forcing over central Europe. *Atmos. Chem. Phys.*, **14,** 12393-12413, doi:10.5194/acp-14-12393-2014.

Ichinose, T., K. Shimodozono, and K. Hanaki, 1999: Impact of anthropogenic heat on urban climate in Tokyo. *Atmos. Environ.*, **33,** 3897-3909, doi:10.1016/S1352-2310(99)00132-6.

IPCC, 2007: Climate Change 2007: The Physical Science Basis. *The Fourth Assessment Report of the Intergovernmental Panel on Climate Change*, S. Solomon, D. Qin, M. Manning, Z. Chen, M. Marquis, et al., Eds., Cambridge University Press, Cambridge, United Kingdom and New York, NY, USA, 996 pp.

——, 2013: Climate Change 2013: The Physical Science Basis. *The Fifth Assessment Report of the Intergovernmental Panel on Climate Change*, T.F. Stocker, D. Qin, G.-K. Plattner, M. Tignor, S.K. Allen, et al., Eds., Cambridge University Press, Cambridge, United Kingdom and New York, NY, USA, 1535 pp.

Islam, S., Y. Tang, and P. Jackson, 2013: Asian monsoon simulations by Community Climate Models CAM4 and CCSM4. *Clim. Dyn.*, **41,** 2617-2642, doi:10.1007/s00382-013-1752-6.

Jacob, D., L. Bärring, O. Christensen, J. Christensen, M. Castro, et al., 2007: An inter-comparison of regional climate models for Europe: model performance in present-day climate. *Clim. Change*, **81,** 31-52, doi:10.1007/s10584-006-9213-4.

Ji, Z., and S. Kang, 2012: Double-nested Dynamical downscaling experiments over the Tibetan Plateau and their projection of climate change under two RCP scenarios. *J. Atmos. Sci.*, **70,** 1278-1290, doi:10.1175/JAS-D-12-0155.1.

Jiang, D. B., Y. Zhang, and X. M. Lang, 2011: Vegetation feedback under future global warming. *Theor. Appl. Climatol.*, **106,** 211-227, doi:10.1007/s00704-011-0428-6.

Jones, P. D., D. H. Lister, and Q. Li, 2008: Urbanization effects in large-scale temperature records, with an emphasis on China. *J. Geophys. Res. Atmos.*, **113,** D16122, doi:10.1029/2008JD009916.

Kain, J. S., 2004: The Kain–Fritsch convective parameterization: an update. *J. Appl. Meteorol.*, **43,** 170-181, doi:10.1175/1520-0450(2004)043<0170:TKCPAU> 2.0.CO;2.

Kalnay, E., and M. Cai, 2003: Impact of urbanization and land-use change on climate. *Nature*, **423,** 528-531, doi:10.1038/nature01675.

Kaufmann, R. K., K. C. Seto, A. Schneider, Z. Liu, L. Zhou, and W. Wang, 2007: Climate response to rapid urban growth: evidence of a human-induced precipitation deficit. *J. Clim.*, **20,** 2299-2306, doi:10.1175/JCLI4109.1.

Kharin, V. V., F. W. Zwiers, X. Zhang, and G. C. Hegerl, 2007: Changes in temperature and precipitation extremes in the IPCC ensemble of global coupled model simulations. *J. Clim.*, **20,** 1419-1444, doi:10.1175/JCLI4066.1.

Kim, Y., and G. Wang, 2007: Impact of initial soil moisture anomalies on subsequent precipitation over North America in the coupled land–atmosphere model CAM3–CLM3. *J. Hydrometeorol.*, **8,** 513-533, doi:10.1175/JHM611.1.

Kitoh, A., H. Endo, K. Krishna Kumar, I. F. A. Cavalcanti, P. Goswami, and T. Zhou, 2013: Monsoons in a changing world: A regional perspective in a global context. *J. Geophys. Res. Atmos.*, **118,** 3053-3065, doi:10.1002/jgrd.50258.

Knutti, R., and J. Sedlacek, 2013: Robustness and uncertainties in the new CMIP5 climate model projections. *Nature Clim. Change*, **3,** 369-373, doi:10.1038/nclimate1716.

Kripalani, R. H., J. H. Oh, and H. S. Chaudhari, 2007: Response of the East Asian summer monsoon to doubled atmospheric CO2: Coupled climate model simulations and projections under IPCC AR4. *Theor. Appl. Climatol.*, **87,** 1-28, doi:10.1007/s00704-006-0238-4.

Kumar, S., V. Merwade, J. L. Kinter, and D. Niyogi, 2013a: Evaluation of temperature and precipitation trends and long-term persistence in CMIP5 20th century climate simulations. *J. Clim.*, **26,** 4168–4185, doi:10.1175/JCLI-D-12-00259.1.

Kumar, S., P. A. Dirmeyer, V. Merwade, T. DelSole, J. M. Adams, and D. Niyogi, 2013b: Land use/cover change impacts in CMIP5 climate simulations: A new methodology and 21st century challenges. *J. Geophys. Res. Atmos.*, **118,** 6337-6353, doi:10.1002/jgrd.50463.

Kumar, S., P. A. Dirmeyer, D. M. Lawrence, T. DelSole, E. L. Altshuler, et al., 2014: Effects of realistic land surface initializations on subseasonal to seasonal soil moisture and temperature predictability in North America and in changing climate simulated by CCSM4. *J. Geophys. Res. Atmos.*, **119,** 13,250-213,270, doi:10.1002/2014JD022110.

Kusaka, H., and F. Kimura, 2004: Coupling a single-layer urban canopy model with a simple atmospheric model: impact on urban heat island simulation for an idealized case. *J. Meteorol. Soc. Jpn. Ser. II*, **82,** 67-80, doi:10.2151/jmsj.82.67.

Kusaka, H., H. Kondo, Y. Kikegawa, and F. Kimura, 2001: A simple single-layer urban canopy model for atmospheric models: comparison with multi-layer and slab models. *Bound.-Layer Meteor.*, **101,** 329-358, doi:10.1023/A:1019207923078.

Lawrence, D., K. W. Oleson, M. G. Flanner, P. E. Thorton, S. C. Swenson, et al., 2011: Parameterization improvements and functional and structural advances in version 4 of the Community Land Model. *J. Adv. Model. Earth Syst.*, **3,** M03001, doi:10.1029/2011ms000045.

Lawrence, P. J., and T. N. Chase, 2010: Investigating the climate impacts of global land cover change in the community climate system model. *Int. J. Climatol.*, **30,** 2066-2087, doi:10.1002/joc.2061.

Lawrence, P. J., J. J. Feddema, G. B. Bonan, G. A. Meehl, B. C. O'Neill, et al., 2012: Simulating the biogeochemical and biogeophysical impacts of transient land cover change and wood harvest in the Community Climate System Model (CCSM4) from 1850 to 2100. *J. Clim.*, **25,** 3071-3095, doi:10.1175/JCLI-D-11-00256.1.

Lee, J.-E., B. R. Lintner, C. K. Boyce, and P. J. Lawrence, 2011: Land use change exacerbates tropical South American drought by sea surface temperature variability. *Geophys. Res. Lett.*, **38,** L19706, doi:10.1029/2011GL049066.

Legates, D. R., and C. J. Willmott, 1990a: Mean seasonal and spatial variability in global surface air temperature. *Theor. Appl. Climatol.*, **41,** 11-21, 10.1007/BF00866198.

Legates, D. R., and C. J. Willmott, 1990b: Mean seasonal and spatial variability in gauge-corrected, global precipitation. *Int. J. Climatol.*, **10,** 111-127, doi:10.1002/joc.3370100202.

Li, H., L. Feng, and T. Zhou, 2011: Multi-model projection of July–August climate extreme changes over China under CO2 doubling. Part II: Temperature. *Adv. Atmos. Sci.*, **28,** 448-463, doi:10.1007/s00376-010-0052-x.

Li, H., A. Dai, T. Zhou, and J. Lu, 2010: Responses of East Asian summer monsoon to historical SST and atmospheric forcing during 1950–2000. *Clim. Dyn.*, **34,** 501-514, doi:10.1007/s00382-008-0482-7.

Li, Q., H. Zhang, X. Liu, and J. Huang, 2004: Urban heat island effect on annual mean temperature during the last 50 years in China. *Theor. Appl. Climatol.*, **79,** 165-174, doi:10.1007/s00704-004-0065-4.

Li, Y., L. Zhu, X. Zhao, S. Li, and Y. Yan, 2013a: Urbanization impact on temperature change in China with emphasis on land cover change and human activity. *J. Clim.*, **26,** 8765-8780, doi:10.1175/JCLI-D-12-00698.1.

Li, Y. F., Z. H. Li, Z. H. Li, X. L. Geng, and X. Z. Deng, 2013b: Numerical simulation of the effects of grassland degradation on the surface climate in overgrazing area of northwest China. *Adv. Meteorol.*, 270192, doi:10.1155/2013/270192.

Li, Z., T. Zhou, H. Chen, D. Ni, and R.-H. Zhang, 2014: Modelling the effect of soil moisture variability on summer precipitation variability over East Asia. *Int. J. Climatol.,* **35,** 879-887, doi:10.1002/joc.4023.

Liao, J., T. Wang, X. Wang, M. Xie, Z. Jiang, X. Huang, and J. Zhu, 2014: Impacts of different urban canopy schemes in WRF/Chem on regional climate and air quality in Yangtze River Delta, China. *Atmos. Res.*, **145–146,** 226-243, doi:10.1016/ j.atmosres.2014.04.005.

Liu, M., and H. Tian, 2010: China's land cover and land use change from 1700 to 2005: Estimations from high-resolution satellite data and historical archives. *Glob. Biogeochem. Cycles*, **24,** GB3003, doi:10.1029/2009GB003687.

Liu, S., W. Gao, and X.-Z. Liang, 2013: A regional climate model downscaling projection of China future climate change. *Clim. Dyn.*, **41,** 1871-1884, doi:10.1007/s00382-012-1632-5.

Loveland, T. R., and R. Mahmood, 2014: A design for a sustained assessment of climate forcing and feedbacks related to land use and land cover change. *Bull. Am. Meteorol. Soc.*, **95,** 1563-1572, doi:10.1175/BAMS-D-12-00208.1.

Mahmood, R., K. G. Hubbard, and C. Carlson, 2004: Modification of growing-season surface temperature records in the northern great plains due to land-use transformation: verification of modelling results and implication for global climate change. *Int. J. Climatol.*, **24,** 311-327, doi:10.1002/joc.992.

Mahmood, R., Mahmood, R., R. A. Pielke, K. G. Hubbard, D. Niyogi, P. A. Dirmeyer, et al., 2014: Land cover changes and their biogeophysical effects on climate. *Int. J. Climatol.*, **34,** 929-953, doi:10.1002/joc.3736.

Meehl, G. A., Meehl, G. A., C. Covey, K. E. Taylor, T. Delworth, R. J. Stouffer, et al., 2007: The WCRP CMIP3 multimodel dataset: a new era in climate change research. *Bull. Am. Meteorol. Soc.*, **88,** 1383-1394, doi:10.1175/ BAMS-88-9-1383.

Meng, L., and S. M. Quiring, 2010: Examining the influence of spring soil moisture anomalies on summer precipitation in the U.S. Great Plains using the Community Atmosphere Model version 3. *J. Geophys. Res. Atmos.*, **115,** D21118, doi:10.1029/ 2010JD014449.

Miao, C., Q. Duan, L. Yang, and A. G. L. Borthwick, 2012: On the applicability of temperature and precipitation data from CMIP3 for China. *PLoS ONE*, **7,** e44659, doi:10.1371/journal.pone.0044659.

Miao, S., F. Chen, M. A. LeMone, M. Tewari, Q. Li, and Y. Wang, 2009: An observational and modeling study of characteristics of urban heat island and boundary layer structures in Beijing. *J. Appl. Meteor. Climatol.*, **48,** 484-501, doi:10.1175/ 2008JAMC1909.1.

Mlawer, E. J., S. J. Taubman, P. D. Brown, M. J. Iacono, and S. A. Clough, 1997: Radiative transfer for inhomogeneous atmospheres: RRTM, a validated correlated-k model for the longwave. *J. Geophys. Res. Atmos.*, **102,** 16663-16682, doi:10.1029/97JD00237.

Monaghan, A. J., D. F. Steinhoff, C. L. Bruyere, and D. Yates, 2014: NCAR CESM Global Bias-Corrected CMIP5 Output to Support WRF/MPAS Research. Research Data Archive at the National Center for Atmospheric Research, Computational and

Information Systems Laboratory, Boulder, CO. [Available online at http://dx.doi.org/10.5065/D6DJ5CN4.] Accessed 20 Dec 2014.

Myoung, B., Y. S. Choi, S. J. Choi, and S. K. Park, 2012: Impact of vegetation on land-atmosphere coupling strength and its implication for desertification mitigation over East Asia. *J. Geophys. Res. Atmos.*, **117**, doi:10.1029/2011jd017143.

Neale, R. B., C.-C. Chen, A. Gettelman, P. H. Lauritzen, S. Park, et al., 2010: Description of the NCAR community atmosphere model (CAM 4.0). NCAR Tech. Note NCAR/TN-485+ STR, 212 pp.

Niyogi, D., P. Pyle, M. Lei, S. P. Arya, C. M. Kishtawal, et al., 2010: Urban modification of thunderstorms: an observational storm climatology and model case study for the Indianapolis urban region*. *J. Appl. Meteor. Climatol.*, **50,** 1129-1144, doi:10.1175/2010JAMC1836.1.

Notaro, M., G. Chen, and Z. Liu, 2011: Vegetation feedbacks to climate in the global monsoon regions*. *J. Clim.*, **24,** 5740-5756, doi:10.1175/2011JCLI4237.1.

Oke, T. R., 1982: The energetic basis of the urban heat island. *Q. J. Roy. Meteorol. Soc.*, **108,** 1-24, doi:10.1002/qj.49710845502.

Oleson, K., 2011: Contrasts between urban and rural climate in CCSM4 CMIP5 climate change scenarios. *J. Clim.*, **25,** 1390-1412, doi:10.1175/JCLI-D-11-00098.1.

Oleson, K. W., G. B. Bonan, J. Feddema, M. Vertenstein, and C. S. B. Grimmond, 2008: An urban parameterization for a global climate model. Part I: formulation and evaluation for two Cities. *J. Appl. Meteor. Climatol.*, **47,** 1038-1060, doi:10.1175/2007JAMC1597.1.

Oleson, K. W., A. Monaghan, O. Wilhelmi, M. Barlage, N. Brunsell, et al., 2015: Interactions between urbanization, heat stress, and climate change. *Clim. Change*, **129,** 525-541, doi:10.1007/s10584-013-0936-8.

Peng, S.-S., S. Piao, Z. Zeng, P. Ciais, L. Zhou, et al., 2014: Afforestation in China cools local land surface temperature. *Proc. Natl. Acad. Sci. U.S.A.*, **111,** 2915-2919, doi:10.1073/pnas.1315126111.

Piao, S., P. Ciais, Y. Huang, Z. Shen, S. Peng, et al., 2010: The impacts of climate change on water resources and agriculture in China. *Nature*, **467,** 43-51, doi:10.1038/nature09364.

Pielke, R. A., J. Adegoke, A. Beltran-Przekurat, C. A. Hiemstra, J. Lin, et al., 2007: An overview of regional land-use and land-cover impacts on rainfall. *Tellus Ser. B*, **59,** 587-601, doi:10.1111/j.1600-0889.2007.00251.x.

Pongratz, J., L. Bounoua, R. S. DeFries, D. C. Morton, L. O. Anderson, W. Mauser, and C. A. Klink, 2006: The impact of land cover change on surface energy and water balance in Mato Grosso, Brazil. *Earth Interact.*, **10,** 1-17, doi:10.1175/ei176.1.

Qian, W., and A. Qin, 2006: Spatial-temporal characteristics of temperature variation in China. *Meteorol. Atmos. Phys.*, **93,** 1-16, doi:10.1007/s00703-005-0163-6.

Qu, X., G. Huang, and W. Zhou, 2013: Consistent responses of East Asian summer mean rainfall to global warming in CMIP5 simulations. *Theor. Appl. Climatol.*, **117,** 123-131, doi:10.1007/s00704-013-0995-9.

Ramankutty, N., and J. A. Foley, 1999: Estimating historical changes in global land cover: Croplands from 1700 to 1992. *Global Biogeochem. Cycles*, **13,** 997-1027, doi:10.1029/1999gb900046.

Ren, G., Y. Zhou, Z. Chu, J. Zhou, A. Zhang, J. Guo, and X. Liu, 2008: Urbanization effects on observed surface air temperature trends in north China. *J. Clim.*, **21,** 1333-1348, doi:10.1175/2007JCLI1348.1.

Ren, G., Y. Ding, Z. Zhao, J. Zheng, T. Wu, G. Tang, and Y. Xu, 2012: Recent progress in studies of climate change in China. *Adv. Atmos. Sci.*, **29,** 958-977, doi:10.1007/s00376-012-1200-2.

Riahi, K., S. Rao, V. Krey, C. Cho, V. Chirkov, et al., 2011: RCP 8.5 − A scenario of comparatively high greenhouse gas emissions. *Clim. Change*, **109,** 33-57, doi:10.1007/s10584-011-0149-y.

Rudolf, B., and U. Schneider, 2005: Calculation of gridded precipitation data for the global land-surface using in-situ gauge observations. *Proceedings of the 2nd Workshop of the International Precipitation Working Group IPWG. 2004,* Monterey, CA, European Organisation for the Exploitation of Meteorological Satellites, 231-247.

Sampaio, G., C. Nobre, M. H. Costa, P. Satyamurty, B. S. Soares-Filho, and M. Cardoso, 2007: Regional climate change over eastern Amazonia caused by pasture and soybean cropland expansion. *Geophys. Res. Lett.*, **34,** L17709, doi:10.1029/ 2007GL030612.

Schneider, U., A. Becker, P. Finger, A. Meyer-Christoffer, M. Ziese, and B. Rudolf, 2013: GPCC's new land surface precipitation climatology based on quality-controlled in

situ data and its role in quantifying the global water cycle. *Theor. Appl. Climatol.*, **115,** 15-40, doi:10.1007/s00704-013-0860-x.

Seo, K.-H., and J. Ok, 2012: Assessing future changes in the East Asian summer monsoon using CMIP3 models: results from the best model ensemble. *J. Clim.*, **26,** 1807-1817, doi:10.1175/JCLI-D-12-00109.1.

Seto, K. C., B. Güneralp, and L. R. Hutyra, 2012: Global forecasts of urban expansion to 2030 and direct impacts on biodiversity and carbon pools. *Proc. Natl. Acad. Sci. U.S.A.*, **109,** 16083-16088, doi:10.1073/pnas.1211658109.

Shao, H., J. Song, and H. Ma, 2013: Sensitivity of the East Asian summer monsoon circulation and precipitation to an idealized large-scale urban expansion. *J. Meteorol. Soc. Jpn. Ser. II*, **91,** 163-177, doi:10.2151/jmsj.2013-205.

Shastri, H., S. Paul, S. Ghosh, and S. Karmakar, 2015: Impacts of urbanization on Indian summer monsoon rainfall extremes. *J. Geophys. Res. Atmos.*, **120,** 2014JD022061, doi:10.1002/2014JD022061.

Shepherd, J. M., 2005: A review of current investigations of urban-induced rainfall and recommendations for the future. *Earth Interact.*, **9,** 1-27, doi:10.1175/EI156.1.

Shi, W. L., and H. J. Wang, 2003: The regional climate effects of replacing farmland and re-greening the desertification lands with forest or grass in West China. *Adv. Atmos. Sci.*, **20,** 45-54, doi:10.1007/BF03342049.

Shi, Y., Y. Shen, E. Kang, D. Li, Y. Ding, G. Zhang, and R. Hu, 2007: Recent and future climate change in northwest China. *Clim. Change*, **80,** 379-393, doi:10.1007/s10584-006-9121-7.

Shimadera, H., A. Kondo, K. L. Shrestha, K. Kitaoka, and Y. Inoue, 2014: Numerical evaluation of the impact of urbanization on summertime precipitation in Osaka, Japan. *Adv. Meteorol.*, in press.

Song, F., and T. Zhou, 2014: Interannual variability of East Asian summer monsoon simulated by CMIP3 and CMIP5 AGCMs: skill dependence on Indian Ocean–western Pacific anticyclone teleconnection. *J. Clim.*, **27,** 1679-1697, doi:10.1175/JCLI-D-13-00248.1.

Song, F., T. Zhou, and Y. Qian, 2014: Responses of East Asian summer monsoon to natural and anthropogenic forcings in the 17 latest CMIP5 models. *Geophys. Res. Lett.*, **41,** 596-603, doi:10.1002/2013GL058705.

Sperber, K. R., H. Annamalai, I. S. Kang, A. Kitoh, A. Moise, et al., 2013: The Asian summer monsoon: an intercomparison of CMIP5 vs. CMIP3 simulations of the late 20th century. *Clim. Dyn.*, **41,** 2711-2744, doi:10.1007/s00382-012-1607-6.

Su, F., X. Duan, D. Chen, Z. Hao, and L. Cuo, 2012: Evaluation of the global climate models in the CMIP5 over the Tibetan Plateau. *J. Clim.*, **26,** 3187-3208, doi:10.1175/JCLI-D-12-00321.1.

Suh, M.-S., and D.-K. Lee, 2004: Impacts of land use/cover changes on surface climate over east Asia for extreme climate cases using RegCM2. *J. Geophys. Res. Atmos.*, **109,** D02108, doi:10.1029/2003JD003681.

Swann, A. L. S., I. Y. Fung, and J. C. H. Chiang, 2011: Mid-latitude afforestation shifts general circulation and tropical precipitation. *Proc. Natl. Acad. Sci. U.S.A.*, **109,** 712-716, doi:10.1073/pnas.1116706108.

Takata, K., K. Saito, and T. Yasunari, 2009: Changes in the Asian monsoon climate during 1700–1850 induced by preindustrial cultivation. *Proc. Natl. Acad. Sci. U.S.A.*, **106,** 9586-9589, doi:10.1073/pnas.0807346106.

Tang, G., and G. Ren, 2005: Reanalysis of surface air temperature change of the last 100 years over China (in Chinese). *Clim. Environ. Res.*, **10,** 791-798, doi: 10.3878/ j.issn.1006-9585.2005.04.10

Taylor, K. E., 2001: Summarizing multiple aspects of model performance in a single diagram. *J. Geophys. Res. Atmos.*, **106,** 7183-7192, doi:10.1029/2000JD900719.

Taylor, K. E., R. J. Stouffer, and G. A. Meehl, 2011: An overview of CMIP5 and the experiment design. *Bull. Am. Meteorol. Soc.*, **93,** 485-498, doi:10.1175/BAMS-D-11-00094.1.

Tewari, M., F. Chen, W. Wang, J. Dudhia, M. LeMone, et al., 2004: Implementation and verification of the unified NOAH land surface model in the WRF model. *The 20th Conference on Weather Analysis and Forecasting/16th Conference on Numerical Weather Prediction*. 2004, Seattle, WA, American Meteorological Society, 11-15.

Thomson, A., K. Calvin, S. Smith, G. P. Kyle, A. Volke, et al., 2011: RCP4.5: a pathway for stabilization of radiative forcing by 2100. *Clim. Change*, **109,** 77-94, doi:10.1007/s10584-011-0151-4.

Trail, M., A. P. Tsimpidi, P. Liu, K. Tsigaridis, Y. Hu, et al., 2013: Potential impact of land use change on future regional climate in the Southeastern U.S.: Reforestation and crop land conversion. *J. Geophys. Res. Atmos.*, **118,** 2013JD020356, doi:10.1002/2013JD020356.

Tu, K., Z.-W. Yan, X.-B. Zhang, and W.-J. Dong, 2009: Simulation of precipitation in monsoon regions of China by CMIP3 models. *Atmos. Oceanic Sci. Lett*, **2,** 194-200.

United Nations, 2014: World Urbanization Prospects: The 2014 Revision. Highlights (ST/ESA/SER.A/352). United Nations, Department of Economic and Social Affairs, Population Division, New York, NY, 27 pp.

Van Vuuren, D. P., M. Meinshausen, G.-K. Plattner, F. Joos, K. M. Strassmann, et al., 2008: Temperature increase of 21st century mitigation scenarios. *Proc. Natl. Acad. Sci. U.S.A.*, **105,** 15258-15262, doi:10.1073/pnas.0711129105.

Varis, O., and P. Vakkilainen, 2001: China's 8 challenges to water resources management in the first quarter of the 21st Century. *Geomorphology*, **41,** 93-104, doi:10.1016/S0169-555X(01)00107-6.

Vautard, R., J. Cattiaux, P. Yiou, J.-N. Thepaut, and P. Ciais, 2010: Northern Hemisphere atmospheric stilling partly attributed to an increase in surface roughness. *Nature Geosci.*, **3,** 756-761, doi:10.1038/ngeo979.

Vörösmarty, C. J., P. Green, J. Salisbury, and R. B. Lammers, 2000: Global water resources: vulnerability from climate change and population growth. *Science*, **289,** 284-288, doi:10.1126/science.289.5477.284.

Vuuren, D., J. Edmonds, M. Kainuma, K. Riahi, A. Thomson, et al., 2011: The representative concentration pathways: an overview. *Clim. Change*, **109,** 5-31, doi:10.1007/s10584-011-0148-z.

Wang, G., Y. Kim, and D. Wang, 2007: Quantifying the strength of soil moisture–precipitation coupling and its sensitivity to changes in surface water budget. *J. Hydrometeorol.*, **8,** 551-570, doi:10.1175/JHM573.1.

Wang, G., S. Sun, and R. Mei, 2011: Vegetation dynamics contributes to the multi-decadal variability of precipitation in the Amazon region. *Geophys. Res. Lett.*, **38,** L19703, doi:10.1029/2011GL049017.

Wang, H., W. Shi, and X. Chen, 2006a: The statistical significance test of regional climate change caused by land use and land cover variation in West China. *Adv. Atmos. Sci.*, **23,** 355-364, doi:10.1007/s00376-006-0355-0.

Wang, J., J. Feng, Z. Yan, Y. Hu, and G. Jia, 2012: Nested high-resolution modeling of the impact of urbanization on regional climate in three vast urban agglomerations in China. *J. Geophys. Res. Atmos.*, **117,** D21103, doi:10.1029/2012JD018226.

Wang, L., and J. Feng, 2011: Two major modes of the wintertime precipitation over China (in Chinese). *Chin. J. Atmos. Sci.*, **35,** 1105-1116, doi: 10.3878/j.issn.1006-9895.2011.06.10.

Wang, L., and W. Chen, 2013: A CMIP5 multimodel projection of future temperature, precipitation, and climatological drought in China. *Int. J. Climatol.*, **34**, 2059-2078, doi:10.1002/joc.3822.

Wang, S., and D. Gong, 2000: Enhancement of the warming trend in China. *Geophys. Res. Lett.*, **27,** 2581-2584, doi:10.1029/1999GL010825.

Wang, S., D. Gong, and J. Zhu, 2001: Twentieth-century climatic warming in China in the context of the Holocene. *The Holocene*, **11,** 313-321, doi:10.1191/095968301673172698.

Wang, S., J. Zhu, and J. Cai, 2004: Interdecadal variability of temperature and precipitation in China since 1880. *Adv. Atmos. Sci.*, **21,** 307-313, doi:10.1007/BF02915560.

Wang, S., J. Ye, D. Gong, J. Zhu, and T. Yao, 1998: Construction of mean annual temperature series for the last one hundred years in China (in Chinese). *Q. J. Appl. Meteor.*, **9,** 392-401.

Wang, X., F. Chen, and Z. Dong, 2006b: The relative role of climatic and human factors in desertification in semiarid China. *Glob. Environ. Change*, **16,** 48-57, doi:10.1016/j.gloenvcha.2005.06.006.

Wang, X., F. Chen, E. Hasi, and J. Li, 2008: Desertification in China: an assessment. *Earth-Sci. Rev.*, **88,** 188-206, doi:10.1016/j.earscirev.2008.02.001.

Wang, X., X. Sun, J. Tang, and X. Yang, 2015: Urbanization-induced regional warming in Yangtze River Delta: potential role of anthropogenic heat release. *Int. J. Climatol.*, in press, doi:10.1002/joc.4296.

Wang, X., J. Liao, J. Zhang, C. Shen, W. Chen, B. Xia, and T. Wang, 2013: A numeric study of regional climate change induced by urban expansion in the Pearl River Delta, China. *J. Appl. Meteor. Climatol.*, **53,** 346-362, doi:10.1175/JAMC-D-13-054.1.

Wang, Y.-L., J.-M. Feng, and H. Gao, 2014: Numerical simulation of the impact of land cover change on regional climate in China. *Theor. Appl. Climatol.*, **115,** 141-152, doi:10.1007/s00704-013-0879-z.

Wang, Y., and L. Zhou, 2005: Observed trends in extreme precipitation events in China during 1961–2001 and the associated changes in large-scale circulation. *Geophys. Res. Lett.*, **32,** L09707, doi:10.1029/2005GL022574.

Wei, K., T. Xu, Z. Du, H. Gong, and B. Xie, 2013: How well do the current state-of-the-art CMIP5 models characterise the climatology of the East Asian winter monsoon? *Clim. Dyn.*, **43,** 1241-1255, doi:10.1007/s00382-013-1929-z.

Wild, M., 2009: How well do IPCC-AR4/CMIP3 climate models simulate global dimming/brightening and twentieth-century daytime and nighttime warming? *J. Geophys. Res. Atmos.*, **114,** D00D11, doi:10.1029/2008JD011372.

Willmott, C. J., and S. M. Robeson, 1995: Climatologically aided interpolation (CAI) of terrestrial air temperature. *Int. J. Climatol.*, **15,** 221-229, doi:10.1002/joc.3370150207.

Xin, X., R. Yu, T. Zhou, and B. Wang, 2006: Drought in late spring of south China in recent decades. *J. Clim.*, **19,** 3197-3206, doi:10.1175/JCLI3794.1.

Xu, C.-H., and Y. Xu, 2012: The projection of temperature and precipitation over China under RCP scenarios using a CMIP5 multi-model ensemble. *Atmos. Oceanic Sci. Lett.*, **5,** 527-533.

Xu, Y., X. Gao, Y. Shen, C. Xu, Y. Shi, and F. Giorgi, 2009: A daily temperature dataset over China and its application in validating a RCM simulation. *Adv. Atmos. Sci.*, **26,** 763-772, doi:10.1007/s00376-009-9029-z.

Xu, Z., R. Mahmood, Z.-L. Yang, C. Fu, and H. Su, 2015: Investigating diurnal and seasonal climatic response to land use and land cover change over monsoon Asia with the Community Earth System Model (CESM). *J. Geophys. Res. Atmos.***,** 2014JD022479, in press, doi:10.1002/2014JD022479.

Xue, Y., 1996: The impact of desertification in the Mongolian and the Inner Mongolian grassland on the regional climate. *J. Clim.*, **9,** 2173-2189, doi:10.1175/1520-0442(1996)009<2173:TIODIT>2.0.CO;2.

Yang, K., Y. Y. Chen, and J. Qin, 2009a: Some practical notes on the land surface modeling in the Tibetan Plateau. *Hydrol. Earth Syst. Sci.*, **13,** 687-701, doi: 10.5194/hess-13-687-2009.

Yang, X., Y. Hou, and B. Chen, 2011: Observed surface warming induced by urbanization in east China. *J. Geophys. Res. Atmos.*, **116,** D14113, doi:10.1029/2010JD015452.

Yang, X., Y. Zhang, L. Liu, W. Zhang, M. Ding, and Z. Wang, 2009b: Sensitivity of surface air temperature change to land use/cover types in China. *Sci. China Ser. D-Earth Sci.*, **52,** 1207-1215, doi:10.1007/s11430-009-0085-0.

Yao, T., J. Pu, A. Lu, Y. Wang, and W. Yu, 2007: Recent glacial retreat and its impact on hydrological processes on the Tibetan Plateau, China, and surrounding regions. *Arct., Antarc., Alp. Res.*, **39,** 642-650, doi:10.1657/1523-0430(07-510)[YAO] 2.0.CO;2.

Yu, L., S. Zhang, J. Tang, T. Liu, K. Bu, et al., 2014: The effect of deforestation on the regional temperature in northeastern China. *Theor. Appl. Climatol.*, **120,** 761-771, doi:10.1007/s00704-014-1186-z.

Yu, R., and T. Zhou, 2007: Seasonality and three-dimensional structure of interdecadal change in the East Asian monsoon. *J. Clim.*, **20,** 5344-5355, doi:10.1175/2007JCLI1559.1.

Yu, R., B. Wang, and T. Zhou, 2004: Tropospheric cooling and summer monsoon weakening trend over East Asia. *Geophys. Res. Lett.*, **31,** L22212, doi:10.1029/2004GL021270.

Yu, R., X. S. Wang, Z. Yan, H. M. Yan, and Q. N. Jiang, 2013: Regional climate effects of conversion from grassland to forestland in southeastern China. *Adv. Meteorol.***,** 630953, doi:10.1155/2013/630953.

Yu, R., W. Li, X. Zhang, Y. Liu, Y. Yongqiang, L. Hailong, and Z. Tianjun, 2000: Climatic features related to eastern China summer rainfalls in the NCAR CCM3. *Adv. Atmos. Sci.*, **17,** 503-518, doi:10.1007/s00376-000-0014-9.

Yuan, X., X.-Z. Liang, and E. Wood, 2012: WRF ensemble downscaling seasonal forecasts of China winter precipitation during 1982–2008. *Clim. Dyn.*, **39,** 2041-2058, doi:10.1007/s00382-011-1241-8.

Zhang, F., X. Li, W. M. Wang, X. L. Ke, and Q. L. Shi, 2013: Impacts of future grassland changes on surface climate in Mongolia. *Adv. Meteorol.*, 263746, doi:10.1155/2013/263746.

Zhang, J. Y., W. J. Dong, L. Y. Wu, J. F. Wei, P. Y. Chen, and D. K. Lee, 2005: Impact of land use changes on surface warming in China. *Adv. Atmos. Sci.*, **22,** 343-348, doi:10.1007/BF02918748.

Zhang, L., and T. Zhou, 2011: An assessment of monsoon precipitation changes during 1901–2001. *Clim. Dyn.*, **37,** 279-296, doi:10.1007/s00382-011-0993-5.

Zhang, Y., 2000: Deforestation and forest transition: theory and evidence in China. *World Forests from Deforestation to Transition?*, M. Palo, and H. Vanhanen, Eds., Kluwer Academic Publishers, Dordrecht, Netherlands, 41-65, doi:10.1007/978-94-010-0942-3_3.

Zhang, Y., T. Li, and B. Wang, 2004: Decadal change of the spring snow depth over the Tibetan Plateau: the associated circulation and influence on the East Asian summer monsoon*. *J. Clim.*, **17,** 2780-2793, doi:10.1175/1520-0442(2004)017<2780: dcotss>2.0.co;2.

Zhang, Y., J. A. Smith, L. Luo, Z. Wang, and M. L. Baeck, 2014: Urbanization and rainfall variability in the Beijing metropolitan region. *J. Hydrometeorol.*, **15,** 2219-2235, doi:10.1175/JHM-D-13-0180.1.

Zhao, C. H., Q. O. Jiang, Z. X. Sun, H. Y. Zhong, and S. S. Lu, 2013: Projected urbanization impacts on surface climate and energy budgets in the Pearl River Delta of China. *Adv. Meteorol.***,** 542086, doi:10.1155/2013/542086.

Zhao, M., and A. Pitman, 2005: The relative impact of regional scale land cover change and increasing CO2 over China. *Adv. Atmos. Sci.*, **22,** 58-68, doi:10.1007/ BF02930870.

Zhao, Z., S. Wang, Y. Xu, G. Ren, Y. Luo, and X. Gao, 2005: Attribution of the 20th Century Climate Warming in China (in Chinese). *Clim. Environ. Res*, **10,** 808-817, doi: 10.3878/j.issn.1006-9585.2005.04.12.

Zheng, Y. Q., G. Yu, Y. F. Qian, M. Q. Miao, X. M. Zeng, and H. Q. Liu, 2002: Simulations of regional climatic effects of vegetation change in China. *Q. J. Roy. Meteorol. Soc.*, **128,** 2089-2114, doi:10.1256/003590002320603557.

Zhou, L., R. E. Dickinson, Y. Tian, J. Fang, Q. Li, et al., 2004: Evidence for a significant urbanization effect on climate in China. *Proc. Natl. Acad. Sci. U.S.A.*, **101,** 9540-9544, doi:10.1073/pnas.0400357101.

Zhou, T., and Z. Li, 2002: Simulation of the east asian summer monsoon using a variable resolution atmospheric GCM. *Clim. Dyn.*, **19,** 167-180, doi:10.1007/s00382-001-0214-8.

Zhou, T., and R. Yu, 2006: Twentieth-century surface air temperature over China and the globe simulated by coupled climate models. *J. Clim.*, **19,** 5843-5858, doi:10.1175/JCLI3952.1.

Zhou, T., L. Zhang, and H. Li, 2008a: Changes in global land monsoon area and total rainfall accumulation over the last half century. *Geophys. Res. Lett.*, **35,** L16707, doi:10.1029/2008GL034881.

Zhou, T., R. Yu, H. Li, and B. Wang, 2008b: Ocean forcing to changes in global monsoon precipitation over the recent half-century. *J. Clim.*, **21,** 3833-3852, doi:10.1175/2008JCLI2067.1.

Zhou, T., D. Gong, J. Li, and B. Li, 2009: Detecting and understanding the multi-decadal variability of the East Asian Summer Monsoon - recent progress and state of affairs. *Meteorol. Z.*, **18,** 455-467, doi:10.1127/0941-2948/2009/0396.

Zhou, T., F. F. Song, R. P. Lin, X. Chen, and X. Chen, 2013: The 2012 north China floods: explaining an extreme rainfall event in the context of a longer-term drying tendency [in "Explaining Extreme Events of 2011 from a Climate Perspective"]. *Bull. Am. Meteorol. Soc.*, **94,** S49-S51, doi:10.1175/bams-d-13-00085.1.

APPENDIX

Figures S1−S3 are supplementary information for section 4.

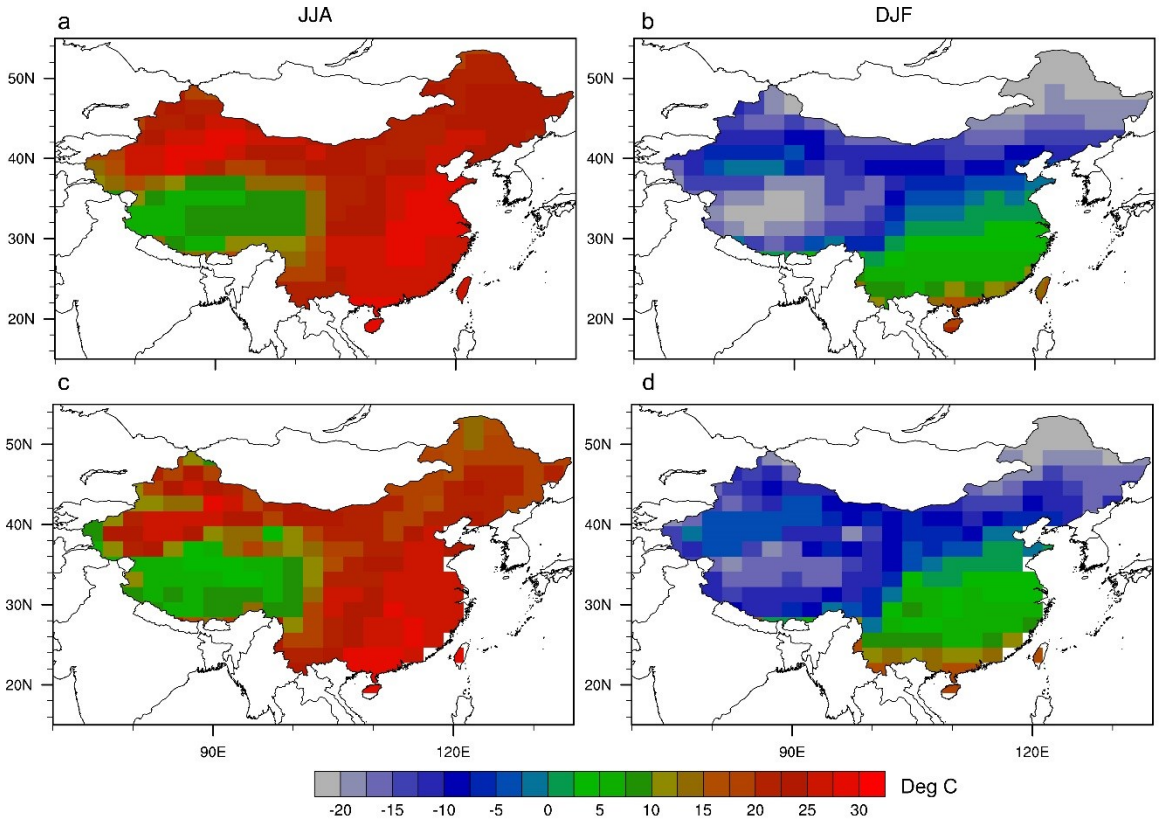

Figure S1. Comparison of summer (a, c) and winter (b, d) mean surface air temperature climatology for 1982–2001 between simulations (a, b) and observations (c, d).

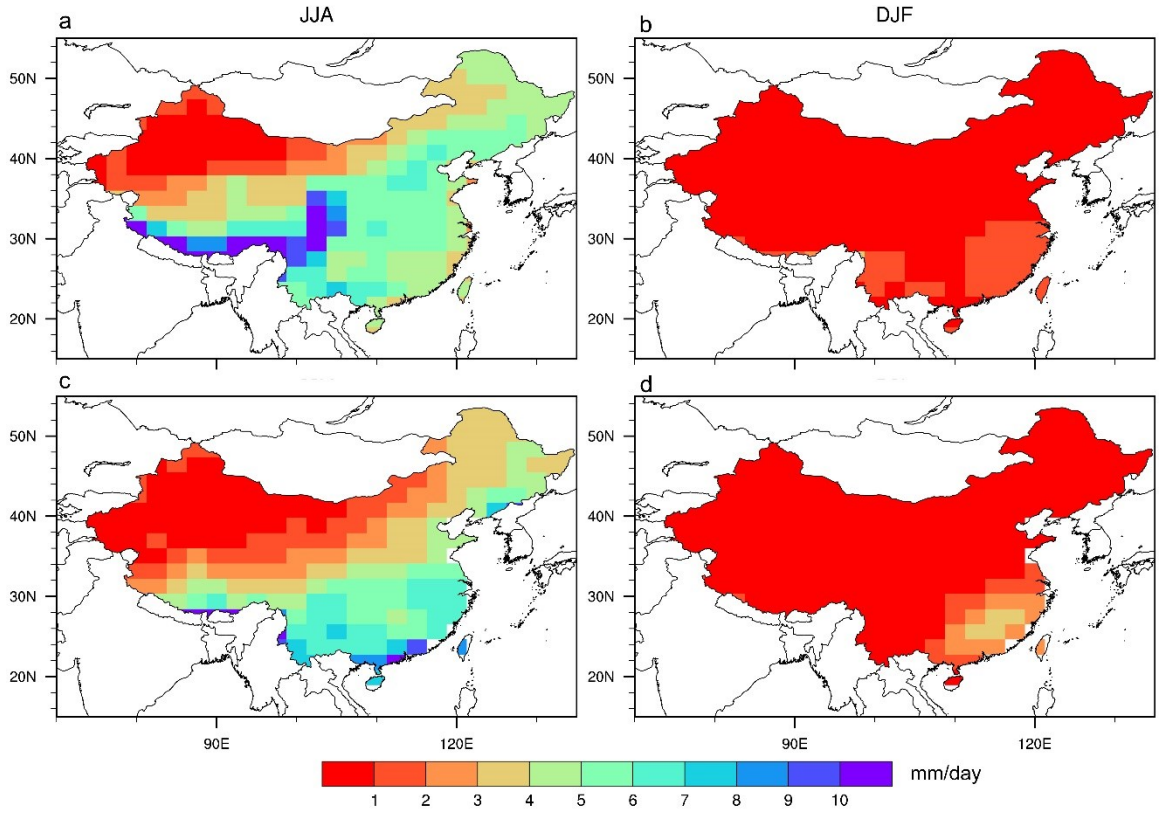

Figure S2. Same as Figure S1 but for precipitation.

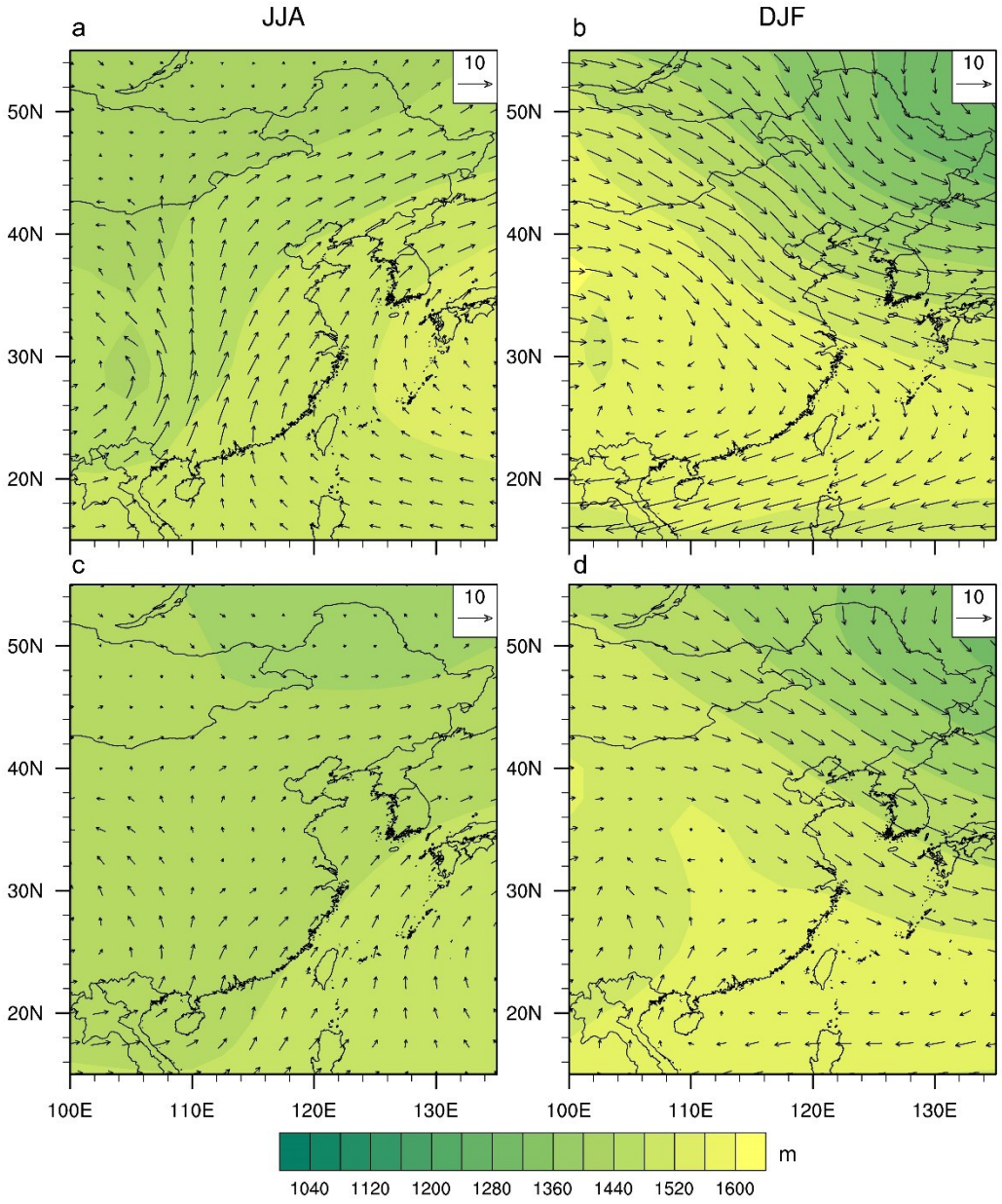

Figure S3. Same as Figure S1 but for geopotential height and wind field at 850 hPa. The shading represents geopotential height (m), and the vectors represent wind speed (m/s).